Sensing with Optical Microresonators and Integrating Cavities

by

William Robert Morrish

A thesis submitted in partial fulfillment of the requirements
for the degree of

Doctor of Philosophy

Department of Physics

University of Alberta

Abstract

This thesis explores theoretical and experimental considerations for the design of refractometric sensors based on optical microcavities for sensing of gases and liquids as well as integrating sphere laser absorption spectroscopy for the detection of greenhouse gases. I discuss highly sensitive refractometric sensing of fluids using a robust, inexpensive platform consisting of a cylindrical microcapillary and broadband light source. Next, I adapt this platform for performing refractometric sensing with the hitherto little-explored "star" and "triangle" modes of microcapillaries. When pumped with sufficient intensity, these modes are capable of lasing and demonstrating high sensitivity to the refractive index of fluids in the capillary channel. This lasing refractometric sensor is then demonstrated for the detection of carboxy-functionalized polystyrene microspheres binding to the inner capillary wall. Finally, I discuss the benefits of using integrating spheres in laser absorption spectroscopy of methane and carbon dioxide, and demonstrate detection of single-digit part-per-million quantities of methane.

Preface

This thesis is an original work by myself, William Morrish.

Chapter 3 was originally published as W. Morrish et al. “Refractometric micro-sensor using a mirrored capillary resonator,” *Optics Express* **24** (22), 24959–24970 (2016). DOI: `10.1364/OE.24.024959`. I performed the experiments, data analysis, and provided substantial revisions to the manuscript. Peter West and Nathan Orlando provided temporary research support; Elizaveta Klantsataya and Dr. Alexandre François developed the silver capillary coating; Kirsty Gardner and Stephen Lane demonstrated experimental techniques used in the data collection; Dr. Raymond DeCorby provided information on Fabry-Perot cavities; and Dr. Al Meldrum provided intellectual contributions, developed experimental techniques, and contributed substantial advice.

Chapter 4 was originally published as W. Morrish et al. “Geometric Resonances for High-Sensitivity Microfluidic Lasing Sensors,” *Physical Review Applied* **10** (5), 051001 (Nov. 2018). DOI: `10.1103/PhysRevApplied.10.051001`. I performed the theoretical analysis, experiments, data analysis, and authored substantial portions of the manuscript. Nicholas Riesen and Dr. Alexandre François developed the procedure for tapering capillaries and fabricated the tapered capillaries used in these experiments. Dr. François also contributed to the theory for detection limits and sensitivity. Simon Stobie provided temporary experimental support. Dr. Al Meldrum contributed substantial advice, experimental direction, and manuscript revision.

Chapter 5 was originally published as Z. Zhang et al. "Functional lasing microcapillaries for surface-specific sensing," *Optics Express* **27** (19), 26967 (2019). DOI: `10.1364/oe.27.026967`. Dr. Zhihong Zhang and myself contributed equally to this document and are co-first authors. Dr. Zhang performed the experiments and helped author the document; Dr. Zhang, S. Yang, and Y. Yang performed the FDTD simulations; I provided experimental direction, mathematical derivations, data analysis, substantial manuscript revisions, and assembled experimental apparatus; Dr. Meldrum provided significant editorial corrections and experimental direction.

Chapter 6 is unpublished as yet. All the experiments and theoretical analysis were performed primarily by myself or with the help of Jamin Achtymichuk and Sofia Arango Arroyave. I wrote the chapter with editorial help from Dr. Meldrum. David Fortin created the drawings for the integrating spheres used in the experiments and helped with the 3D printing; he also demonstrated the electroplating technique. Greg Popowich assisted with the physical vapour deposition of the gold onto the aluminum sphere, which was manufactured by the Physics machine shop. Tanisha Mehreen, Sofia, Jamin, and Dr. Meldrum provided valuable discussion and advice.

This thesis is dedicated with all my love, pride, and respect to my precious parents Bev, Bob, and Donna, and the best brother in the world, Daniel.

“I often say that when you can measure what you are speaking about, and express it in numbers, you know something about it; but when you cannot measure it, when you cannot express it in numbers, your knowledge is of a meagre and unsatisfactory kind; it may be the beginning of knowledge, but you have scarcely, in your thoughts, advanced to the stage of science, whatever the matter may be.”

—William Thomson (Lord Kelvin)

“Had to be me. Someone else might have gotten it wrong.”

—Mordin Solus

“When life give you lemons, squeeze them until you get publishable results.”

—PHDCOMICS

Acknowledgements

I am very grateful to all who have supported me and assisted with my research and this thesis.

The Department of Physics and Faculty of Graduate Studies and Research (FGSR) at the University of Alberta have supported much of this research.

Thanks to Peter West, Nathan Orlando, Jamin Achtymichuk, Dr. Zhihong Zhang, and Sofia Arango Arroyave for their contributions to my research.

The Alberta Technical University of Munich Graduate School for Hybrid Functional Materials (ATUMS) led by Jon and Leah Veinot, Alberta Innovates Technology Futures (AITF), and Natural Sciences and Engineering Research Council (NSERC) of Canada are the primary funding sources for this research.

Thanks to the University of Alberta's NanoFAB, in particular, Stephanie Bozic, and Applied Nanotools' Dr. Jocelyn Bachman for help in designing the waveguides for greenhouse gas sensing. Thanks again to Dr. Bachman for her fabrication of the waveguides used for greenhouse gas sensing.

Thanks to Amira Aissiou, Kirsty Gardner, and Stephen (that's Stephen

with a PhD) Lane for being my companions and associates. Grad school would not have been the same without you, and I appreciate your constant, and important, advice, collaborations, and friendship.

I thank University of Alberta technical specialists Greg Popowich, James Chaulk, and David Fortin for the incredible amount of technical expertise they provided and the knowledge they imparted. I hope you know that I'd still be scraping through my first paper if it wasn't for your knowledge.

I would like to acknowledge the contribution of my supervisory committee, consisting of Drs. Al Meldrum, Frank Hegmann, and Joseph Maciejko, in guiding the course of my program and research and for discussions that have been both beneficial and interesting.

Dr. Alkiviathes Meldrum was absolutely indispensable to this thesis, the papers within, and my maturation as a researcher and human being in general. I thank him for all of his help and guidance over the last 5 years. I had a feeling when I first met him that his optics lab was the ideal place for me; over the next several years I came to realize that it was absolutely the correct place, and staying in his lab to complete my PhD was one of the easiest decisions I've made. For everything he's done things, I'll be forever grateful.

I am incredibly thankful for my family. They have supported me through my entire life and my career as a researcher and I wouldn't have been able to come as far as I have without their love and support.

Contents

List of Tables

List of Figures

Chapter 1

Introduction

Light is universal. It reaches to the edge of known space and illuminates all kinds of mysteries. Due to our innate ability to sense certain frequencies of light, and our innovation in building light sources and detectors that can detect and analyze light with an extraordinary range of frequencies, the measurement of light is now a fundamental part of how we interact with and understand the universe.

While the definition of "optical frequencies" can sometimes be rather fluid, I take it here to include ultraviolet, visible, and infrared frequencies (~1 nm – 1 mm) as in [4, 5]. Optical sensors utilize these frequencies of light to perform measurements. They have a number of powerful features that are advantageous for sensing applications. For example, they require no physical medium so they can operate under vacuum conditions and they can be readily used for remote sensing in harsh or dangerous environments. A great deal of research has gone into producing lasers, LEDs, broadband sources, and other types of light sources in this region of the electromagnetic spectrum.

Optical sensors have a variety of applications. They can be inexpensive and used in relatively mundane applications such as measuring the ripeness of apples [6–8], reading data off of a DVD or Blu-Ray disc [9, 10], determining the amount of light in a room to set the brightness of a phone screen [11, 12], or even just measuring distance [13, 14]. However, they are also present at the very forefront of scientific research. The Laser Interferometric Gravitational Observatory is a billion-dollar kilometre-scale optical sensor capable of detecting minute changes in the very fabric of space due to gravitational waves [15]. However, not all cutting-edge sensors must exist at this scale. Much smaller scale devices are capable of measuring properties of viruses [16], molecules [17], and even individual atoms [18].

With their ubiquitous presence and substantial capabilities, developing new kinds of optical sensors and advancing existing designs is a focus for many research groups. Designing high-performance sensors with smaller physical footprints and lower cost is important in gaining wider industry adoption. Toward these ends, there has been much research into microcavity optical sensors. Microcavities such as rings [19, 20], disks [21], spheres [22–26], toroids [27–29] and capillaries [30–33] confine light to regions measured on the scale of microns. Microcavities can demonstrate the detection of single nanoparticles [34] and molecules [28], and they have been applied to many sorts of problems such as measuring humidity [35], solute concentration [22], temperature [36], refractive index [37], force [38], and magnetic fields [39].

1.1 Optical resonances in capillaries

Microcapillaries are hollow, cylindrical cavities with micron-scale internal and external radii. The work presented in this thesis deals extensively with transparent glass capillaries. The channel through the centre of the capillary provides a convenient internal surface for microfluidics and can be functionalized for biomolecule detection [40]. There are three types of optical resonances in capillaries that will be discussed here: Fabry-Perot (FP) resonances, whispering gallery modes (WGMs), and "geometric modes", which have never previously been studied for sensing purposes and will be one focus of this thesis. Simplified ray representations of these modes are shown in Fig. 1.1.

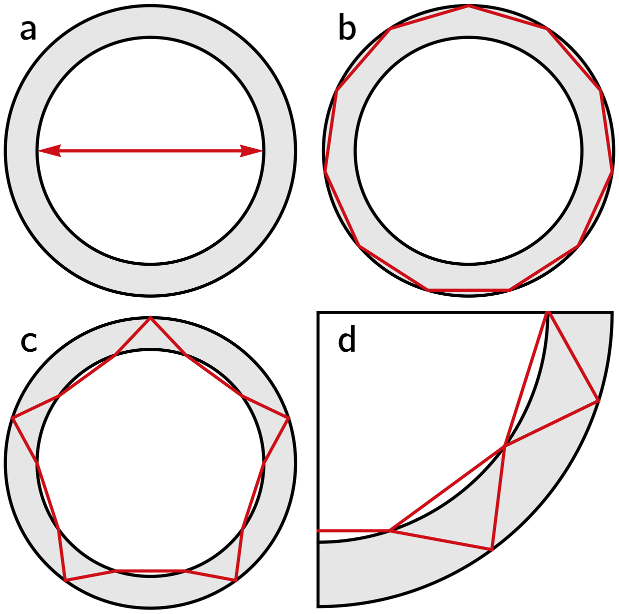

Figure 1.1 Ray diagrams of optical cavities in a capillary. **a** Fabry-Perot modes across the cavity channel. **b** Whispering gallery modes formed around the outer edge of the capillary. **c** "Star" modes formed by rays passing through the capillary wall. **d** "Triangle" modes formed by interference between a ray reflecting off the inner and outer surfaces of the capillary. Both star modes and triangle modes fall under the class of geometric modes, whose theory and sensing performance will be developed in this thesis.

A planar Fabry-Perot (FP) cavity is formed between two flat, parallel surfaces. Interference of light waves reflecting from these surfaces results in optical standing waves forming inside the cavity. If the surfaces are a distance L apart and separated by a dielectric with refractive index n, the resonant wavelengths are given by $\lambda_m = 2Ln/m$, where $m = 1, 2, 3, ...$ is the mode number. The spacing between the resonant wavelengths or frequencies is known as the free-spectral range (FSR). The modes are regularly spaced in frequency, allowing the FSR to be represented as $\Delta f = c/(2Ln)$ [41].

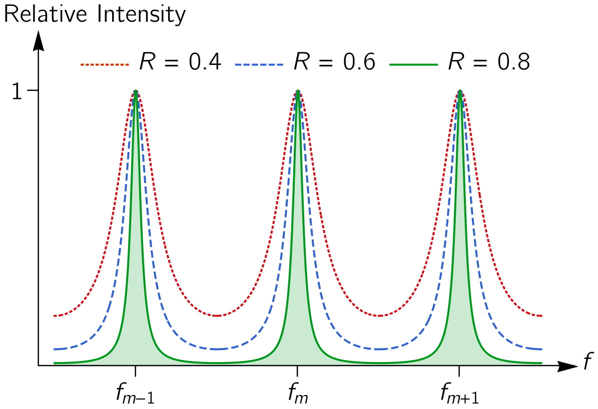

Figure 1.2 Spectrum of FP modes in a cavity with varying mirror reflectivity R. The Q factor increases with reflectivity as shown by the narrowing of the modes. Figure adapted from Ref. [42].

The quality factor Q is the ratio of the electromagnetic energy retained in the cavity to that lost in each round-trip [42]. It can readily be shown [42] that this definition leads to one that is practically measured: the Q factor is simply the centre frequency or wavelength divided by the mode full width at half maximum. By definition, higher Q modes are narrower and thus more monochromatic as illustrated in Fig. 1.2. The quality factor has several equivalent definitions [42]:

$$Q = \frac{f_c}{\Delta f_{\mathrm{FWHM}}} = \omega_c \tau = mF, \tag{1.1}$$

where f_c is the central frequency of the mode, Δf_{FWHM} is the full-width at half-maximum of the resonance, ω_c is $2\pi f_c$, τ is the lifetime of the resonance, and m is the mode number. The finesse F represents the ratio of the FSR to the spectral width and can be defined as [42]

$$F = \frac{\Delta f}{\Delta f_{\mathrm{FWHM}}}. \tag{1.2}$$

The concept of an FP cavity with planar mirrors can be extended to the case of two curved mirrors. Two-mirror systems can be categorized as either stable or unstable resonators. If a ray is traced back and forth between the mirrors and eventually reconnects with itself, it is a stable resonator [43]. In unstable resonators, the ray will eventually reach the edge of a mirror and leave the system. The condition for a stable curved-mirror FP resonator is

$$0 \leq \left(1 + \frac{L}{r_1}\right)\left(1 + \frac{L}{r_2}\right) \leq 1, \tag{1.3}$$

where L is the distance between the centres of the mirrors, and r_1 and r_2 are the radii of curvature for the mirrors. This stability condition can be visualized in Fig. 1.3. The planar case is on the very edge of stability, any slight misalignment in the mirrors will cause the beam to eventually leave the cavity.

A capillary is comprised of a series of concentric surfaces with cylindrical curvature. As light passes through each surfaces, there will be some amount of reflection simply due to differences in refractive index. Both the outermost surfaces and the channel walls form symmetric concentric cavities (Fig. 1.3 **d**), while the pairing of a concave and convex surface form a concentric cavity as in Fig. 1.3 **c**. Both of these cavity types are on the very edge of the stable region. For modes entirely within the capillary channel or within the wall, the resonant wavelengths are the same as in the planar case. FP resonances that incorporate multiple media inside the cavity must take into account the refractive index of each of the layers according

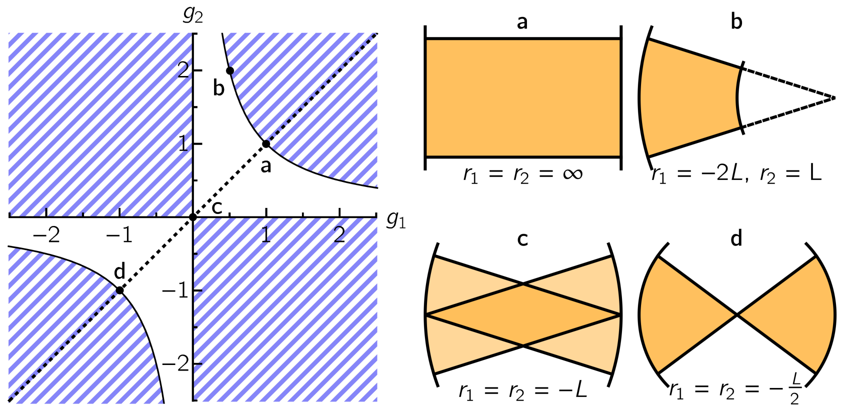

Figure 1.3 Plot of resonator stability from Eq. 1.3 where $g_1 = 1\ Lr_1$ and $g_2 = 1\ Lr_2$. Shaded areas in the plot represent unstable resonators, and symmetric systems lie along the dashed line. Diagrams display mirrors set apart a distance L with the left mirror having a radius of curvature of r_1, and the right mirror a radius of r_2. **a** Planar FP cavity. **b** Concentric concave/convex cavity. **c** Symmetric confocal cavity. **d** Symmetric concentric cavity.

to

$$\lambda_m = \frac{2}{m} \sum_{i=1}^{i=N} L_i n_i \tag{1.4}$$

where N is the total number of layers, L_i is the thickness of layer i, and n_i is the refractive index of layer i, and the summation term represents the optical path length (OPL).

Capillaries can also support whispering gallery modes (WGMs), where light is confined to a circular boundary by total internal reflection (TIR) (Fig. 1.1 **b**). The resonant wavelengths are approximately given by $\lambda_m = 2\pi r n/m$ and the FSR is $\Delta f = \frac{c}{2\pi r n}$ where r is the radius of the circular cavity, n is the refractive index of the channel medium, and m is the mode number [41]. For WGMs to form, it is "critical" that the refractive index of the inner layer be higher than that of the outer layer. Thus, in a bare capillary, WGMs can either form at the outermost glass-air interface, or else at the channel-glass interface if the channel medium has a higher refractive index than the glass.

In this thesis, I will show that another class of resonances, which I refer to as “star and triangle” modes or “geometric modes”, are characteristic of glass capillaries and can also be used for optical sensing (Fig. 1.1 **c** and **d**). For these modes to form, light entering the capillary wall at a shallow enough angle will be refracted and then undergo TIR at the outer glass-air interface, reflecting back towards the centre of the capillary and again refracting as it enters the channel. This process repeats around the edge of the capillary, to eventually form a star-like ray pattern. Triangle modes, which modulate these star modes, result from a splitting of the light rays as they enter the glass wall from the channel, forming a triangular shape in the corresponding ray diagram. These resonances have been only briefly described in the literature [44] and their application towards optical sensing has not been previously explored.

As stated earlier, the advantage of microcavities is that light is trapped inside, repeatedly travelling the same path. This allows for longer effective path lengths and greater interaction between the light and analyte in a compact sensing device. Resonances also provide the opportunity for lasing by providing wavelength selectivity and repeated interaction with a gain medium [30, 45]. Having briefly discussed the various resonances in capillaries, we now turn to a short description of the principles, applications and characteristics of refractometric sensors.

1.2 Refractometric sensing

Refractometric sensing is the process of measuring changes in the refractive index of an analyte. The optical path length (OPL) is the physical distance light travels multiplied by the refractive index of the medium through which it propagates. As such, changes in the refractive index result in a different OPL. Since the resonant wavelengths of an optical cavity depend on the path length, an increase in the OPL will cause the modes to redshift, and a decrease will cause the modes to blueshift. This principle forms the basis for refractive index sensing in optical cavities.

1.2.1 Figures of merit

The sensitivity (S) and limit of detection (LoD) are two of the most important figures of merit for optical sensors. The sensitivity of a refractometric sensor is the rate of change of the mode wavelength with respect to some physical parameter; often this is the refractive index itself, but may also be reported with respect to other properties such as chemical concentration, temperature, pressure, etc. Herein, the sensitivity with respect to refractive index is defined as $S = \frac{\mathrm{d}\lambda_m}{\mathrm{d}n}$ measured as nanometres per "refractive index unit" (nm/RIU) as is typical in the literature.

The limit of detection is the minimum change in a property being measured that produces a detectable change in the mode wavelength. A 99.7% confidence level results in LoD = $3\sigma/S$, where σ is the standard deviation of the data over a period when the property being measured is constant (i.e. the noise level). The sensitivity and LoD are important figures of merit by which the performance of various kinds of sensors can be compared.

1.2.2 Types of sensors

There are a wide variety of refractometric sensors based on resonant optical cavities. Some sensors employ the Fabry-Perot resonances generated between the facets of two end-facing optical fibres to perform sensing. In order to provide a microfluidic cavity, the fibres are sometimes enclosed in a capillary or some other enclosure [46–48].

Photonic crystals are systems of periodically varying refractive index in one or more dimensions. The simplest of these is the distributed Bragg reflector (DBR), where the refractive index varies along a single dimension

[49]. Often, the grating will be incorporated into the structure of an optical fibre (fibre Bragg grating) for use in sensing schemes [50–52]. In two dimensions, there are a wide variety of cavity configurations that can be used for sensing [53–55].

Ring and disk resonators are often microfabricated onto a silicon substrate using UV photolithography [56], electron beam lithography [57], or direct laser writing [58, 59]. Light can then be coupled in evanescently from a fibre, where it circulates before eventually exiting the cavity. Multiple rings or disks coupled together can also be used to create delay lines and add/drop filters [60].

Polymer [61] and glass [62] microspheres, either attached to a fibre [63] or freestanding [37], have also been explored for refractometric sensing. The potential for extremely high Q factors (sometimes in excess of 10^9 [64]) means that they can be extremely sensitive, capable of detecting specific proteins [40] or even a single virus particle [65] that has adhered to the surface. A downside to microspheres is that they are more difficult to incorporate into a microfluidic setup than capillaries or hollow core fibres which naturally provide their own channel for fluids.

Liquid-core optical ring resonator sensors (LCORRS) are a class of capillary sensors where the glass wall of the capillary has been thinned to a thickness of 2–5 µm, typically using hydrofluoric acid [32, 66]. These thinned capillaries are filled with fluid, and pumped by an external light source. Light couples into WGMs at the outer glass-air interface of the capillary, but the electric field extends to the inside channel due to the thinness of the wall. Thus, changes in the refractive index of the channel fluid will affect the wavelengths of the WGMs.

Fluorescent core microcapillaries (FCMs) are a similar type of capillary-based sensor but they do not require thinning. Instead, a fluorescent, high-refractive index layer, such as a polymer or silicon nanoparticle-doped glass layer, is deposited on the inner channel. This device is then pumped by an external light source, and WGMs form at the interface between the layer and inner surface of the capillary [40, 67, 68].

1.2.3 Tracking the resonant modes in optical sensors

Tracking the positions of the modes in refractometric sensors can be accomplished using several methods. “Peak picking” is perhaps the simplest and involves selecting a particular peak or peaks and measuring the position of each of their maxima over time. Alternatively, curve fitting involves fitting a model to each resonant mode. However, this does require one to have an idea of what the model might be beforehand (ideally a simple Lorentzian), as well as determining which data points should be used in fitting the model [69]. A third method is to use Fourier techniques, such as the Fourier shift theorem [70], to track the shift.

The resonant modes in the devices included in this thesis are regularly spaced in frequency and, for large mode numbers m, the modes are nearly periodic in wavelength as well. In the limit of small changes in refractive index, the mode shape remains the same and can be modelled as a pure shift in the phase of the Fourier transform of the mode spectrum [70]. The general procedure is to apply a discrete Fourier transform (DFT) to the data. Then, Fourier components with a power level within a certain range of the peak power are selected to represent the periodic resonances (Fig. 1.4 **b**). As further spectra are acquired, the phase of the selected Fourier components is monitored. These phases can be transformed back into wavelength shifts by applying the formula

$$\delta\lambda = \frac{\Delta\phi}{2\pi}\frac{\Delta\lambda}{k}, \tag{1.5}$$

where k is the Fourier component (with $k = 0$ representing the DC offset), $\delta\lambda$ is the mode shift, $\Delta\lambda$ is the width of the spectrum which was transformed, and $\Delta\phi$ is the phase shift compared to the baseline.

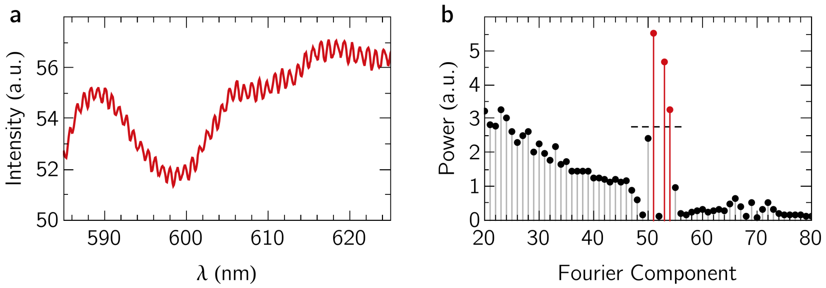

Figure 1.4 **a** Example transmission spectrum of broadband light passing through a capillary perpendicular to the axis. **b** Discrete Fourier transform of the spectrum in **a**. Here, only components near the expected fourier component with power $\geq$ 50% of the peak component would be analyzed (shown in red).

1.3 Laser absorption spectroscopy

While changes in the real component of the refractive index n form the basis of refractometric sensing, changes in the imaginary component k, also known as the extinction coefficient, form the basis for absorptive sensing schemes. In this regime, sensing is primarily based on measuring how much light is absorbed by some molecule of interest. Materials like glass, water, and air have a negligible extinction coefficient at visible wavelengths; mostly, light passes through without attenuation. However, at certain wavelengths, molecules like water vapour, carbon dioxide, methane, and many others have maxima in their absorption due to molecular resonances. In these cases, incoming light will be absorbed.

Laser absorption spectroscopy (LAS) is an absorption-based technique for measuring the presence of certain species of gases. A laser, with a wavelength tuned to one of the absorption features of that gas, is directed through a volume of gas and onto a detector. As either the concentration of the gas or the length of interaction between the gas and laser increases, the intensity at the detector decreases. An advantage of this technique is that many common gas lines are spectrally unique, imparting an intrinsic chemical-specificity.

1.3.1 Rovibrational modes

The absorption features of molecular gases arise from interactions between vibrational and rotational normal modes [71]. Atoms have 3 degrees of freedom (one for each of the x, y, and z directions), so it stands to reason that a collection of N atoms should have $3N$ degrees of freedom. In a molecule, these N atoms are bound together and vibrations result from stretching and compressing these bonds. When all of the atoms translate simultaneously along the same axis, the bonds are not strained. Similarly, atoms rotating about an axis in a coordinated fashion do not strain any bonds. Accounting for these three translations and three rotations (one for each Cartesian axis), a molecule comprised of N atoms has $3N - 6$ possible vibrational modes. Linear molecules only have two rotational degrees of freedom, and therefore have $3N - 5$ possible vibrations.

Of the $3N - 6$ (or $3N - 5$) possible modes, a number of these will be degenerate and have the same energy depending on the symmetry of the molecule [72]. Methane is a 5 atom tetrahedral molecule which should have $3(5) - 6 = 9$ vibrational modes, but only displays 4 (Fig. 1.5). There is a symmetric stretch of all bonds termed ν_1, a doubly degenerate symmetric bending mode ν_2, a triply degenerate asymmetric stretching mode ν_3, and a triply degenerate asymmetric bending mode ν_4 [71]. Carbon dioxide, a linear 3-atom molecule which we might expect to have $3(3) - 5 = 4$ modes (Fig. 1.6), has a symmetric stretching mode ν_1, a doubly degenerate symmetric bending ν_2, and an antisymmetric stretching mode ν_3 [71].

Not all vibrational modes result in an oscillating dipole moment in the molecule. In order to be infrared-active, vibrational modes must have an oscillating dipole moment that is resonant with the frequency of the incoming photons [73]. Symmetric stretching modes cannot absorb light as

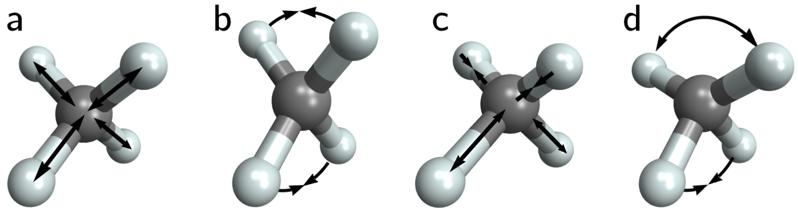

Figure 1.5 Vibrational modes of methane. **a** Symmetric stretching mode ν_1. **b** Doubly degenerate symmetric bending mode ν_2. **c** Triply degenerate asymmetric stretching mode ν_3. **d** Triply degenerate asymmetric bending mode ν_4.

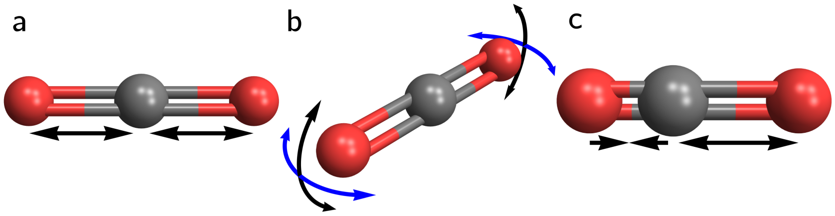

Figure 1.6 Vibrational modes of carbon dioxide. **a** Symmetric stretching mode ν_1. **b** Doubly degenerate symmetric bending mode ν_2; black and blue arrows denote two orthogonal bending directions which are degenerate. **c** Antisymmetric stretching mode ν_3.

there is no change in the dipole moment. As homonuclear diatomic gases only have a symmetric stretching mode, they are not amenable to infrared absorption spectroscopy. This also rules out the ν_1 modes of methane and carbon dioxide as candidates for absorption spectroscopy. Similarly, the symmetric bending mode of methane v_2 does not have an oscillating dipole moment.

Each vibrational mode has a ground state energy and many possible excited states. However, it can be shown that only transitions between the ground state and first excited state contribute to the absorption spectrum at room temperature. The Boltzmann distribution can be used to ascertain the ratio of molecules in two different states as

$$\frac{N_{\text{upper}}}{N_{\text{lower}}} = \exp\left(\frac{-\Delta E}{kT}\right), \tag{1.6}$$

where N_{upper} is the population of the higher state, N_{lower} is the population of the lower state, ΔE is the energy difference between the states, k_B is the Boltzmann constant, and T is the temperature [74]. While the spacing between energy levels is not constant, and differs depending on the molecule, to an order of magnitude it can be approximated as $10^3\,\text{cm}^{-1}$ ($10\,\mu\text{m}$) [71]. Assuming a temperature of 297.15 K, the ratio of the number of molecules in the first excited state of a vibrational mode to that in the ground state is

$$\frac{N_{\nu=1}}{N_{\nu=0}} = \exp\left(\frac{-6.626\times10^{-34}\,\text{J s}\cdot 3\times10^{8}\,\text{m/s}}{10^{-5}\,\text{m}\cdot 1.38\times10^{-23}\,\text{J/K}\cdot 297.15\,\text{K}}\right) \approx 0.008,$$

indicating that less than 1% of the atoms will be in the first excited state at room temperature. As the energy difference between the ground and first excited state grows, this ratio approaches zero. Since so few molecules exist in an excited state at room temperature, vibrational transitions from an excited state to an even higher energy excited state will have negligible contribution to the overall absorption spectrum and can largely be ignored.

A transition from the ground state of a mode to the first excited state ($\nu = 0 \rightarrow \nu = 1$) is the fundamental absorption. Transitions to higher excited states ($\nu = 0 \rightarrow \nu = 2$, $\nu = 0 \rightarrow \nu = 3$, etc.) are called overtones. Absorptions at the fundamental frequency ν_i are the strongest; the first overtone (labelled $2\nu_i$ since it is approximately twice the frequency) is considerably weaker, and the second overtone $3\nu_i$ is typically negligible [71]. Resonance between two different transitions with similar frequencies (e.g. if an overtone of one mode has similar frequency to the fundamental of another mode) will increase the strength of the absorption. Absorption may also occur at combinations and differences of fundamental and overtone frequencies but, unless reinforced by resonance between other modes with the same frequency, their strength is negligible.

Discussion of the fundamental and overtone frequencies seems to imply that a typical molecular absorption spectrum should have, at best, three absorption features for each non-degenerate, IR-active vibrational mode. However, absorption spectra of polyatomic molecules, such as methane or carbon dioxide, display many more absorption peaks. This is due to the interplay between vibration and rotation. Transitions between states of purely rotational modes, where they exist, have energies far below that of vibrational transitions. Due to their lower energy, many rotational states are occupied at room temperature [74]. Combinations and differences of vibrational and the numerous rotational transitions result in a series of closely spaced absorption peaks arranged about a fundamental or overtone absorption.

The allowed transitions between energy levels upon absorption of an infrared photon can be described with selection rules. For vibrational modes, transitions between any two states are allowed ($\Delta\nu = \pm1, \pm2, \pm3, ...$), where $\Delta\nu = 1$ or 2) are most common based on the occupation of higher levels decreasing rapidly as shown earlier. Let J'' represent the occupied rotational energy level in the lower vibrational state ($\nu = 0$), J' the rotational energy level in the upper vibrational state ($\nu = 1$ or 2, usually), then the change in levels on transition is ΔJ. For vibrational modes with a dipole pointing along an axis of symmetry, $\Delta J = \pm1$; a change in vibrational energy levels must be accompanied by a change in rotational energy level to conserve angular momentum from the absorbed photon. For vibrational modes with dipoles perpendicular to an axis of symmetry, $\Delta J = 0, \pm1$. In Raman spectroscopy, where a photon is absorbed and re-emitted, the possibility of $\Delta J = 2$ arises but will not be discussed here. Each possible ΔJ gives rise to a family of lines or branch:

ΔJ:	-2	-1	0	1	2
Branch:	*O*	*P*	*Q*	*R*	*S*

with the R branch on the high frequency side of the central Q branch. The collection of lines in the Q branch, when present, have very small differences in energy and are difficult to separate spectroscopically. Some P, Q, and R transitions are shown in Fig. 1.7.

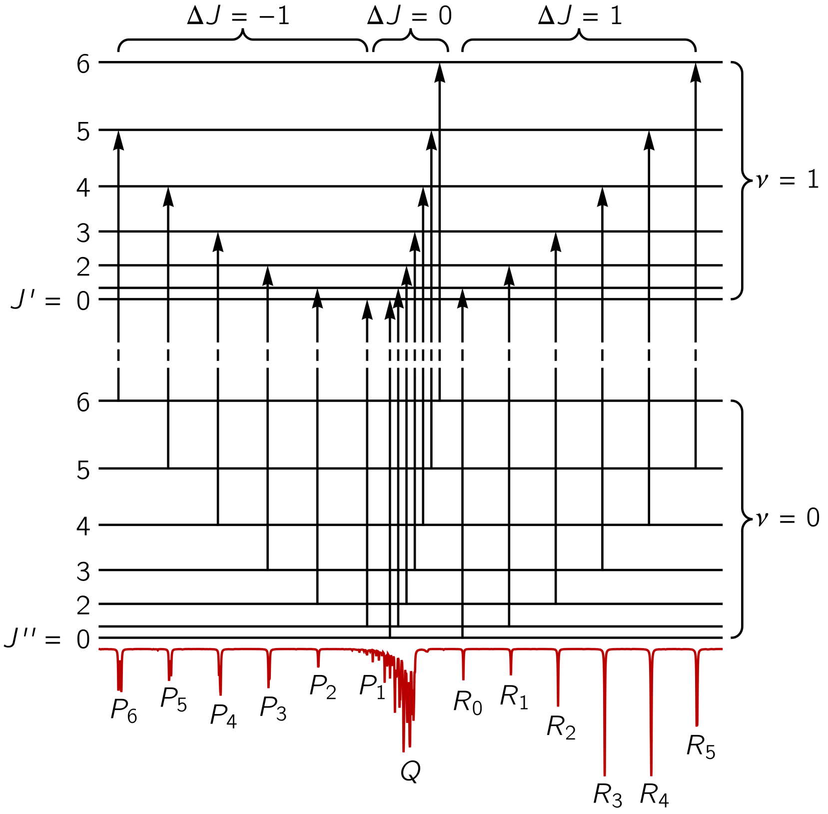

Figure 1.7 Schematic of selected rovibrational transitions demonstrating the P, Q, and R branches with subscripts denoting the J'' level of the transition. The Q branch contains many closely spaced transitions. The graph at the bottom shows an example relative transmission spectrum with increasing frequency to the right. Figure adapted from Ref. [71].

The ν_2 mode of carbon dioxide, at 15 µm, is deep into the mid-infrared (MIR) which is taken here to refer to those wavelengths of approximately 3 µm to 15 µm, though the definitions in the literature are somewhat mercurial. MIR lasers and detectors are expensive and thus currently impractical for developing cheaper sensing technologies. The ν_3 antisymmetric stretching mode (~4250 nm) and, in particular, the $2\nu_3$ mode (Fig. 1.8 **b**) are of more practical interest. As the dipole oscillates parallel to the symmetric axis, the selection rules dictate that $\Delta J = \pm 1$. As $\Delta J = 0$ is disallowed, the Q band is absent from the absorption spectrum.

Again, due to the high cost of MIR lasers and detectors, the ν_3 (~3250 nm) symmetric bending mode and $2\nu_3$ overtone of methane and the nearby absorption features (Fig. 1.8 **a**) are the focus of much research for sensing technologies. Equipment for the ν_3 mode is still more expensive than for the $2\nu_3$ mode, but is still more economical than for the ν_4 mode around 7650 nm. For methane, the selection rules allow $\Delta J = 0, \pm 1$ resulting in a fully developed Q branch in addition to the P and R branches.

1.3.2 Types of sensors

There are a variety of absorption-based optical sensing techniques that exploit the rovibrational transitions of molecules. A combination of path length, gas concentration, and absorption strength dictate the level of interaction between the light source and the gas. As the concentration of the gas is generally out of our hands, it's clear that the focus is on creating the longest path length and choosing the strongest absorption feature. Cavity-based systems increase the path length by having light circulate in a high finesse optical cavity, while non-resonant systems involve either reflections between several mirrors in a multipass cell, or entirely random reflections in a diffusely reflecting integrating sphere.

Integrated cavity output spectroscopy (ICOS) is a type of cavity-enhanced absorption spectroscopy. It involves injecting light into a resonant cavity such as a Fabry-Perot or whispering gallery cavity where the path length is enhanced by the cavity effect. A tunable laser is scanned across a narrow range of wavelengths, and the absorption is measured based

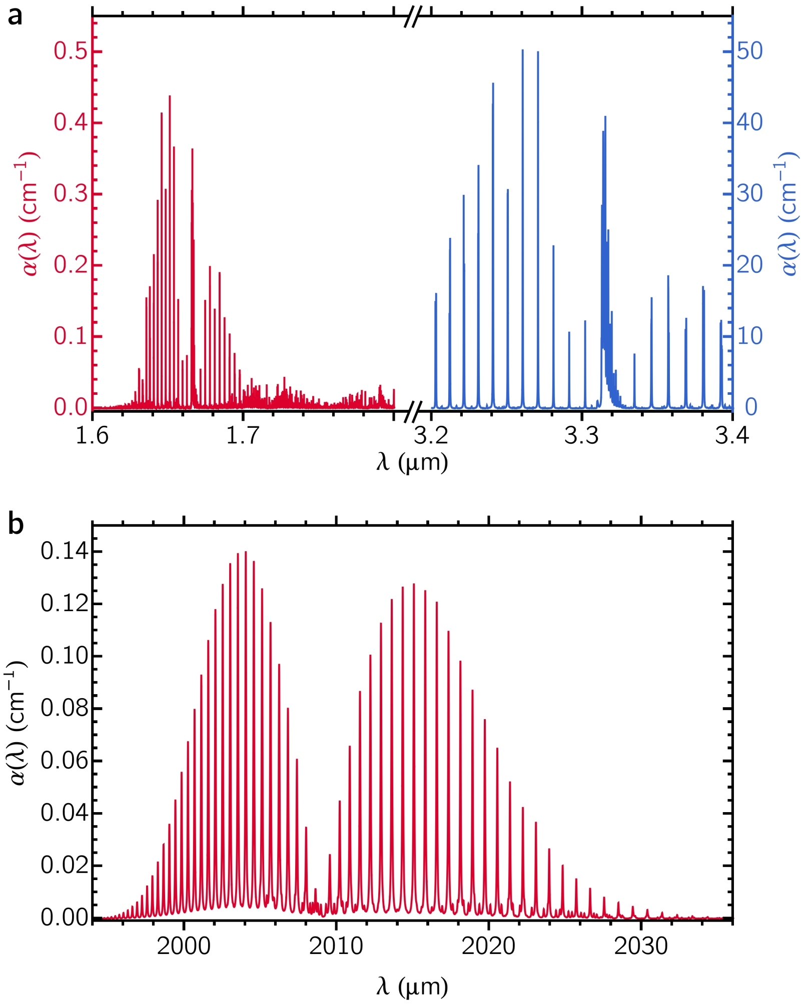

Figure 1.8 Absorption spectra for methane and carbon dioxide calculated from the HITRAN 2016 database [75]. **a** The methane absorption lines around the $2\nu_3$ transition (~1660 nm) and ν_3 (~3320 nm). **b** The carbon dioxide absorption lines around the $2\nu_3$ overtone (~2010 nm).

on the amount of light that reaches a photodetector at the output coupler [76]. ICOS systems can massively increase the effective path length, with one example producing an effective path length of 4.2 km from an 88 cm cell [77]. A compact 5.3-cm-long cell is capable of measuring as little as 2 ppb nitric oxide in human breath [78]. Combining an optical parametric oscillator laser with an ICOS cavity, simultaneous detection of ethane, methane, and water vapour concentrations in human breath is feasible [79].

Cavity ringdown spectroscopy (CRDS) is closely related to ICOS. The main difference is that CRDS is a time domain technique that monitors the temporal decay rate of the light in the cavity [80]. A pulse of light is injected into the cavity and the output light is monitored. The decay rate of the light in the cavity will increase when an absorber is present inside the cavity. CRDS can be incredibly sensitive owing to the long effective path lengths as well as its insensitivity to fluctuations in the intensity of the injected light [81]. Since only the rate of decay matters, differences in pulse intensities have no effect on the result. More recent CRDS systems are even capable of using continuous wave sources rather than pulsed sources by utilizing an acoutso-optic modulator to rapidly interrupt the laser [82, 83]. Detection limits for CRDS can be in the parts-per-trillion level [84].

There are a few non-resonant techniques as well. Photoacoustic spectroscopy (PAS) involves delivering modulated optical radiation into a gas cell. This results in a periodic expansion and contraction of the gas and generates pressure waves in the cell. These acoustic waves are then detected by a transducer of some kind—possibly a micromechanical membrane acting as a microphone. The signal from the microphone is then analyzed and is the basis of detection for PAS systems [85]. Some designs even use a quartz tuning fork for transducing the pressure waves [86]. Using 3 different laser sources and resonators, but only a single microphone, multiple gases can be monitored simultaneously [87]. PAS systems can measure gases like hydrogen fluoride down to sub-ppt levels given sufficiently long averaging times [88].

Open-path gas detectors place the laser source and detector far apart in order to measure across large distances [89]; this is not practical for a compact sensor, but can be useful for monitoring gas concentrations over long distances. Alternatively, one may envision folding the path length in on itself using mirrors. A White multipass cell (1.9 **a**) has three concave mirrors with two of the mirrors placed opposite a larger mirror, again resulting in multiple reflections [90, 91]. The Herriott multipass cell (Fig. 1.9 **b**) employs two concave mirrors with small entrance and exit holes for a laser beam [92–94]. The beam bounces multiple times between the mirrors depending on the entrance angle and distance between the mirrors. Circular multipass cells (Fig. 1.9 **c**) have either a single, circular mirror surface, or multiple mirrors arranged in a circular pattern and separated by an absorbing material [95–97]. The absorbing material helps to ensure one particular path is followed even if the beam is somewhat divergent [98].

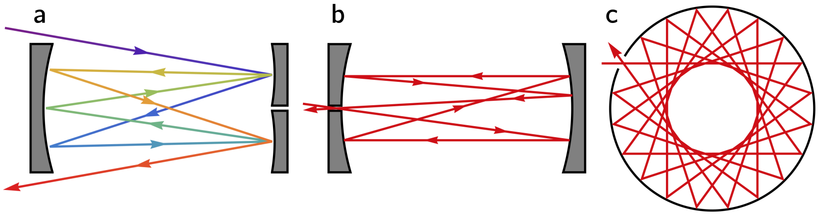

Figure 1.9 Diagrams of multipass cells; angles are exaggerated for clarity. **a** White cell. The gradient colour is meant to help follow the reflections. **b** Herriott cell. **c** Circular multipass cell.

Herriott, White, and circular multipass cells rely on repeated reflections between polished, precisely aligned mirrors. Integrating spheres offer an intriguing alternative: they have random reflections with no requirement for a smooth surface or precise alignment. Integrating spheres have rough, highly reflective inner surfaces designed to reflect light randomly until it reaches a detector or collection port as shown in Fig. 1.10. These reflections extend the path length of light in the sphere, but allow for light to travel many paths through the sphere—some are shorter, some are longer.

While the path length enhancement tends to be less than for multipass cells or cavity-enhanced methods, integrating spheres are still an attractive platform because they are relatively inexpensive and easy to set up [99]. Industrial and atmospheric monitoring of gases like methane and carbon dioxide don't necessarily require the sub-ppt and sub-ppb sensitivity that can be achieved by ICOS, CRDS, and PAS, so more economical designs have practical utility. Integrating spheres have been used to detect hazardous gases such as nitrogen dioxide and sulphur dioxide [99], water vapour and butane [100], carbon monoxide [101], and methane [102].

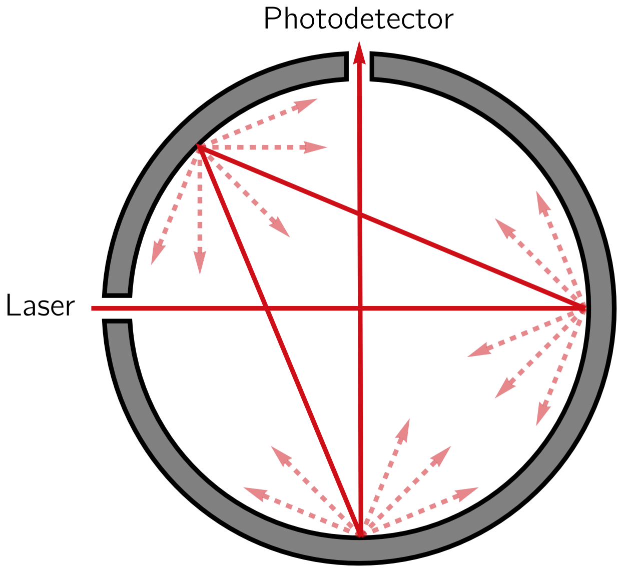

Figure 1.10 Diagram of light passing through an integrating sphere. An initially collimated laser beam will be scattered upon reflection from the surface of the sphere. The light will bounce randomly until it is either absorbed by gas molecules in the chamber or it reaches the photodetector.

1.4 Conclusion

In this introduction, I first explored the types of optical resonances that can exist in capillaries and how they might be applied towards refractometric sensing. I also discussed some important terms as well as a brief overview of what other kinds of resonant refractometric sensors are being researched. The focus of Chapter 3 will be on Fabry-Perot modes in a capillary, while Chapters 4 and 5 will focus on star and triangle modes in capillaries and their application toward refractometric sensing. Then, I described how resonance between rotational and vibrational motion of molecules and electromagnetic radiation leads to absorption features at particular wavelengths. These features have been exploited by various types of optical absorption spectroscopy schemes. Developing integrating sphere laser absorption spectroscopy for the measurement of methane and carbon dioxide will be the focus of Chapter 6 of this thesis.

Chapter 2

Experimental methods

2.1 Preparation of Fabry-Perot capillaries

Bare capillaries were prepared from Polymicro Technologies® fused silica tubing. This tubing has a nominal inner diameter of 50 µm and outer diameter of 360 µm including a 20 µm polyimide jacket. I sectioned the tubing into lengths of ~5 cm by scoring the jacketed tubing and breaking the segments with tweezers. I then placed a silica boat containing a batch of capillaries into a tube furnace. In order to burn off the coating, the temperature was held at 650 °C for 45 minutes in flowing oxygen.

I then coated the channel of the capillaries with poly-pentabromophenylacrylate (PBPA) obtained from Sigma-Aldrich. The PBPA was dissolved in chloroform (1 mg/mL) and drawn into the channel by capillary action. I heated the capillaries on a hot plate at ~70 °C for 20 minutes until the chloroform had evaporated. This left a thin layer of about 200 nm of polymer on the inner surface of the capillary.

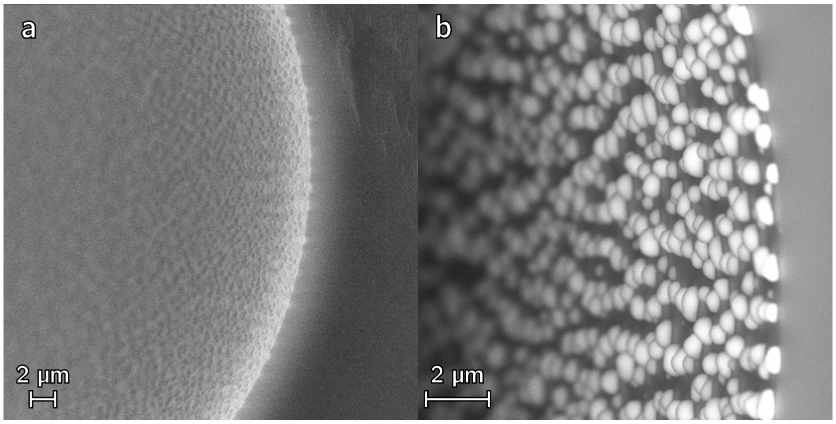

Figure 2.1 SEM images of silver-coated capillaries taken on a Zeiss Sigma 300 VP-FESEM. **a** Variable pressure secondary electron image of the inner surface of a microcapillary at 2,280X magnification. **b** Backscattered electron image of the silver layer at 6,000X magnification.

The silver-coated capillaries were prepared by Elizaveta Klantsataya and Alexandre François from the University of South Australia. The capillaries were first ashed to remove the polyimide jacket. Then, a solution of tin(II) chloride was prepared by mixing 0.1 M $SnCl_2$ and 0.1 M HCl. The resulting solution was flowed through the capillary channel at a rate of 50 μL/min for 5 minutes. This tin(II) chloride causes greater adhesion of the silver film on the capillary walls [103]. Mixing silver nitrate (0.24 M; aqueous) with potassium hydroxide (0.25 M) precipitated silver oxide. Ammonia (3 M) was slowly added to this solution until the silver oxide dissolved, producing Tollens' reagent. A mixture of methanol and 1.9 M glucose in a 1:2 ratio was then mixed with Tollens' reagent and the resulting solution was flowed through the capillary channel for 4 minutes. This produced a layer of silver about 10-30 nm thick on the capillary wall and served to increase the reflectiveness of the wall. This layer is relatively rough as seen in Fig. 2.1.

2.2 Fabrication of Tapered Capillaries

Tapered capillaries were prepared by collaborators Nicholas Riesen and Alexandre François from the University of South Australia. The outer coating of nominally 250 µm inner diameter and 320 µm outer diameter capillaries was again removed by ashing in a tube furnace. Then, the capillaries were heated with a graphite filament and gently pulled in a custom apparatus until the middle tapered to the desired radius. This produced capillaries with inner:outer radii of 52:71, 69:91, 84:114, and 99:134 µm. A set of capillaries without modified radii were measured to have a ratio of 121:161 µm. All capillary sizes were determined by optical microscopy.

2.3 Functionalizing capillaries with PE layers

Polyelectrolyte (PE) layers were added to the channel walls to create a layer with which to bind polystyrene microspheres to the capillary wall. The steps are as follows:

1. A solution of 10 M NaOH was pumped through a capillary with an inner diameter of 250 µm and 320 µm outer diameter for 2 minutes at a rate of 0.1 mL/min. This cleaned the capillary wall and created a slight negative charge which promoted adhesion of the first polyelectrolyte layer.

2. Water was pumped through at the same rate of 0.1 mL/min to remove any excess NaOH.

3. Rhodamine B (1 mM; aqueous) was pumped through the capillary at 5 µL/min while being excited with the 500 nm light from the pulsed dye laser. Spectra were taken every 30 seconds to establish a baseline, and then the rhodamine solution was washed out of the capillary with water.

4. A 2.5 M aqueous NaCl solution containing 2 mg/mL polyallylamine hydrochloride (PAH) was pumped at a rate of 20 µL/min for 5 minutes followed by water. The PAH had a positive charge which resulted in electrostatic attraction between it and the capillary wall.

5. Polystyrene sulfonate (PSS) solution (also 2 mg/mL with 2.5 M NaCl) was pumped for 5 minutes at 20 µL/min followed by water. PSS has a negative charge.

6. Step 4 was repeated.

7. As in Step 3, rhodamine B solution was pumped through the capillary while spectra were collected.

8. Various concentrations (0.05 mg/mL to 2 mg/mL) of polystyrene microspheres (Polysciences; 50 nm diameter) were pumped into the capillary along with 250 mM n-hydroxysuccinimide (NHS), and 250 mM 1-ethyl-3(3-dimethylaminopropyl)-carbodiimide (EDC) for 30 minutes. The capillary was rinsed with water afterward.

9. Step 7 was repeated.

2.4 Collection of spectroscopic data

Spectroscopic data for Chapters 3, 4, and 5 were generally collected in a similar manner, with a diagram of the experimental setup shown in Fig. 2.2 and photographs shown in Fig. 2.3. Once prepared, polytetrafluoroethylene (PTFE) with an inner diameter slightly larger than the outer diameter of the capillary was glued to both ends of the capillary using Norland Optical Adhesive (NOA) 76. The adhesive was cured under a UV lamp for 60 seconds. The capillary with its tubing was then mounted to a custom-made capillary stage with supports for the capillary and the tubing. Scotch tape was used to secure the assembly to the stage at each support. One end

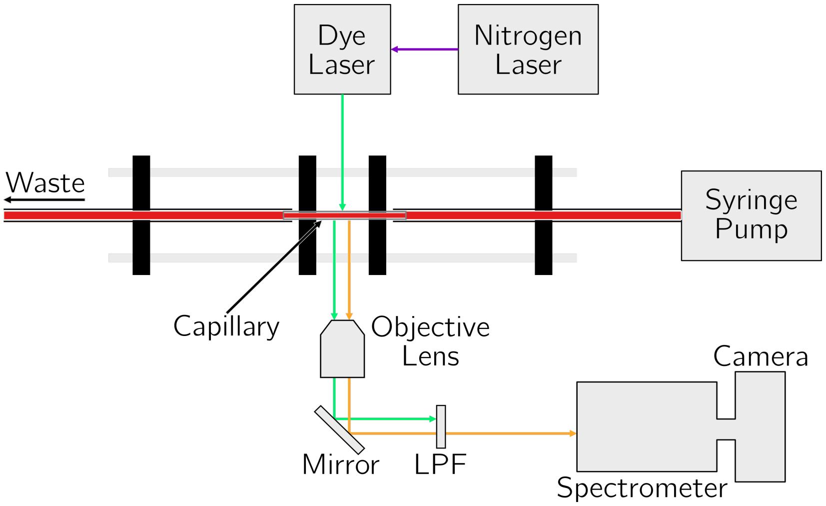

Figure 2.2 Diagram of the experimental setup used for collecting spectra from the capillaries. In the case of Ch. 3, the nitrogen and dye laser were replaced with a broadband lamp and no longpass filter (LPF) was used. The syringe pump forces fluid through tubing and into the capillary which is mounted to a stage. The nitrogen laser emits 337 nm radiation which is converted to 500 nm light by the dye laser attachment. The light source was focused onto the capillary and the resulting emission collected by an objective lens, and passed to a spectrometer.

of the tubing was then attached to a Nanojet syringe pump, and the other open end was routed into a waste collection beaker. The capillary stage was then mounted to a microscope such that the capillary was directly above a 20 × objective lens, and the central channel of the capillary was brought into focus. The objective lens routed the light through the microscope and into a Santa Barbara Instrumentation Group (SBIG) imaging spectrometer with an SBIG ST-7 camera attached.

For the Fabry-Perot resonances in Ch. 3, I used 10% and 11% w/w sucrose in water to perform the sensing measurements. The broadband emission of the transmission light source of the microscope was focussed onto the capillary using a condensing lens. As 11% sucrose solution was pumped through the capillary at a rate of 5 µL/min, 30 second exposures were taken continuously using the spectrometer system. After a sufficient

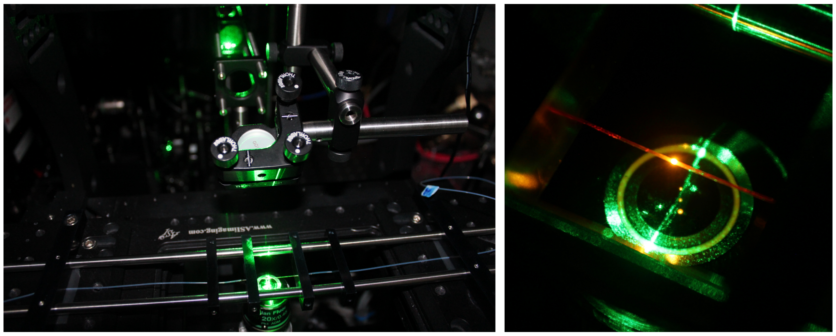

Figure 2.3 Photographs of the capillary experimental setup. **Left** A capillary was attached to tubing and then mounted to a stage. Laser light was focused onto the capillary and the resulting emission was collected by a spectrometer. **Right** A zoomed image of a capillary showing the orange emission of rhodamine B.

number of exposures had been taken to ensure a baseline could be established, the tubing was switched to a syringe filled with 10% sucrose. This new solution was pumped at the same rate while the spectrometer continuously collected spectral images. The analysis of these images is explained in the next section.

The Fabry-Perot capillaries were also used to measure changes in refractive index as a result of change in either gas composition or pressure. Similar to the liquid solution, I alternated flowing high-purity argon and nitrogen gas through the capillary, with argon serving as the baseline while the capillary was illuminated by the broadband source. Here, the tubing was connected to a Y-connection which in turn connected to a regulator on each of the two gas cylinders. The regulators for both gases were set to 170 kPa to try to avoid any change in pressure when the gases were switched. For the measurement of changes in pressure, I flowed the argon gas through the capillary at an initial pressure of 301 kPa. This was held constant as spectra were collected and then quickly, but as smoothly as possible, the pressure was increased to 401 kPa after 25 spectra had been collected, and then again increased to 501 kPa after the collection of a further 25 spectra. The spectrometer was set to automatically collect these spectra, and was left running for the entire ~35 minute duration of the experiment.

In Ch. 4, I used a similar method of connecting a capillary to tubing and the stage Fig. 2.2, and placing the stage on the microscope. This time, however, the pulsed, 337 nm output of a nitrogen laser (Photon Technology International GL-3300) was coupled into a PTI GL-302 dye laser. A high-power laser was necessary in order to stimulate lasing emission from within the capillary. This dye laser had two fused silica cuvettes filled with PL-500 dye solution. The dye laser was set to output 500 nm light, and focussed onto the capillary mounted to the microscope stage (Fig. 2.3). Aqueous solutions of 10% or 11% w/w sucrose and 1 mM rhodamine B were pumped at 5 µL/min through the capillary and were excited by the 500 nm emission of the dye laser with a repetition rate of 3 Hz and approximately 220 µJ pulse energy. This energy was sufficient to promote lasing into the geometric modes of the tapered capillaries. The 10% solution was pumped for 12 minutes to establish a baseline, followed by 11% for 16 minutes, and then 10% again for another 16 minutes. Spectra were collected every 30 seconds throughout the experiment.

2.5 Analysis of capillary mode shifts

Shifts in FP and geometric modes were measured using a Fourier shift method [70]. The first step involved taking a spectrum of a neon calibration lamp shone into the system while keeping all other settings, such as the position of the spectrometer's diffraction grating or the microscope's objective lens, the same as during the experiment. This calibration image was imported into Mathematica, cropped to exclude regions where the light did not land on the sensor, and the image was skewed so that the neon emission lines were vertical in the image. This was done so that the pixels could be vertically binned in order to improve the signal-to-noise ratio of the measured spectra. The emission lines of the calibration lamp were identified either by manually comparing their intensities and spacing to known neon lines, or using a custom-made automated program which performed this routine numerically. This allowed the bright lines from the calibration lamp in the spectral image to be assigned a specific wavelength, and the full wavelength calibration was then obtained by interpolation between the known values.

After calibrating the wavelengths, the spectral images from the experiment were imported and then preprocessed in the same fashion as the calibration image, i.e. they were cropped and skewed in the exact same way, resulting in spectroscopic images with known wavelengths. Each image was then vertically binned to produce an array of wavelength-intensity pairs.

This data was then analyzed using a Fourier shift method. A full description can be found in Ref. [69]. Briefly, a discrete Fourier transform is applied to the data and the phase shift of particular Fourier components between spectral images is calculated. These phase shifts can then be converted back in to wavelength shifts.

Using this technique, I was also able to track multiple mode shifts simultaneously or focus only on modes of interest. In the FP capillaries shown in Ch. 3, pairs of reflections from the four different capillary surfaces created by the inner and outer edge of the glass wall led to multiple signals in the power spectrum due to multiple, overlapping modes. The shifts of the mode of interest could be monitored by only selecting the Fourier components with high power near the expected frequency. In the case of the geometric modes of Chs. 4 and 5, the star modes have a much smaller FSR and redshift with increasing channel refractive index, while the triangle modes have a much larger FSR and blueshift as the refractive index increases. These modes, shifting in opposite senses, were tracked through each spectrum and the resulting shifts were added to improve the sensitivity.

2.6 Lasing threshold measurements

In order to verify that the increase in the peak heights and decrease in width of the modes seen in Ch. 4 was due to the onset of lasing, I performed lasing threshold measurements. An aqueous 1 mM Rhodamine B solution was pumped into the capillary while the capillary was mounted above a microscope objective lens as in Sec. 2.4. A rotating neutral density filter wheel was placed between the output of the dye laser and the capillary. This neutral density filter decreased from optical density (OD) 4 at 0° to OD 0 at 270°. The filter wheel was rotated between OD 4 and OD 0 in 5° increments, and a spectrum was collected at each OD. The spectra were acquired and vertically binned as in Sec. 2.4, although a calibration of the wavelength was not performed since the wavelengths are identical for all of the spectra. The energy per pulse was calculated by multiplying the unattenuated pulse energy of the laser with 10^{OD}. The integrated intensity of each spectrum was plotted against the pump energy and a linear fit was performed to the data on either side of the “kink”. A kink in the graph represents the onset of lasing, and the threshold can be calculated by performing a linear fit to the data points on the high-energy side of the kink and extrapolating back to the x-axis.

Chapter 3

Refractometric micro-sensor using a mirrored capillary resonator

A modified version of this chapter was published as W. Morrish et al. "Refractometric micro-sensor using a mirrored capillary resonator," Optics Express **24** *(22), 24959–24970 (2016).* DOI: `10.1364/OE.24.024959`. *© 2016 Optical Society of America*

3.1 Abstract

We report on a flow-through optical sensor consisting of a microcapillary with mirrored channels. Illuminating the structure from the side results in a complicated spectral interference pattern due to the different cavities formed between the inner and outer capillary walls. Using a Fourier transform technique to isolate the desired channel modes and measure their resonance shift, we obtain a refractometric detection limit of $(6.3 \pm 1.1) \times 10^{-6}$ RIU near a center wavelength of 600 nm. This simple device

demonstrates experimental refractometric sensitivities up to $(5.6\pm0.2)\times10^2$ nm/RIU in the visible spectrum, and it is calculated to reach 1540 nm/RIU with a detection limit of 2.3×10^{-6} RIU at a wavelength of 1.55 µm. These values are comparable to or exceed some of the best Fabry-Perot sensors reported to date. Furthermore, the device can function as a gas or liquid sensor or even as a pressure sensor owing to its high refractometric sensitivity and simple operation.

3.2 Introduction

Microscale optical sensors could address important needs in fields ranging from health sciences to clean energy development [104]. Optofluidic architectures are especially interesting in this context, providing a strong interaction between the probing light and the analyte [104]. Many optofluidic sensors utilize interference effects in which the path length of light within the device is affected by the properties of the analyte medium. Notable types of microscale interference-based sensors include photonic crystal cavities (PCCs) (e.g., Ref [105].) that can act as gas sensors [106], whispering gallery mode (WGM) structures [107], and microscale Fabry-Perot (FP) interferometers [108].

In all these devices, the presence of the analyte causes a change in the local refractive index (RI), which in turn causes a shift in the resonance frequencies. The sensitivity to RI changes in the analyte is typically measured in wavelength shift (nm) per refractive index “unit” (nm/RIU). In WGM-based devices, the sensitivity depends on a variety of experimental parameters and is typically in the range of 5-50 nm/RIU [109, 110]. In PCCs, one can obtain sensitivities as high as 500 nm/RIU [111]. FP interferometers typically have the highest sensitivities because the electric field is predominantly in the analyte region, with values up to 900 nm/RIU [112] or even 1160 nm/RIU [113] as recently reported at a wavelength of

1550 nm.

The limit of detection (LoD) represents the minimum detectable refractive index change. Current typical LoDs are somewhat difficult to summarize coherently since they are almost always extrapolated from much larger RI changes. For fluorescence WGM-based refractive-index sensors, estimated LoDs are typically in the range of 10^{-3} – 10^{-4} RIU [26, 33, 61, 114, 115]. These values can be pushed down to 10^{-5} RIU for PCC gas sensors [105] or ~10^{-6} RIU for evanescently-coupled microspheres and other WGM-type structures [116]. However, these devices can be difficult and/or expensive to prepare and often require expensive precision equipment to be operated, making them impractical for many applications. For example, micron-scale Fabry-Perot cavities on optical fibers are often fabricated using femtosecond machining [108, 113], fusion splicing different fibers [48, 117], or a mix of both [118]. Alternatively, two fiber or waveguide tips with a reflective coating can be positioned in close proximity to form the FP cavity in a flow-through microchannel [119, 120].

Here, we demonstrate a simple capillary-based microfluidic sensor, which doesn't require any micromachining or any other complex microfabrication techniques, with a sensitivity as high as $(5.6\pm0.2)\times10^{2}$ nm/RIU in the visible spectrum, corresponding to ~1540 nm/RIU at a wavelength of 1550 nm, and demonstrate its usage for chemical or pressure sensing. The light scattering and interference pattern from capillaries has been investigated for refractometric applications before [121–126]; here we instead employ the cylindrical FP resonances for sensitive refractometric shift sensing, which is somewhat more reminiscent of the optofluidic photonic crystal cavities reported in [127, 128]. Two different approaches have been pursued to increase the reflectivity of the inner capillary walls, resulting in higher cavity quality (Q) factor. The first approach uses a high refractive index polymer coating, enabling resonances with a sufficiently high visibility and Q to be observed in an all-dielectric structure due to the high refractive index contrast between the channel medium and the deposited polymer layer. The second method used involves the deposition of a silver thin film, using an electroless plating method, onto the inner capillary wall to produce a partially transparent silver mirror. While the latter structure is clearly lossier, the reflectivity of the channel mirrors can be significantly higher than in the polymer case, resulting in clearly distinguishable resonances.

3.3 Basic structure

The devices consisted of channel-coated microcapillaries into which broadband radiation from a tungsten lamp was directed perpendicular to the capillary axis [Fig. 3.1]. It was impractical to measure an insertion loss, but as the incident beam was roughly parallel and not narrowly focused onto the capillary, the percentage of incident radiation coupled into the channel was certainly low; despite this the signal intensity was more than sufficient. In this orientation, the capillary can be viewed as two concentric, low-finesse cylindrical FP cavities with the distance between the mirrors (L) being twice the radius R. There are four interfaces perpendicular to the capillary axis (labeled 1 to 4 on Fig. 3.1) which form sets of different FP cavities. The strongest resonances will correspond to those having the highest reflection coefficients and longest cavity lengths. Of particular importance is the cavity formed between interfaces 2-3 [Fig. 3.1]; because most of the field is contained within the channel it should have the highest sensitivity to the channel media. Cavity (2-3) also forms a marginally stable resonator similar to cavity (1-4) (both have a radius of curvature R equal to half the channel length L). Additional resonances would also exist within the thin mirror layer, but this long-wavelength periodicity is not observable within the ~60-nm wavelength range of our spectrometer.

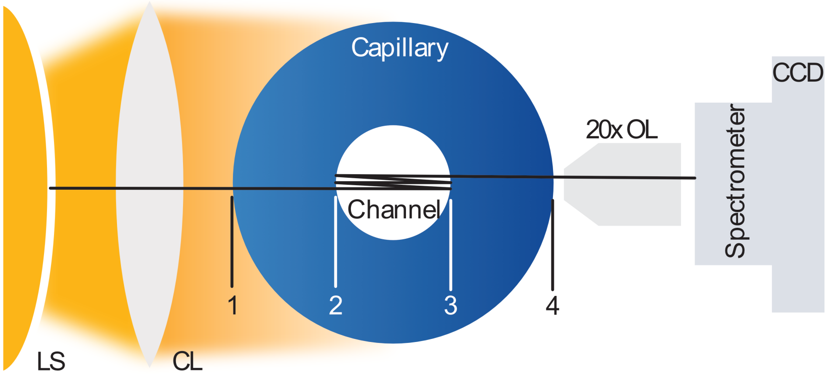

Figure 3.1 Diagram illustrating the basic structure of the capillary and the experimental setup. Light from the tungsten lamp (LS) was roughly collimated using a condenser lens (CL). A 20× objective lens (OL) was used to collect the transmitted radiation and pass it to an imaging CCD spectrometer with a nominal resolving power of 2800. Continuous exposures of 30 seconds each were taken for sensorgram measurements. Capillary interfaces 1, 2, 3, and 4 are labeled. The channel layer thickness is greatly exaggerated for clarity.

In a cylindrical cavity of length $L = 2R$, where R is the radius, the transverse modes are degenerate and the mode spacing is simply given by $\Delta f = c/(2n_{\mathrm{eff}}L)$, where c is the speed of light in vacuum, L is the cavity length (the diameter in this case), and n_{eff} is the effective index, which is analogous to an FP cavity of the same length [129]. The quality factor is approximately $Q = (2\pi L/(-\lambda \cdot \ln[R]))$ ignoring diffraction losses, where R is the reflectance. For the high-index polymer-coated capillary, the calculated Q factor is ~200 for the modes defined by interfaces 2-3 (which we will refer to as “channel modes”) with air in the channel. In contrast, the air-glass outer interface (cavity 1-4) has a predicted Q of ~1400. This difference is mainly due to the much larger length of the (1-4) cavity.

With a silver-mirrored channel, the reflection coefficients and Q factors depend on the mirror thickness. For example, for a 30-nm coating the reflection coefficient is 0.88 and the calculated Q factor is ~4000. Obviously the Q factor would improve with coating thickness, but thick mirrors reduce the transmission through the device.

3.4 Device fabrication and characterization

The microfluidic FP cavities were prepared using fused silica microcapillaries (RI = 1.45) from Polymicro Technologies or Beckman-Coulter, with inner and outer diameters of 50 and 320 µm, respectively. The 20-µm jackets were removed by ashing at 650 °C.

Poly(penta-bromophenyl)acrylate (ppba; Sigma) was chosen as the polymer to be deposited onto the capillary inner wall due to its high refractive index (n 1.7) in the visible [130]. The polymer was dissolved into chloroform (1 mg/mL), the resulting solution was allowed to fill the channel by capillary action, and the solvent was then evaporated at ~70 °C for 20 minutes in atmosphere. The resulting 200-nm-thick polymer layer can be seen in Fig. 3.2 **a** and 3.2 **b**, although its uniformity along the length of the channel was difficult to ascertain by SEM.

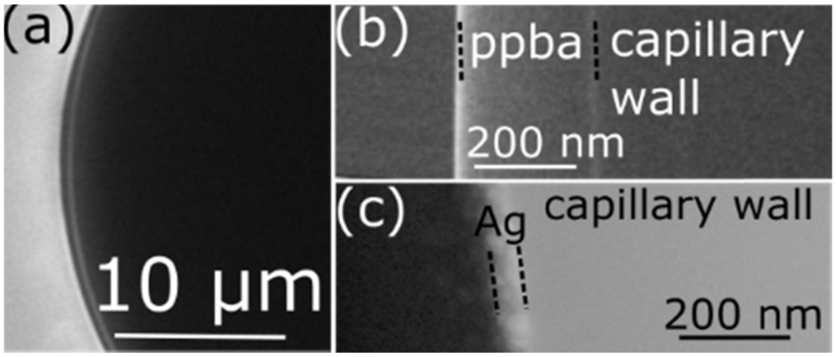

Figure 3.2 **a** Low-magnification SEM image showing the polymer-coated capillary channel. **b** A zoom-in of the interface showing the ~230-nm-thick ppba high-index coating. **a** Same as in **b** except with the Ag mirrors. The Ag coating appears bright against the capillary wall and is ~30 nm thick. These images were taken by cleaving the capillary and imaging it using a Zeiss Sigma 300 VP-FESEM operated at 25 keV in either backscatter or secondary electron mode.

An electroless plating method was used to deposit a silver film inside the capillary channel via the precipitation of metallic silver from ammoniacal silver nitrate solution in the presence of a reducing agent (i.e. Tollens' reaction). First, tin(II) chloride (0.1 M of $SnCl_2$ in 0.1 M of HCl) solution was flowed into the capillary to promote film adhesion onto the fused silica capillary walls [103] using a syringe pump at a constant flow rate of 50 µL/min for 5 min. The preparation of Tollens' reagent started with the oxidation of an aqueous silver nitrate solution (0.24 M) into silver oxide using potassium hydroxide (0.25 M), resulting in the formation of a brown precipitate. Ammonia (3 M) was then added dropwise to the solution to dissolve the silver oxide and produce a transparent silver ammonia complex.

Once the silver ammonia complex became colorless, the reducing agent (1:2 mixture of methanol and 1.9 M glucose) was added to Tollens' reagent to cause the reduction of the silver ammonia complex. This solution was then pumped through the capillary for 4 minutes in order to achieve a silver channel coating a few tens of nm thick. Tollens' reaction also successfully produced a capillary channel coating, with the Ag about 30 nm thick, as seen in Fig. 3.3 **c**, and fairly rough, consistent with previous results on cover slips and optical fibers [131].

The capillaries were then attached to polytetrafluoroethylene tubing and mounted over an objective lens. Light from a tungsten lamp was focused onto one side of the capillary, transmitted through the structure, and the spectrum was projected onto a miniature spectrometer [Fig. 3.1] with a pitch of 0.077 nm/pixel on the CCD. The capillary was precisely aligned parallel to the spectrometer entrance slit, which was centered along the capillary axis. A gas tubing interface was used to force gases through the capillary at controllable pressures while the optical transmission spectra were being collected. Liquid experiments used a syringe pump to inject sucrose-water mixtures into the capillary at a flow rate of 5 µL/min.

Finite-difference time domain (FDTD) simulations using the commercial OmniSim package were performed to validate the experimental data. The domain size was 50 nm, with perfectly matched layers at the boundaries of the simulation domain. The emitter produces a simulated sinusoidal plane wave (in order to match the experiment reasonably well) with a pulse length of 5 fs in order to give a wide spectral range. The simulated time was at least 200 ps, by which time the electric field amplitude in the device had decreased to negligible values. For full devices, a single simulation run took ~4 hours on a 2.4 GHz PC using 15 cores.

3.5 Experimental results

3.5.1 Polymer-coated channels

The transmission spectrum for a capillary with a polymer channel coating (with air both in the channel and outside the capillary) showed a complex set of overlapping cavity resonances [Fig. 3.3], as expected for the four dielectric interfaces. The Fourier spectrum contained at least four high-power regions whose mean free spectral range (FSR) can be determined according to $\Delta\lambda_{\text{spec}}/K$, where $\Delta\lambda_{\text{spec}}$ is the spectral width in Fig. 3.3 and K is the peak Fourier component number. Accordingly, one can extract four main periodicities having mean FSRs of 3.6, 0.92, 0.72, and 0.40 nm. The FSRs calculated according to $\Delta f = c/(2n_{\text{eff}}L)$ for cavities 2-3, 1-2, 1-3, and 1-4 can be estimated using the mean refractive index (i.e., spatially averaged along the path length) for n_{eff}. This gives FSRs of 3.6, 0.91, 0.73, and 0.41 nm, respectively, in reasonably good agreement with observation. The resonances have a somewhat broad Fourier power spectrum because the mode spacing is not perfectly uniform in wavelength units.

To confirm these mode identifications, mineral oil ($n = 1.45$, Sigma) was used as an index matching fluid. When the mineral oil was pumped into the channel (with air on the outside), the only observable modes had

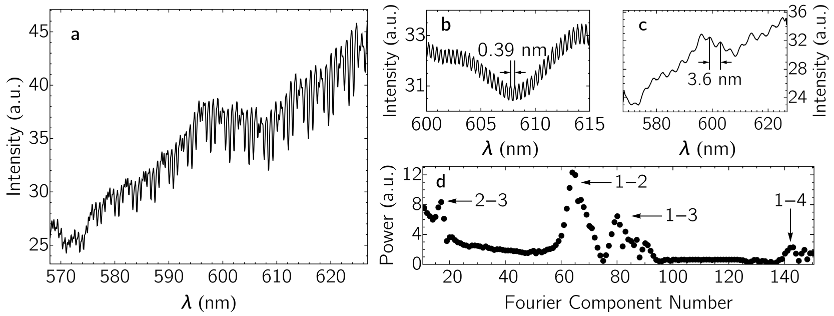

Figure 3.3 **a** Raw transmitted light spectrum showing several overlapping oscillations. **b** Transmission spectrum taken with mineral oil in the channel. Only the high-frequency oscillations corresponding to the cavity defined by interfaces (1-4) are visible. **c** The mode spectrum for the same capillary (with air in the channel) immersed in mineral oil in order to remove interfaces 1 and 4. The low-frequency oscillations with a spacing of 3.6 nm correspond to interfaces (2-3). **d** A Fourier power series for the raw transmitted light spectrum. The arrowed peaks correspond to the cavity defined by the associated interfaces.

a periodicity of 0.39 nm, consistent with a cavity formed by the outer interfaces (1-4) only [Fig. 3.3 **b**]. The observed Q factor for these modes ($Q = \lambda_0/\Delta\lambda_{\mathrm{FWHM}} = {\sim}3000$) appears higher than the theoretical value calculated as described above $Q = (2\pi L/(-\lambda \cdot \ln[R])) = 1400$, but due to extensive mode overlap the measurement clearly underestimates the measured peak width ($\Delta\lambda_{\mathrm{FWHM}}$). To further support the mode identifications, the capillary was next immersed in mineral oil, thus effectively removing interfaces 1 and 4, while the channel contained air. Two holes were drilled into opposite faces of a cuvette. The capillary was inserted through these holes, which were then sealed with adhesive, so that a section of the capillary was inside the cuvette. The cuvette was then filled with mineral oil and capped. In this case, the only observable modes had a periodicity of 3.6 nm [Fig. 3.3 **c**)], confirming that they are indeed the channel modes. The observed Q factor was 225, which is similar to the predicted value of 200 for the polymer-coated channel.

The channel modes are especially applicable for refractometric sensing applications. To demonstrate this, Ar and N_2 gas (99.998% purity) were flowed sequentially through the capillary channel at a pressure of 170 kPa. A channel mode spectrum was collected every 23-46 seconds and the resonance shifts associated with the channel modes were measured using the Fourier shift technique [70] [Fig. 3.4], taking the main Fourier component only to avoid possible overlaps with other modes.

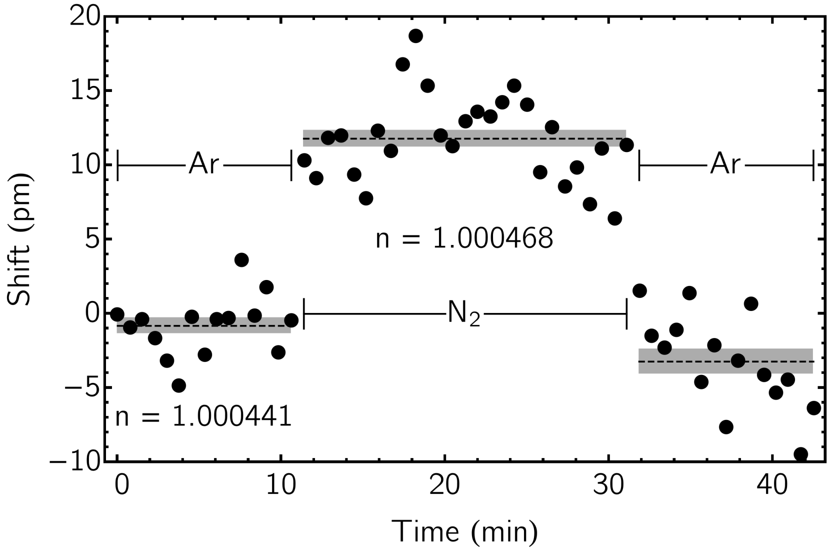

Figure 3.4 Refractometric sensorgram on transitioning from Ar to N_2 and back to Ar. Only the main Fourier component for interface 2-3 was used to calculate the spectral shifts. The grey boundaries are centered on the mean and their thickness represents the standard error of the mean. The refractive indices of Ar and N_2 are also shown, as calculated from the Gladstone-Dale equation. The fact that the final Ar result did not precisely return to the original one within the standard error of the mean is likely due to a systematic (drift) error, possibly caused by mechanical drifts that were difficult to eliminate when changing gases.

The refractive index of Ar at a pressure of 170 kPa (10 psi gauge pressure) can be estimated from the Gladstone-Dale approximation of the Lorentz-Lorenz law given by $n = 1 + \mu(P/T)$ where μ is a gas-dependent constant equal to 762×10^{-9} and 808.8×10^{-9} K/Pa for Ar and N_2, respectively [132], and P and T are the pressure and temperature. Accordingly, the refractive index increases by ~2.7×10^{-5} RIU on transitioning from Ar to N_2 at this pressure. This transition was readily detectable in the sensorgram [Fig. 3.4], which demonstrated a mode shift of 12.6 ± 0.3 pm on going from Ar to N_2. The uncertainties were obtained from the standard error of the mean for each step, with uncertainties for each step added in quadrature. This yields a refractometric sensitivity, S, of $(4.7 \pm 0.3) \times 10^2$ nm/RIU at a wavelength near 600 nm. The relatively large error in the sensitivity is due to the data scatter in Fig. 3.4.

The LoD is typically estimated with 99.7% certainty according to $3\sigma/S$, where σ represents the standard deviation of the wavelength shifts under constant conditions. From Fig. 3.4, the LoD is therefore $(1.3 \pm 0.1) \times 10^{-5}$ RIU. This experimentally-detected change compares favorably with the calculated LoD for recently-developed square capillary devices [133]. However, in typical runs in which it was not necessary to switch gases (and thereby induce pressure fluctuations and mechanical motion), a better 3σ shift resolution was obtained, down to 3.5 pm (an example is shown in Fig. 3.5); accordingly under conditions like those in Fig. 3.5 the device has an LoD of ~$(7.6 \pm 0.5) \times 10^{-6}$ RIU at a wavelength of ~600 nm. Despite its simplicity, the optimum detection limit is comparable to those of the best microscale refractometric devices such as whispering gallery mode [70, 116] and surface plasmon sensors [134].

Finally, a polymer-coated capillary can also serve as a sensitive gas pressure sensor. To demonstrate this, a capillary was filled with Ar at a pressure of 301 kPa and the resonance wavelengths were monitored as the pressure was increased to 401 and then 501 kPa [Fig. 3.5]. The modes redshifted by ~140 pm owing to the pressure dependence of the refractive index of argon as articulated by the Gladstone-Dale equation given above. The results yielded a shift of 4.88 ± 0.01 pm/psi = 0.709 ± 0.002 pm/kPa at a wavelength of ~600 nm, which is close to an order of magnitude better than currently-reported state-of-the-art FP-type gas pressure sensors [135] and is similar to the exceptional response of a just-published fiber sensor [136] that lacks the simple flow capacity shown here. The latter studies used air, which displays similar pressure-related behavior to both Ar and N_2, validating these comparisons. From the mode shift deviations under constant conditions, we find a pressure-related LoD of 4.96 ± 0.01 kPa.

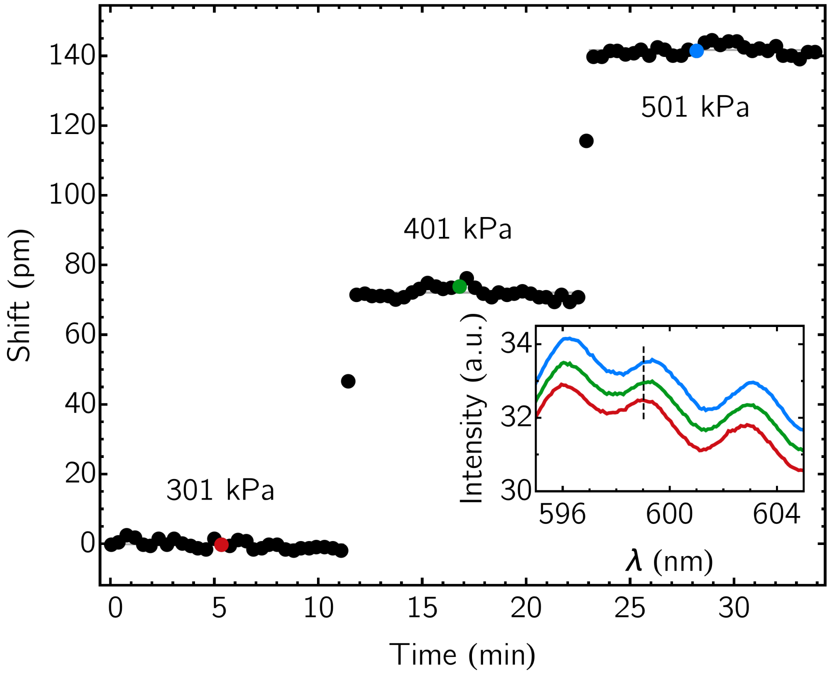

Figure 3.5 Pressure sensorgram showing the mode shifts as the pressure was changed twice and then held for ~11 min. Only the main Fourier component ((2-3) in Fig. 3.3) was used to calculate the spectral shifts. The inset shows a portion of each transmission spectrum on increasing pressure from bottom (red) to top (blue). The colors refer to the specific spectrum indicated by the colored points on the main panel. The standard error of the mean is < 2 pm and is smaller than the data points. The refractive indices estimated from the Gladstone-Dale approximation are 1.00077, 1.00103, and 1.00128 for the three increasing pressures shown.

Liquid sensing is also particularly interesting for a large range of applications. However, the mode visibility of the polymer coated capillary dropped significantly once filled with liquid, to the point where clear sensorgrams couldn't be obtained. The poor mode visibility was attributed to the relatively low refractive index contrast between the polymer coating and water in the capillary channel. It is negligibly influenced by the capillary wall thickness, as one effectively satisfies the "thick substrate" criterion for capillaries of these dimensions.

3.5.2 Silver-mirrored channels

The channel mode visibility with air in the channel was much higher for the silver mirrors [Fig. 3.6] than for the polymer coating, due to the higher reflectivity. The FSR was close to 3.6 nm near $\lambda = 600$ nm, again consistent with the 2-3 resonances. Transfer matrix calculations showed that the reflectivity of a flat, 30-nm-thick silver mirror is 87.6% and 84.8% in air and water, respectively, yielding calculated Q factors on the order of 4000. Experimentally, the Q factors were ~413; these significantly lower values are probably due to scattering induced by the high surface roughness of the deposited silver coating as shown previously [131].

In order to test the response of the Ag-mirrored capillaries, a new pressure sensorgram was taken using Ar in the channel [Fig. 3.7 **a**]. Here the pressure was varied from 301 to 501 kPa in 40 kPa steps. The silver-mirrored capillary tracked these pressure changes well; by using the Gladstone-Dale approximation described above we obtain a pressure sensitivity of 1.08 ± 0.04 pm/kPa corresponding to an RI sensitivity of $(4.2 \pm 0.2) \times 10^2$ nm/RIU. The uncertainty comes from the linear fit to the data in the inset to Fig. 3.7 **a**, where we ignore the error in the pressure measurements as probably smaller than the relative error in $\Delta\lambda$. The LoD calculated from the measured sensitivity and the optimum system resolution (most stable run, where $3\sigma = 3.5$ pm as described above), was 3.3 ± 0.1 kPa.

Unlike the polymer-coated capillary, the silver-mirrored one can also

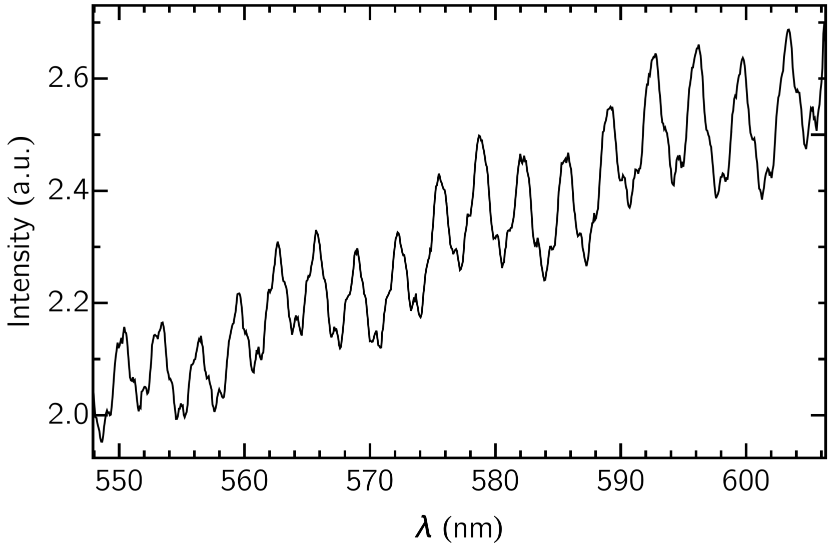

Figure 3.6 Transmission spectrum through the center of a silver-mirrored microcapillary, with Ar in the channel. The spectrum is dominated by a set of modes with an FSR of ~3.6 nm.

readily function as a liquid sensor [Fig. 3.7 **b**]. Whereas for the polymer coating the 2-3 mode visibility became too small, the Ag mirrors retained a high reflectivity and therefore good mode visibility for liquid channel media also. Here, the refractometric sensitivity was found to be 354.2 ± 0.6 nm/RIU for sucrose-water solutions, yielding a best-case 3σ detection limit of $(1.000 \pm 0.002) \times 10^{-5}$ RIU.

3.6 Comments and discussion

The resonance wavelength of an FP cavity is given by $\lambda_0 = 4\pi n L \cos\theta / (2\pi m + \phi_1 + \phi_2)$, where L is the cavity length, θ is the incidence angle, m is the order, and ϕ_1 and ϕ_2 are the phase shifts on reflection at the two interfaces. Accordingly, the refractometric sensitivity of an ideal capillary FP cavity with $m \gg 1$ is given by $S = \mathrm{d}n/\mathrm{d}\lambda \approx 4R/m$, where R is the cap-

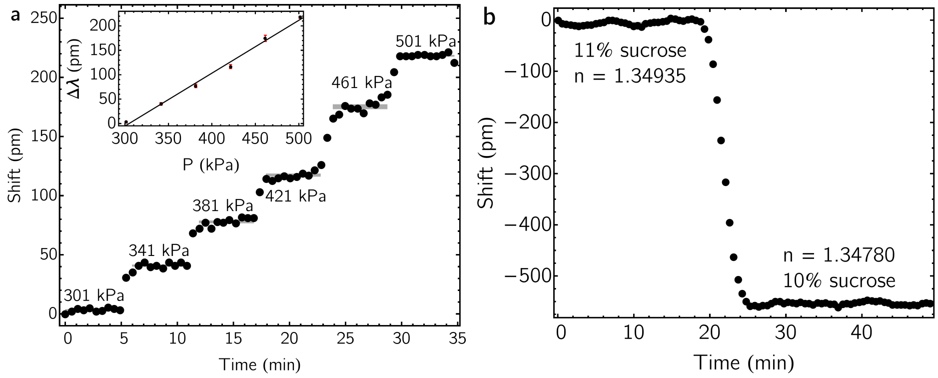

Figure 3.7 **a** Pressure sensorgram for Ar gas in a silver-mirrored capillary. The inset shows a linear fit to the mean resonance shifts, yielding a pressure sensitivity of 1.07 ± 0.02 nm/RIU. **b** Sensorgram as two concentrations of sucrose (11% w/w and 10% w/w) solution are pumped through the capillary

illary radius as before. There is no dependence on the reflectivity of the mirrors or the quality factor of the cavity. Mirror roughness (see Fig. 3.2) also doesn't matter insofar as the sensitivity is concerned, although it can decrease the visibility and thereby degrade the mode shift resolution and the LoD. Thus, the deciding factor controlling the refractometric sensitivity for these capillary sensors is the measurement wavelength, because it determines m independently of the radius (in other words, for a fixed resonant wavelength, there are many possible combinations of L and m but they all have the same refractometric sensitivity).

Using $S = 4R/m$, one predicts a refractometric sensitivity of 599 nm/RIU for both the polymer- and silver-mirrored channel near $\lambda = 600$ nm and $n = 1.002$ (Table 3.1). We observed $(4.7 \pm 0.3) \times 10^2$ and $(5.6 \pm 0.2) \times 10^2$ nm/RIU for the polymer and silver-mirrored capillaries, respectively. The experimental sensitivities tended to be somewhat lower than the theoretical values. One possible reason is that the Gladstone-Dale approximation used to calculate the RIs may overestimate the RI difference between Ar and N_2 at the measurement pressure.

A few other comments can also be made at this point. First, we see that the refractometric sensitivity is lower with liquid in the channel as compared to gas. At a fixed wavelength, increasing the RI of the channel medium increases the mode order correspondingly, thus lowering the sensitivity (opposite to the case of a WGM resonator, in which the sensitivity decreases for lower analyte index). These observations are also in agreement with the general trends predicted by the analysis above.

However, some discrepancies also exist. For example, the liquid sensitivity for Ag-mirrored channels (Table 3.1) is about 63% of the gas one, but the theory implies that it should be 75% of it (according to the ratio of channel refractive indices 1.00:1.33). Also, the lower "pressure LoD" for the Ag-mirrored devices as compared to the polymer ones is unexpected; from the above discussion one would expect them to be the same. We can't unambiguously explain this discrepancy, but we note that the Fourier spectra (from which the wavelength shifts are calculated) were much weaker in the polymer case than they were in the Ag one, due to the much lower visibility of the 2-3 resonances and the maximum-power component was not nearly as well defined. These differences affect the accuracy of the Fourier shift method [70] and could potentially be responsible for the different observed pressure LoDs (3.3 vs. 5.0 kPa for Ag and ppba mirrors, respectively).

A brief discussion of the error analysis appears necessary. The device sensitivities were calculated from the experimental wavelength shifts, which were obtained as the difference in the mean values of $\Delta\lambda$. The reported uncertainties come from quadrature addition of the standard error of the means (SE = $\sigma/n^{1/2}$), where σ is the sample standard deviation and n is the number of measurements for each shift value. The fact that the uncertainties are far smaller than the nominal "resolution" of the spectrometer isn't inconsistent because they simply come from the noise in the mode peak positions under constant conditions. For several of the runs,

Table 3.1 Summary of the experimental, simulated, and calculated sensitivities of polymer-coated and silver-mirrored capillaries in nm/RIU. Listed values are for wavelengths of 600 nm and 1550 nm, and near RIs of 1.002 (air) or 1.33 (water). Units are nm/RIU.

			Experiment	FDTD	Theory
600 nm	Poly	Air	468	530	599
		Water	—	420	452
	Ag	Air	565	516	599
		Water	354	412	452
1550 nm	Poly	Air	—	1574	1547
		Water	—	1128[a]	1165
	Ag	Air	—	1513	1547
		Water	—	1222	1165

[a] The FDTD result for water in the polymer-coated channel yielded low-visibility, low-Q modes that were difficult to analyze by Fourier methods, so the peak shift was estimated manually by choosing the highest point.

these values were very small, with a standard deviation of less than 1.5 pm. This error analysis does, however, ignore systematic errors which we do believe are significant but are difficult to quantify.

Since most of the Fabry-Perot fiber sensors cited in the literature were tested at a wavelength near 1550 nm, the sensitivity in the infrared would present a more consistent comparison with previous work. For Fabry-Perot-type cavities, the wavelength shift under a fixed index change is directly proportional to the central wavelength. Thus, at 1550 nm the sensitivity of the capillary device would be close to 1540 nm/RIU for air in the channel. This estimate is in reasonable agreement with FDTD simulations which gave a sensitivity of 1574 nm/RIU.

The best detection limit we could achieve was $(6.3 \pm 0.2) \times 10^{-6}$ RIU, taking the most stable experimental run to calculate the 3σ variation in the mode peak positions. The detection limit varies inversely with wavelength, due to the greater sensitivity of the proportionally smaller mode orders. Thus, at 1550 nm (as compared to 600 nm for the current measurements) the detection limit is predicted to be 2.3×10^{-6} RIU, which is also in excellent agreement with FDTD simulations.

Temperature cross-sensitivity is an issue for many sensors [137, 138]. The response to temperature fluctuations is due to thermal expansion which for silica is $5.5 \times 10^{-7}\,\mathrm{K}^{-1}$ [139], giving a relative change of a few parts in 10^5 for a temperature change of 100 °C, corresponding to a few pm of spectral drift. Since this is quite close to the shift resolution, one can conclude good thermal stability over a range of ~100 °C, but for larger temperature drifts the thermal expansion would have to be compensated. Of course, in an open system the thermo-optic coefficient of the gas would cause a change in the RI which may not be distinguishable from a change in pressure; whereas in a closed system both P and T would change concurrently and the effects would cancel insofar as one has an ideal gas.

There are several additional features of this device. No splicing, melting, femtosecond laser ablation [113, 136], or nanolithography is required as is usually the case for other sensors. Since the mode propagates mainly in the channel, the elasto-optic effect, which can be a problem for fiber sensors, is not important here. The compressibility of silica near atmospheric pressure is $9.8 \times 10^{-12}\,\mathrm{Pa}^{-1}$ [140], which would cause a redshift of a fraction of a picometer due to elastic expansion in this pressure range. The compressibility of ppba is unknown but the values for related polymers such as PMMA are on the order of $1.5 \times 10^{-10}\,\mathrm{Pa}^{-1}$ [141], and for silver it is ~$1 \times 10^{-11}\,\mathrm{Pa}^{-1}$ [142]. These values are about an order of magnitude larger than that of silica but would still cause negligibly small mode shifts as compared to the wavelength shift resolution (i.e., the polymer film thickness would change by a few parts in 10^5 over 200 kPa leading to a few pm of spectral drift, around 1% of the typical changes observed).

However, similar to other FP gas sensors, gas specificity is currently lacking. One can envision ways to overcome this problem in the future, such as, for example, by filling a capillary with a porous absorber. Indeed, this concept has recently been demonstrated for fluid biosensors [143]. Secondly, a small amount of heating is likely to occur in the sample. We did not make any temperature-stabilizing efforts here; but since the device only uses a comparatively weak white light source, thermal drifts should be minimal. Indeed, after the sample was allowed to stabilize for a few minutes we found no observable thermal drift in the reported sensorgrams after starting an experiment.

A final question concerns the value of a capillary-type FP sensor as compared to the fiber-optic sensors investigated previously. First, despite its simplicity a mirrored-capillary gas, liquid, and pressure sensor hasn't been shown before. In fact, the simplicity of the device is an attractive aspect since only a very straightforward fabrication is required and it could easily be parallelized to produce multiple devices. Secondly, sensitivity in the visible spectrum is as good as or better than in previously demonstrated FP devices, with predicted detection limits in the low 10^{-6} RIU range at a wavelength of 1.55 µm. Third, the light source is nothing more than a simple incandescent bulb. Finally, better mechanical stabilization (e.g., by packaging the capillary and light source) would likely lead to a smaller shift resolution and even better detection limits.

3.7 Conclusions

To conclude, we show a simple, robust refractometric gas sensor based on a capillary coated with a high-index polymer or metallic silver. The response is comparable to or better than many other optical gas sensors. A refractometric shift of 2.7×10^{-5} RIU was tested and an optimum detection limit of $(6.3 \pm 1.1) \times 10^{-6}$ RIU was found at a wavelength of ~600 nm. These values would further improve by a factor of ~2.6 at the infrared wavelengths used by other detection systems. The device can also function as a gas pressure sensor with a detection limit as low as 3.3 ± 0.1 kPa at λ = 600 nm, which is comparable to the best optical pressure sensors reported to date. The concept doesn't require any complicated equipment or preparation. The same concept was demonstrated for fluid sensing in the channel as well, again with competitive sensitivities and LoDs. The results were finally discussed in terms of the simple theory governing the sensitivity of FP-type refractometric sensors.

3.8 Acknowledgements

Natural Science and Engineering Research Council of Canada (NSERC) CREATE Program (grant 463990-2015); Australian Research Council (ARC) Georgina Sweet Laureate Fellowship.

We thank Sergei Vagin (Technische Universität München) for discussions on high-index polymers.

3.9 References

[1] W. Morrish et al. "Refractometric micro-sensor using a mirrored capillary resonator," *Optics Express* **24** (22), 24959–24970 (2016). DOI: `10.1364/OE.24.024959` (pp. iv, 32, 60).

[26] Y. Zhi, T. Thiessen, and A. Meldrum. "Silicon quantum dot coated microspheres for microfluidic refractive index sensing," *Journal of the Optical Society of America B-Optical Physics* **30** (1), 51–56 (2013). DOI: `10.1364/josab.30.000051` (pp. 2, 34, 75).

[33] C. P. K. Manchee et al. "Refractometric sensing with fluorescent-core microcapillaries," *Optics Express* **19** (22), 21540–21551 (2011). DOI: `10.1364/OE.19.021540` (pp. 2, 34, 59, 75).

[48] H. Y. Choi et al. “Miniature fiber-optic high temperature sensor based on a hybrid structured Fabry-Perot interferometer,” *Optics Letters* **33** (21), 2455–2457 (2008). DOI: `10.1364/ol.33.002455` (pp. 8, 34).

[61] A. Francois et al. “Polymer based whispering gallery mode laser for biosensing applications,” *Applied Physics Letters* **106** (3), (2015). DOI: `10.1063/1.4905931` (pp. 9, 34, 76).

[70] J. W. Silverstone et al. “Ultimate resolution for refractometric sensing with whispering gallery mode microcavities,” *Optics Express* **20** (8), 8284–8295 (Apr. 2012). DOI: `10.1364/OE.20.008284` (pp. 10, 29, 41, 42, 47, 65, 85).

[103] X. Wei and D. K. Roper. “Tin Sensitization for Electroless Plating Review,” *Journal of the Electrochemical Society* **161** (5), D235–D242 (2014). DOI: `10.1149/2.047405jes` (pp. 24, 38).

[104] X. Fan and I. M. White. “Optofluidic microsystems for chemical and biological analysis,” *Nature Photonics*. (2011). DOI: `10.1038/nphoton.2011.206` (p. 33).

[105] J. Jágerská et al. “Refractive index sensing with an air-slot photonic crystal nanocavity,” *Optics Letters* **35** (15), 2523–2525 (2010). DOI: `10.1364/ol.35.002523` (pp. 33, 34).

[106] H. Clevenson et al. “High sensitivity gas sensor based on high-Q suspended polymer photonic crystal nanocavity,” *Applied Physics Letters*. (2014). DOI: `10.1063/1.4879735` (p. 33).

[107] M. R. Foreman, J. D. Swaim, and F. Vollmer. “Whispering gallery mode sensors,” *Advances in Optics and Photonics* **7** (2), 168 (June 2015). DOI: `10.1364/aop.7.000168` (p. 33).

[108] Y.-J. Rao et al. “Micro Fabry-Perot interferometers in silica fibers machined by femtosecond laser,” *Optics Express*. (2007). DOI: `10.1364/oe.15.014123` (pp. 33, 34).

[109] A. Francois et al. "Whispering Gallery Mode Devices for Sensing and Biosensing," *Photonic Materials for Sensing, Biosensing and Display Devices*. Ed. by M. J. Serpe, Y. Kang, and Q. M. Zhang. Vol. 229. Springer Series in Materials Science. Cham: Springer International Publishing, 2016, 237–288. DOI: `10.1007/978-3-319-24990-2_9` (p. 33).

[110] T. Reynolds et al. "Optimization of whispering gallery resonator design for biosensing applications," *Optics Express*. (2015). DOI: `10.1364/oe.23.017067` (pp. 33, 59).

[111] Y. Zhang et al. "Functional Investigation of Effects on Transplantable Bone Marrow Stem Cells Label with Iron Oxide Nanoparticles," *Journal of Biomaterials and Tissue Engineering* **5** (6), 486–492 (June 2015). DOI: `10.1166/jbt.2015.1298` (p. 33).

[112] R. St-Gelais, J. Masson, and Y. A. Peter. "All-silicon integrated Fabry-Peacuterot cavity for volume refractive index measurement in microfluidic systems," *Applied Physics Letters* **94** (24), (2009). DOI: `10.1063/1.3152286` (p. 33).

[113] T. Wei et al. "Temperature-insensitive miniaturized fiber inline Fabry-Perot interferometer for highly sensitive refractive index measurement," *Optics Express* **16** (8), 5764–5769 (2008). DOI: `10.1364/oe.16.005764` (pp. 33, 34, 49).

[114] S. Pang, R. E. Beckham, and K. E. Meissner. "Quantum dot-embedded microspheres for remote refractive index sensing," *Applied Physics Letters* **92** (22), (2008). DOI: `10.1063/1.2937209` (p. 34).

[115] P. Zijlstra, K. L. van der Molen, and A. P. Mosk. "Spatial refractive index sensor using whispering gallery modes in an optically trapped microsphere," *Applied Physics Letters* **90** (16), (2007). DOI: `10.1063/1.2722695` (p. 34).

[116] I. M. White and X. Fan. "On the performance quantification of resonant refractive index sensors," *Optics Express* **16** (2), 1020–1028 (2008). DOI: `10.1364/OE.16.001020` (pp. 34, 42, 60).

[117] D.-W. Duan et al. "Microbubble based fiber-optic Fabry-Perot interferometer formed by fusion splicing single-mode fibers for strain measurement," *Applied Optics* **51** (8), 1033–1036 (2012). DOI: `10.1364/ao.51.001033` (p. 34).

[118] C. R. Liao, T. Y. Hu, and D. N. Wang. "Optical fiber Fabry-Perot interferometer cavity fabricated by femtosecond laser micromachining and fusion splicing for refractive index sensing," *Optics Express* **20** (20), 22813–22818 (2012). DOI: `10.1364/oe.20.022813` (p. 34).

[119] Y. Guo et al. "Optofluidic Fabry-Perot cavity biosensor with integrated flow-through micro-/nanochannels," *Applied Physics Letters* **98** (4), (2011). DOI: `10.1063/1.3548673` (p. 34).

[120] W. Z. Song et al. "Refractive index measurement of single living cells using on-chip Fabry-Perot cavity," *Applied Physics Letters* **89** (20), (2006). DOI: `10.1063/1.2387965` (p. 34).

[121] S. Calixto et al. "Capillary refractometer integrated in a microfluidic configuration," *Applied Optics* **47** (6), 843–848 (2008). DOI: `10.1364/ao.47.000843` (p. 34).

[122] H. El Ghandoor et al. "Measuring the refractive index of crude oil using a capillary tube interferometer," *Optics and Laser Technology* **35** (5), 361–367 (2003). DOI: `10.1016/s0030-3992(03)00029-x` (p. 34).

[123] B. Krattiger et al. "Laser-based refractive-index detection for capillary electrophoresis: ray-tracing interference theory," *Applied Optics* **32** (6), 956 (1993). DOI: `10.1364/ao.32.000956` (p. 34).

[124] S. W. Qi et al. "Analysis of capillary interferometry for measuring refractive indices of minute samples," *Applied Optics* **43** (3), 530–536 (2004). DOI: `10.1364/ao.43.000530` (p. 34).

[125] H. J. Tarigan et al. "Capillary-scale refractive index detection by interferometric backscatter," *Analytical Chemistry* **68** (10), 1762–1770 (1996). DOI: `10.1021/ac9511455` (p. 34).

[126] A. Yang et al. "Measuring the refractive indices of liquids with a capillary tube interferometer," *Applied Optics* **45** (31), 7993–7998 (2006). DOI: `10.1364/ao.45.007993` (p. 34).

[127] S. Surdo et al. "Optofluidic microsystems with integrated vertical one-dimensional photonic crystals for chemical analysis," *Lab on a Chip* **12** (21), 4403–4415 (2012). DOI: `10.1039/c2lc40613f` (p. 34).

[128] S. Surdo et al. "Capillarity-driven (self-powered) one-dimensional photonic crystals for refractometry and (bio) sensing applications," *Rsc Advances* **4** (94), 51935–51941 (2014). DOI: `10.1039/c4ra09056j` (p. 34).

[129] O. Svelto et al. "Lasers and Coherent Light Sources," *Springer Handbook of Lasers and Optics*. Ed. by F. Träger. New York, NY: Springer New York, 2007, 583–936. DOI: `10.1007/978-0-387-30420-5_11` (p. 36).

[130] URL: `http://www.polysciences.com/default/pentabromophenyl-acrylate`.

[131] E. Klantsataya et al. "Effect of surface roughness on metal enhanced fluorescence in planar substrates and optical fibers," *Optical Materials Express* **6** (6), 2128–2138 (2016). DOI: `10.1364/ome.6.002128` (pp. 38, 44).

[132] Y. Clergent, C. Durou, and M. Laurens. “Refractive index variations for argon, nitrogen, and carbon dioxide at lambda = 632.8 nm (He-Ne laser light) in the range 288.15K <= T <= 323.15K, 0 < p < 110 kPa,” *Journal of Chemical and Engineering Data* **44** (2), 197–199 (1999). DOI: `10.1021/je980133o` (pp. 42, 161).

[133] F. Carpignano et al. “Refractive Index Sensing in Rectangular Glass Micro-Capillaries by Spectral Reflectivity Measurements,” *Ieee Journal of Selected Topics in Quantum Electronics* **22** (3), (2016). DOI: `10.1109/jstqe.2015.2455339` (p. 42).

[134] M. Piliarik and J. J. Homola. “Surface plasmon resonance (SPR) sensors: approaching their limits?,” *Optics Express* **17** (19), 16505–16517 (2009). DOI: `10.1364/oe.17.016505` (pp. 42, 60).

[135] G. Liu and M. Han. “Fiber-optic gas pressure sensing with a laser-heated silicon-based Fabry-Perot interferometer,” *Optics Letters* **40** (11), 2461–2464 (2015). DOI: `10.1364/ol.40.002461` (p. 43).

[136] B. Xu et al. “Fiber-tip gas pressure sensor based on dual capillaries,” *Optics Express* **23** (18), 23484–23492 (2015). DOI: `10.1364/oe.23.023484` (pp. 43, 49).

[137] E. Pinet. “Pressure measurement with fiber-optic sensors: Commercial technologies and applications,” *21st International Conference on Optical Fiber Sensors*. Ed. by W. J. Bock, J. Albert, and X. Bao. Vol. 7753. Proceedings of SPIE. 2011. DOI: `10.1117/12.895536` (p. 49).

[138] Y. Z. Zhu et al. “High-temperature fiber-tip pressure sensor,” *Journal of Lightwave Technology* **24** (2), 861–869 (2006). DOI: `10.1109/jlt.2005.862444` (p. 49).

[139] URL: `https://www.crystran.co.uk/optical-materials/silica-glass-sio2`.

[140] W. B. Emerson. “Compressibility of fused-quartz glass at atmospheric pressure,” *Journal of Research of the National Bureau of Standards* **18** (6), 683–711 (1937). DOI: `10.6028/jres.018.044` (p. 49).

[141] S. B. Sane and W. G. Knauss. “The time-dependent bulk response of Poly (Methyl Methacrylate),” *Mechanics of Time-Dependent Materials* **5** (4), 293–324 (2001). DOI: `10.1023/a:1012517421899` (p. 49).

[142] J. J. Xie et al. “First-principles calculation of the thermal properties of silver,” *Physical Review B* **59** (2), 965–969 (1999). DOI: `10.1103/PhysRevB.59.965` (p. 49).

[143] J. Mai et al. “Rapid detection of trace bacteria in biofluids using porous monoliths in microchannels,” *Biosensors & Bioelectronics* **54**. 435–441 (2014). DOI: `10.1016/j.bios.2013.11.012` (p. 50).

Chapter 4

Geometric resonances for high-sensitivity microfluidic lasing sensors

A modified version of this chapter was published as W. Morrish et al. “Geometric Resonances for High-Sensitivity Microfluidic Lasing Sensors,” Physical Review Applied ***10*** *(5), 051001 (Nov. 2018).* DOI*:* *`10.1103/PhysRevApplied.10.051001`*. *© 2018 American Physical Society*

4.1 Abstract

Microcapillaries are inherently fluidic sensing platforms that can, under appropriate conditions, support lasing. We propose and demonstrate a lasing microcapillary sensor based on “star” and “triangle” interferences arising from reflection and refraction at the inner and outer microcapillary walls. These interferences lead to distinct modal trajectories that sample the channel medium inside the microcavity structure. Both star and triangle resonances are therefore sensitive to the nature of the channel

medium, yielding theoretical and experimental sensitivities significantly exceeding those found for sensors based on conventional whispering-gallery modes. Additional enhancement can be achieved because the two main resonance families shift in an opposite sense, yielding a differential sensitivity that can reach several thousand nanometers per refractive index “unit”. These devices represent a robust, yet easily fabricated optical sensor and capillary-based lasing system for microfluidic sensing.

4.2 Introduction

Microcavity resonators are a natural fit for sensing applications. They are compact and can measure changes in humidity [35], temperature [36], and force [38]. They can measure chemical reactions [144] and can be functionalized to detect specific proteins [40], DNA [17], viruses [110], and individual nanoparticles [34]. Microcapillaries also provide an intrinsic flow-through capability, whereas other geometries, such as microspheres, disks, and fiber-based resonators, require more-complicated external channels and sampling chambers.

Two main capillary-type microcavity sensors have been proposed. Liquid-core-optical-ring-resonator sensors (LCORRS) are capillaries whose walls have been thinned below 5 μm [19]. Light is then coupled into the whispering-gallery modes (WGMs) through the use of a phase-matched waveguide or fiber taper, which requires sub-micron positioning apparatus and/or a narrow-bandwidth tunable laser. LCORRS are also fragile and their fabrication can require injection and pumping of hydrofluoric acid.

Fluorescent-core microcavities (FCMs) are standard thick-walled microcapillaries with a high-refractive-index fluorescent layer on the inside of the capillary channel [33]. The WGMs can be observed in the fluorescence emitted from the channel coating. While FCMs are more robust and easier to prepare, their drawbacks include low light levels, low Q factors of typically 1000, and relatively low refractometric sensitivity [30]. While lasing FCMs can alleviate the first two issues to some degree [145], the lasing is subject to photobleaching and does not increase the sensitivity.

LCORRSs and FCMs typically have sensitivities (S) of 5–30 nm per refractive index "unit" (RIU), although the high-order radial modes can reach 200 nm/RIU [146] or 570 nm/RIU [147], respectively. A sensitivity of 967 nm/RIU was achieved in capillary resonators having a layered structure with outwardly decreasing refractive indices [148]. Surface-plasmon resonators typically show comparatively lower sensitivities [134]; whereas Fabry-Perot cavities [1, 149] and photonic crystals [150] can achieve values near 1000 nm/RIU. Specially designed devices such as coupled optofluidic ring lasers can reach even higher values [20]. The detection limit for refractometric devices is generally defined as $L_d = R_e/S$, where R_e is the "resolution" of the sensor, which is based on the noise present in a given configuration [116]. For capillaries, the detection limit ranges from 10^{-4} to 10^{-6} RIU depending on the geometry. Surface-plasmon sensors can routinely achieve detection limits of 10^{-6} RIU [134], the detection limits of Fabry-Perot cavities range from 10^{-4} to 10^{-6} RIU [1, 149], and the detection limit of optofluidic ring lasers reaches 10^{-7} RIU [20].

Here we demonstrate a novel lasing capillary sensor that is both robust and sensitive by using geometric modes in the lasing regime. We start by analyzing the trajectories of these modes and derive an equation for their sensitivity. We then fabricate devices, characterize the resonances, and measure the sensitivity experimentally. We find two families of lasing modes that shift in an opposite sense as a function of the analyte refractive index, reaching sensitivities significantly greater than those of other capillary-based devices.

4.3 Theory

There are two types of resonance that can be supported. In the first type, light travels around the full circumference of the capillary, periodically refracting into the glass wall [Fig. 4.1 **a**]. If the path difference after one round trip is an integer number of wavelengths, a "star-mode" resonance will form. These modes require that the refracted ray approaches the outer boundary at an angle larger than the critical angle. The resonant wavelengths obtained by geometric analysis are

$$\lambda_{\mathrm{TE,TM}} = \frac{2N}{m - N(\phi_{\mathrm{TE,TM},2}/(2\pi))}\left(\frac{Rn_2^2 \sin\alpha}{n_1 \cos\psi} + rn_1 \sin\alpha\right), \tag{4.1}$$

where λ is the mode wavelength, order N represents the number of points on the star, m is the mode number (i.e., the number of wavelengths in the optical path), $\phi_{\mathrm{TE,TM},2}$ is the phase change on total internal reflection at surface 2 for TE- or TM-polarized modes, R is the outer radius of the capillary, r is the inner radius of the capillary, n_1 is the refractive index inside the channel, n_2 is the refractive index of the glass wall, α is the half-angle subtended by the points of incidence for the ray that refracts into the glass wall and returns to surface 1 [Fig. 4.1 **c**, line ABC], and ψ is the half-angle subtended by the path that reflects through the channel [Fig. 4.1 **a**, line AC]. The phase shifts on internal reflection from surface 2 are calculated from the Fresnel equations.

The star modes have the constraint that $N(\psi + \alpha) = \pi$, establishing a limit on the possible values of N. For example, in capillaries with $n_1 = 1.348$, a 125-µm inner radius, and a 160-micro m outer radius, the only allowable values of N are integers 5–8. To find the resonant wavelengths, we write the angle α in terms of the other parameters:

$$\alpha = \sin^{-1}\left(\frac{n_1}{n_2}\cos\psi\right) - \sin^{-1}\left(\frac{rn_1}{Rn_2}\cos\psi\right). \tag{4.2}$$

Pairs of angles ψ and α can be calculated by solving Eq. 4.2 numerically, and then the resonant wavelengths can be calculated from Eq. 4.1.

The sensitivity of the star modes can be determined by taking the derivative of Eq. 4.1 with respect to n_1 for either polarization. We focus on the TE case (i.e., electric field parallel to the capillary axis), although the TM result is similar. Since many of the variables in Eq. 4.1 are themselves dependent on n_1, the derivative has no simple analytical solution. We therefore solve $\mathrm{d}\lambda/\mathrm{d}n_1$ numerically, finding sensitivities up to 350 nm/RIU for capillaries with the largest r/R ratio, as shown in Fig. 4.2 **a**. In general, star-mode sensitivities decrease with increasing orders, while sensitivity increases as the r/R ratio increases.

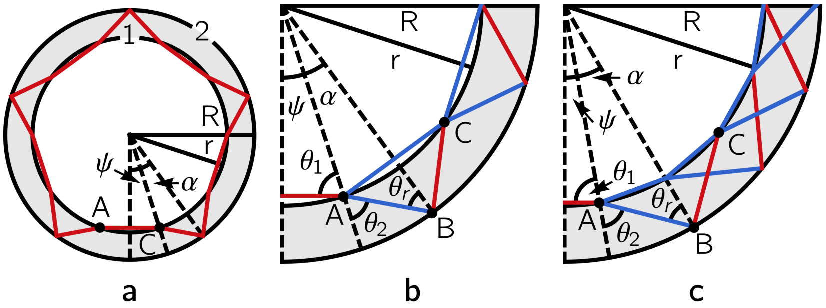

Figure 4.1 Ray diagrams showing possible resonance configurations. Inner and outer capillary surfaces are labeled 1 and 2, respectively, θ_2 is the angle of refraction after light enters the glass wall, and θ_r is the angle of reflection at surface 2. Other symbols are defined after Eq. 4.1. **a** A ray reflects off the glass-air interface five times. **b**, **c** An incoming ray is split into two paths via Fresnel reflection and recombines after either one reflection **b** or two reflections **c** of the internal ray.

In the second type of resonance, a wave propagating through the capillary channel is incident on the glass wall, splits into a reflected and refracted component at point A, and recombines again at point C [Figs. 4.1 **b** and 4.1 **c**]. If these rays interfere in phase, they form a “triangle” resonance. Building upon a simpler analysis [44], we find the condition for a triangle is

$$\lambda_{\mathrm{TE,TM}} = \frac{2\left(v\frac{Rn_2^2\sin\alpha}{n_1\cos\psi} - urn_1\sin\psi\right)}{m - v\frac{\phi_{\mathrm{TE,TM},2}}{2\pi} - u\frac{\phi_{\mathrm{TE,TM},1}}{2\pi}}, \tag{4.3}$$

where u and v are integers such that $u\psi = v\alpha$, and the phase shifts on reflection at surface 1 are $\phi_{\mathrm{TE},1} = \pi$ and $\phi_{\mathrm{TM},1} = 0$ when $\sin^{-1}(\cos\phi) < \tan^{-1}(n_2/n_1)$ and π otherwise. In the case of $u = v$ [i.e., when the two angles are the same as in Fig. 4.1 **c**],

$$\psi = \arccos\left[\frac{1}{12rRn_1^2}(2w - w^2zy^{-1/3} - y^{1/3}z^*)\right], \tag{4.4}$$

where $w = r^2n_1^2 + R^2n_1^2 + R^2n_2^2$, $x = 9r^2R^4n_1^4n_2^2$, $y = w^3 - 6x + (36x^2 - 12w^3x)^{1/2}$, and $z^* = 1 - 3^{1/2}i$.

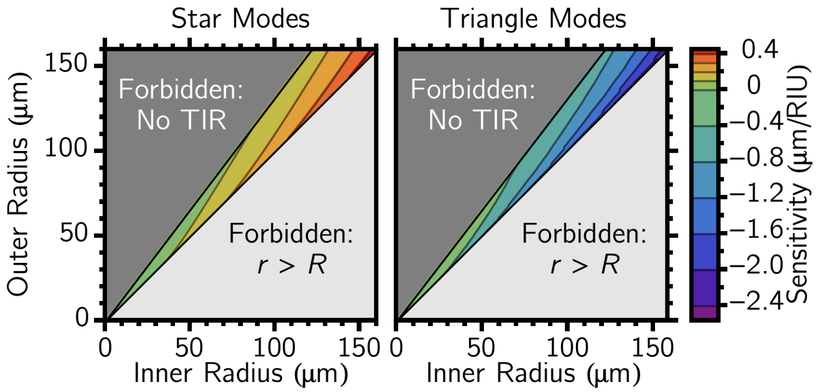

Figure 4.2 Theoretical sensitivities of the TE-polarized modes for inner and outer capillary radii up to 160 µm. Failure of total internal reflection (TIR) due to the small angle of incidence prevents lasing in the upper “forbidden” regions. The lower forbidden region has inner radius exceeding the outer radius.

When $u = 1$, the inner ray path goes straight from point A to point C; if

$u = 2$, there is an additional inner-wall reflection [Fig. 4.1 **c**]. If $v = 2$, then there are two outer-wall reflections, making a "double-triangle" mode. The triangle-mode sensitivity is the derivative of Eq. 4.3 with respect to n_1. When $u = v$, the sensitivity is negative and larger than for the star modes [Fig. 4.2 **b**], reaching thousands of nanometers per RIU for increasing r/R ratio. The star and triangle modes can also be coupled (i.e., they can have the same resonant wavelength) as in the experiment to follow.

For both the star and the triangle modes, total internal reflection must occur at surface 2. This places a lower cutoff for the ratio of the inner radius and outer radius of approximately 0.75 for the refractive indices used in the experimental demonstration, although it weakly depends on the mode orders N (star modes) or u and v (triangle modes). There is technically no upper limit to the radius ratio, although eventually one returns to the situation in which the mode spectrum is dominated by the WGMs, which are formed by reflections at surface 2 only.

The free spectral range (FSR) generally defines the dynamic range that can be achieved in a sensing experiment. The star-mode FSR is

$$\Delta f_{\text{star}} = \frac{c n_1 \cos\psi}{2N(R n_2^2 \sin\alpha + r n_1^2 \sin\psi \cos\psi)}, \tag{4.5}$$

whereas for triangle modes

$$\Delta f_{\text{triangle}} = \frac{c n_1 \cos\psi}{2(v R n_2^2 \sin\alpha + u r n_1^2 \sin\psi \cos\psi)}. \tag{4.6}$$

The star modes have a small spacing, similar to WGMs for capillaries of the same size, where $\Delta f_{\text{WGM}} = c/(2\pi R n_2)$ and c is the speed of light. $\Delta f_{\text{triangle}}$ is approximately 20 times larger than Δf_{star}, implying a larger range relative to the sensitivity.

4.4 Experimental methods

Test devices are prepared from standard 125-µm-inner-radius and 160-µm-outer-radius fused-silica microcapillaries ($n \approx 1.458$ at 600 nm [151]). The polyimide coating is removed by ashing under flowing oxygen in a tube furnace at 923 K. The inner and outer radii are modified by heating the capillaries with a graphite filament and gently pulling them until they reached the desired radius. The r/R ratios are 52:71, 69:91, 84:114, 99:134, and 121:161 as estimated by optical microscopy (Fig. 4.3). Each capillary is connected to polytetrafluoroethylene tubing and affixed to a stage mounted above an objective lens. The test analyte is 1 mM Rhodamine B dissolved in aqueous solutions of either 10 or 11 wt % sucrose ($n_1 = 1.3478$ and 1.3494 at 600 nm, respectively [152]), which are pumped through the tubing and into the capillary channel with a syringe pump. The capillaries are illuminated with a Photon Technology GL-302 dye laser (500 nm, 3 Hz, pulse length approximately 1 ns), and the emission is measured with an imaging spectrometer. The mode shifts are determined by Fourier analysis [70].

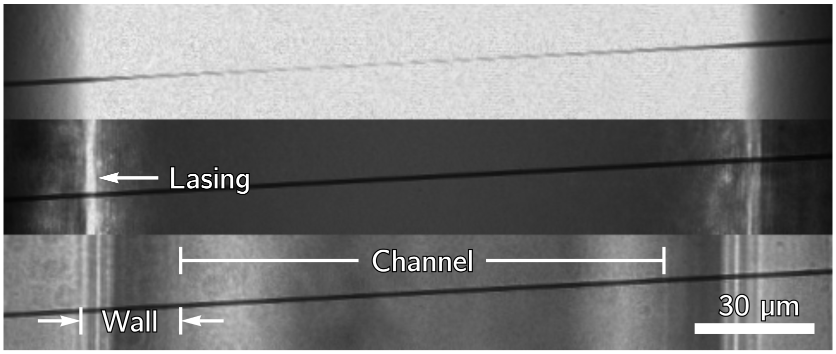

Figure 4.3 Optical images of a vertically oriented capillary with radius ratio of 69:91 filled with 1 mM aqueous Rhodamine B under 532 nm CW-laser illumination (upper) and under 500 nm pulsed-laser illumination (middle), and an empty capillary under white light (lower). The black line is the spectrometer entrance slit.

4.5 Results and discussion

The spectra show a set of periodic, narrowly spaced modes for the various radius ratios examined (Fig. 4.4). The narrowness of these modes combined with the threshold behavior is indicative of lasing. Below the threshold, no modes are visible in the spectrum because the fluorescence is dominated by the bulk fluid in the channel. For the star modes, the calculated FSR is 0.27 nm, in close agreement with the 0.26-nm spacing between adjacent lasing modes for radius ratio 121:161. With this identification, the Q factors for the star modes increase with capillary radius, ranging from approximately 3800 for the smallest capillaries to approximately 6000 for the largest as measured by dividing the central wavelength of a peak by its full width at half maximum. The triangle modes have a much larger calculated spacing of 5.9 nm, approximately consistent with the experimental results shown in Fig. 4.4, in which the envelope mode spacing is approximately 5.4 nm (i.e., the spacing between the groups of lasing modes). The width of the triangle-mode envelope and the underlying star-mode structure do, however, make it hard to measure the triangle-mode FSR, possibly explaining the difference between the calculated and experimental values. Although the Q factor of the triangle modes is difficult to estimate due to the complicated underlying star-mode structure, the evidently low value is expected due to low reflectivity at surface 1 [44]. Additionally, a higher-order triangle mode [$u = 2$; Fig. 4.1 **c**] appears in the spectrum, with a measured FSR of approximately 5.8 nm, with a fairly large uncertainty.

The sensitivities are experimentally determined by collecting a series of spectra represented in Fig. 4.5. Triangle and star modes with differing modal parameters should produce a large set of peaks in the Fourier spectrum, and, indeed, a complex spectrum with several maxima is observed. Mode shifts are followed by monitoring the phases of the Fourier components that agreed with the calculated modal frequencies [Fig. 4.6 **a**].

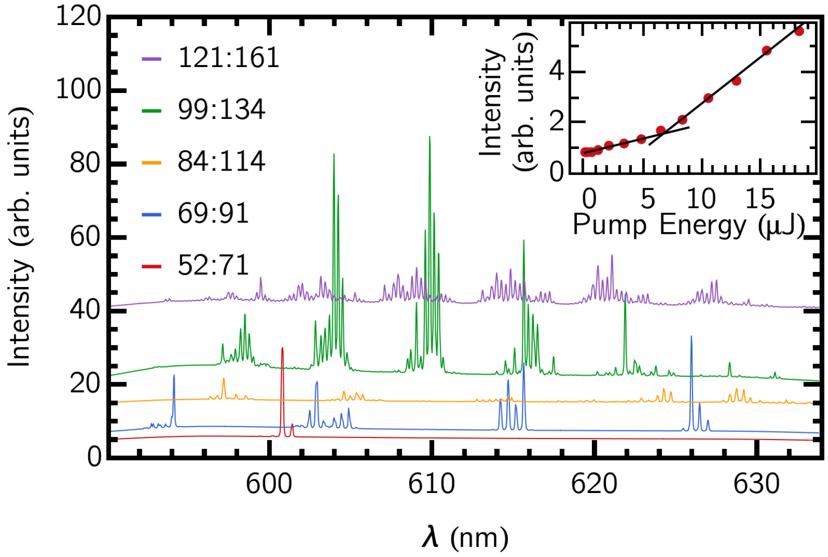

Figure 4.4 Lasing spectra for capillaries of various inner and outer radii given in micrometers. The groups of lasing peaks are star modes modulated by a triangle-mode envelope. Only these coupled modes appear to lase. The inset shows the lasing threshold for the capillary with radius ratio of 121:161.

The phase shifts can then be recast as wavelength shifts, resulting in the sensor read-out shown in Fig. 4.6 **b**. The triangle-mode envelope shows a large blueshift and the star modes show a smaller redshift in the sensor read-out, as predicted by the theoretical analysis.

The calculated sensitivity of these modes can also be compared with the experimental values. The $R = 161$μm capillary demonstrates sensitivities of 147 and −767 nm/ RIU for the star and triangle modes, respectively. These correspond to calculated sensitivities of 135 and −794 nm/RIU for $N = 5$ and $u = 1$, which appears to be reasonably good agreement given the experimental uncertainties. Since these two sets of modes have sensitivities of the opposite sign, they can be combined to achieve a sensitivity higher than either can provide alone. This yields a sensitivity of 914 nm/RIU experimentally and 929 nm/RIU from the theory.

The sensitivity of the other capillaries is also measured, yielding star-mode values of 111, 160, 227, and 139 nm/RIU for the devices with radius ratios of 52:71, 69:91, 84:114, and 99:134, respectively. The triangle-mode sensitivities of these same capillaries are −856, −743, −828, and −991 nm/RIU, again in good agreement with the theoretical calculations described above and confirming that combined sensitivities in excess of 1000 nm/RIU can be achieved. The theory shows that even better values can be easily obtained (Fig. 4.2).

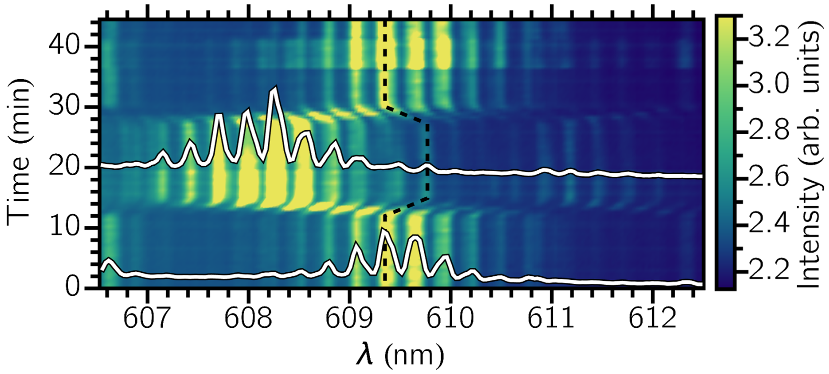

Figure 4.5 Density plot illustrating a sensing run. Two spectra are overlaid in white. A 10 wt% aqueous sucrose solution is pumped through the capillary, followed by 11 wt% at approximately 12 min, and 10 wt% solution is reintroduced at approximately 28 min.

To calculate the detection limit, the wavelength resolution R_e is defined as 3 times the standard deviation of the data during a period where no change occurs. With the definition $L_d = R_e/S$, the data in Fig. 4.6 **b** yield detection limits of 3.4×10^{-5} RIU for the triangle modes and 2.5×10^{-5} RIU for the star modes. The main limitation is the jitter in the data for the triangle modes, which are harder to clearly isolate in the Fourier spectrum. In the most stable runs, however, the 3σ resolution is good enough to imply a detection limit in the mid-10^{-6} range.

Unlike WGM-based capillary lasers that rely on organic dyes in solid media [145], here the lasing modes show no bleaching over an entire experiment (i.e., 45 min). The fresh solution continuously pumped through the capillary channel minimizes oxidative effects from the excitation of triplet states common to organic chromophores. Furthermore, specific detection via surface functionalization is possible in principle, since the star and triangle modes depend on the optical properties of surface 1. The main drawback is that the fluid must contain a lasing chromophore, which may limit the range of analytes. However, this arrangement can also be desirable, such as when proteins or cells are tagged with laser dyes [153].

4.6 Conclusions

The star and triangle "geometric" modes of conventional microcapillaries can be used for a lasing sensor that demonstrates a combined theoretical sensitivity up to several thousand nanometers per RIU at visible wavelengths and yields a detection limit in the range from 10^{-5} to 10^{-6} RIU, depending on the stability of the experimental setup and the capillary radii. The lasing-mode structure is shown to be the result of two sets of coupled modes: closely spaced modes created as light travels in a star-shaped path around the capillary, and more-widely-spaced ones created by interference between the reflected and transmitted waves at the channel wall. The capillaries are also robust and require little preparation, thus representing an attractive option for microfluidic sensing in the lasing regime.

4.7 Acknowledgements

The authors thank NSERC (CREATE Grant No. 463990-2015) for financial support.

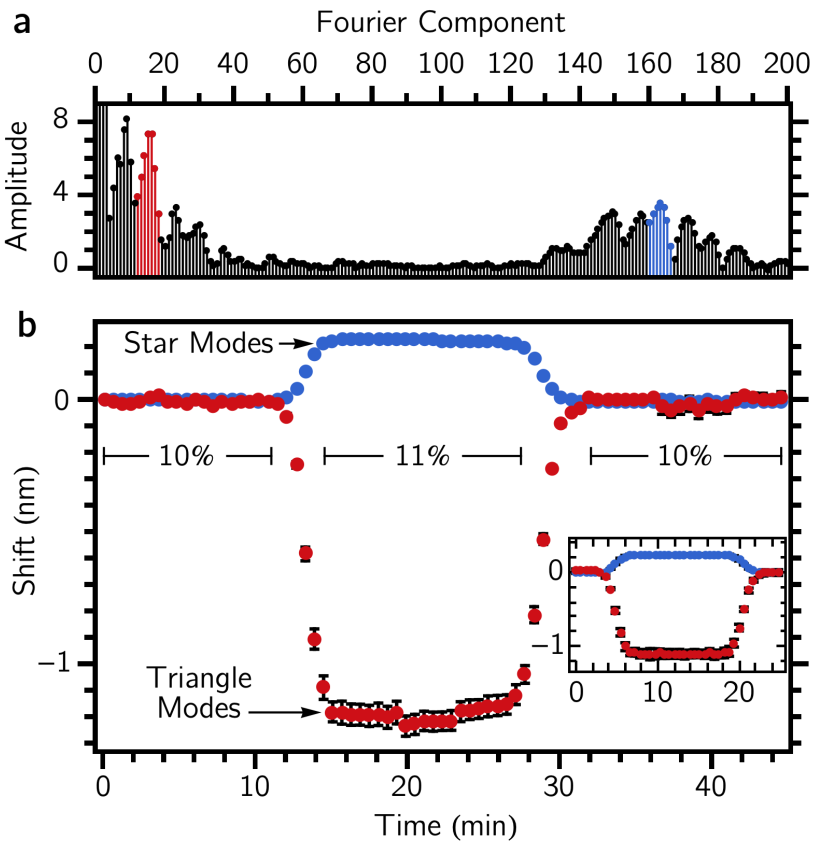

Figure 4.6 **a** Discrete Fourier transform of the lasing spectrum of a capillary with 160-µm outer radius. Colors indicate the components used to create the read-out in **b**. **b** Sensor read-out with 10 and 11 wt% aqueous sucrose solutions. The error bars are smaller than the data points in most cases. The inset shows the sensor read-out of the same capillary with TE polarization.

4.8 References

[1] W. Morrish et al. "Refractometric micro-sensor using a mirrored capillary resonator," *Optics Express* **24** (22), 24959–24970 (2016). DOI: 10.1364/OE.24.024959 (pp. iv, 32, 60).

[2] W. Morrish et al. “Geometric Resonances for High-Sensitivity Microfluidic Lasing Sensors,” *Physical Review Applied* **10** (5), 051001 (Nov. 2018). DOI: `10.1103/PhysRevApplied.10.051001` (pp. iv, 58, 77, 80, 85).

[17] M. D. Baaske, M. R. Foreman, and F. Vollmer. “Single-molecule nucleic acid interactions monitored on a label-free microcavity biosensor platform,” *Nature Nanotechnology* **9**. 933 (2014). DOI: `10.1038/nnano.2014.180` (pp. 2, 59, 75).

[19] M. Sumetsky et al. “Optical liquid ring resonator sensor,” *Optics Express* **15** (22), 14376–14381 (2007). DOI: `10.1364/OE.15.014376` (pp. 2, 59).

[20] X. Zhang et al. “Coupled optofluidic ring laser for ultrahigh- sensitive sensing,” *Optics Express* **19** (22), 22242–22247 (2011). DOI: `10.1364/OE.19.022242` (pp. 2, 60).

[30] A. Meldrum et al. “Luminescent Capillary-Based Whispering Gallery Mode Sensors: Crossing the Lasing Threshold,” *Physica Status Solidi (a)* **1700619** (7), 1700619 (2017). DOI: `10.1002/pssa.201700619` (pp. 2, 7, 60).

[33] C. P. K. Manchee et al. “Refractometric sensing with fluorescent-core microcapillaries,” *Optics Express* **19** (22), 21540–21551 (2011). DOI: `10.1364/OE.19.021540` (pp. 2, 34, 59, 75).

[34] H. Li et al. “Analysis of single nanoparticle detection by using 3-dimensionally confined optofluidic ring resonators,” *Optics Express* **18** (24), 25081–25088 (2010). DOI: `10.1364/OE.18.025081` (pp. 2, 59).

[35] A. K. Mallik et al. “Agarose coated spherical micro resonator for humidity measurements,” *Optics Express* **24** (19), 21216–21227 (2016). DOI: `10.1364/OE.24.021216` (pp. 2, 59).

[36] I. Hernández-Romano et al. "Optical fiber temperature sensor based on a microcavity with polymer overlay," *Optics Express* **24** (5), 5654–5661 (2016). DOI: `10.1364/OE.24.005654` (pp. 2, 59).

[38] T. Ioppolo et al. "Micro-optical force sensor concept based on whispering gallery mode resonators," *Applied Optics* **47** (16), 3009–3014 (2008). DOI: `10.1364/AO.47.003009` (pp. 2, 59).

[40] S. Lane et al. "Protein biosensing with fluorescent microcapillaries," *Optics Express* **23** (3), 2577–2590 (Feb. 2015). DOI: `10.1364/OE.23.002577` (pp. 3, 9, 10, 59, 76, 79, 89).

[44] H.-J. Moon and D.-Y. Kang. "Strongly enhanced mode selection in a thin dielectric-coated layered microcavity laser," *Optics Letters* **32** (11), 1554–1556 (2007). DOI: `10.1364/OL.32.001554` (pp. 7, 63, 66, 77).

[70] J. W. Silverstone et al. "Ultimate resolution for refractometric sensing with whispering gallery mode microcavities," *Optics Express* **20** (8), 8284–8295 (Apr. 2012). DOI: `10.1364/OE.20.008284` (pp. 10, 29, 41, 42, 47, 65, 85).

[110] T. Reynolds et al. "Optimization of whispering gallery resonator design for biosensing applications," *Optics Express*. (2015). DOI: `10.1364/oe.23.017067` (pp. 33, 59).

[116] I. M. White and X. Fan. "On the performance quantification of resonant refractive index sensors," *Optics Express* **16** (2), 1020–1028 (2008). DOI: `10.1364/OE.16.001020` (pp. 34, 42, 60).

[134] M. Piliarik and J. J. Homola. "Surface plasmon resonance (SPR) sensors: approaching their limits?," *Optics Express* **17** (19), 16505–16517 (2009). DOI: `10.1364/oe.17.016505` (pp. 42, 60).

[144] S. H. Huang et al. "Whispering gallery mode resonator sensor for in situ measurements of hydrogel gelation," *Optics Express* **26** (1), 51–62 (2018). DOI: `10.1364/OE.26.000051` (p. 59).

[145] A. François et al. “Lasing of whispering gallery modes in optofluidic microcapillaries,” *Optics Express* **24** (12), 12466–12477 (2016). DOI: `10.1364/OE.24.012466` (pp. 60, 68).

[146] V. Zamora, Z. Zhang, and A. Meldrum. “Refractometric Sensing of Heavy Oils in Fluorescent Core Microcapillaries,” *Oil Gas Sci. Technol. – Rev. IFP Energies nouvelles* **70** (3), 487–495 (2015). DOI: `10.2516/ogst/2013113` (p. 60).

[147] H. Li and X. Fan. “Characterization of sensing capability of optofluidic ring resonator biosensors,” *Applied Physics Letters* **97** (1), (2010). DOI: `10.1063/1.3462296` (p. 60).

[148] T. Ling and L. J. Guo. “Sensitivity enhancement in optical microtube resonator sensors via mode coupling,” *Applied Physics Letters*. (2013). DOI: `10.1063/1.4813007` (p. 60).

[149] G. Rigamonti et al. “Flow-through micro-capillary refractive index sensor based on T/R spectral shift monitoring,” *Biomedical Optics Express* **8** (10), 4438–4453 (2017). DOI: `10.1364/BOE.8.004438` (p. 60).

[150] F. Sun et al. “High quality factor and high sensitivity photonic crystal rectangular holes slot nanobeam cavity with parabolic modulated lattice constant for refractive index sensing,” *Optics Communications* **399**. 56–61 (Sept. 2017) (p. 60).

[151] I. H. Malitson. “Interspecimen Comparison of the Refractive Index of Fused Silica*,†,” *Journal of the Optical Society of America* **55** (10), 1205–1209 (1965). DOI: `10.1364/JOSA.55.001205` (pp. 65, 77).

[152] J. R. Rumble. “CRC Handbook of Chemistry and Physics,” 98th ed. Boca Raton, FL: CRC Press/Taylor & Francis (p. 65).

[153] Y.-C. Chen, Q. Chen, and X. Fan. “Lasing in blood,” *Optica* **3** (8), 809 (2016). DOI: `10.1364/optica.3.000809` (pp. 69, 76).

Chapter 5

Functional lasing microcapillaries for surface-specific sensing

A modified version of this chapter was published as Z. Zhang et al. "Functional lasing microcapillaries for surface-specific sensing," Optics Express **27** *(19), 26967 (2019).* DOI*:* `10.1364/oe.27.026967`*.*

5.1 Abstract

Lasing-based sensors have several advantages over fluorescent devices, specifically related to the high light intensity and narrow mode linewidth that can improve the speed and accuracy of the sensor performance. In this work, a microcapillary-based lasing sensor is demonstrated, in which the lasing wavelengths are sensitive to the surface binding of specific materials. In order to achieve this, we utilized lasing into the "star" and "triangle" modes of a conventional microcapillary and tracked the mode

positions after the deposition of a polyelectrolyte tri-layer and the subsequent amide binding of carboxy-functionalized polystyrene microspheres. While the lasing mode spectrum becomes increasingly complicated by the addition of the surface layers, careful mode selection can be used to monitor the layer-by-layer surface binding in a mechanically and optically robust device. For polystyrene microspheres, the detection limits were 9.75 nM based upon the lasing mode shift, which compares favorably with fluorescence-based devices. The methods presented in this work could readily be extended to other surface binding schemes and lasing wavelengths, showing that capillary microlasers could be used for many potential applications that capitalize on stable lasing-based detection methods.

5.2 Introduction

Whispering-gallery-mode (WGM) resonators such as microrings [56, 154–156], toroids [27–29], capillaries [31–33, 157], and spheres [25, 26, 158, 159] have been widely investigated for various sensing applications. WGM-based biosensing generally relies on one of two main approaches for measuring the mode structure. The first approach requires an external light source evanescently coupled into the cavity in order to track the resonance changes that occur when a particle (e.g., a virus, protein, or a representative nanoparticle) binds to the sensor surface. Evanescent coupling methods using phase-matched tapered fibers [160], waveguides [161], or prisms [17] are especially common. In these measurements, the cavity resonances are probed by a tunable laser and the modes appear as “dips” in the transmission spectrum. These methods are capable of measuring Q factors of 10^9 or higher [162], and can permit single-particle detection via modulation of the Q factor [163] or by mode splitting [164]. However, certain drawbacks have so far prevented the development of viable applications. These are mainly associated with expense (i.e., for a narrow-bandwidth tunable laser), device fragility, and difficult experimental setup and packaging. Recent work is aimed toward addressing some of these issues [165].

The second approach employs fluorescence spectroscopy to sample the WGMs. These unlabeled sensing schemes rely on the incorporation of the fluorescent material such as quantum dots [40, 166] or other chromophores [167] into the cavity architecture. The fluorescence is pumped via free-space excitation with a continuous-wave laser or light-emitting diode and the cavity resonances appear as modulations in the fluorescence spectrum. Measurement of WGMs via fluorescence obviates the need for expensive equipment such as narrow-bandwidth tunable lasers and does not require delicate or sensitive apparatus for coupling into the cavity modes. However, the light levels are extremely low in comparison to tunable laser setups and the emission must be further dispersed in a spectrometer. The Q factors also tend to be low, due to the inherently wide bandwidth of fluorophores at room temperature [168, 169]. Also, many fluorophores are susceptible to photobleaching, although this problem can be minimized by cross referencing schemes [170].

A WGM-based laser has several advantages for sensing applications, including a higher Q factor and more intense emission spectra as compared to fluorescence-based devices [45]. Microspherical lasers have been demonstrated for biosensing [61, 171] and, more recently, nonspecific lasing microcapillaries have been reported [**p2c12**]. These devices use laser-dye-containing layers as the gain medium. While a significant intensity enhancement and mode narrowing was observed, lasing instabilities seemed to preclude the development of biosensing applications [167]. In related work, thin-walled capillaries containing a laser dye solution in the channel have also been demonstrated for laser-based sensing applications [153].

Stable microcapillary lasing can be induced relatively easily in conventional thick-walled microcapillaries if the channel is filled with a gain medium [44]. The lasing modes are not the WGMs but are instead associated with reflections at both the inner and outer interfaces. These "geometric resonances" were recently demonstrated for non-specific refractive index sensing with sensitivities as high as 1000 nm/RIU [2]. The geometric modes allow the use of robust, thick-walled capillaries rather than the fragile capillaries commonly used for WGM-based sensing [172]. Capillaries have the additional advantage of being inherently fluidic and thus do not require external chambers or fluid handling systems. Thus, the object of this work is to demonstrate and evaluate the first example of specific surface sensing from the geometric modes of a microcapillary device.

5.3 Experimental methods

The devices were made from fused-silica microcapillaries ($n \approx 1.458$ at 600 nm [151]). Glass capillaries with 125-µm inner radius and 160-µm outer-radius were cut into ~5 cm lengths and the polyimide jacket was removed by ashing in a furnace at 923 K in flowing oxygen. Each capillary was connected to polytetrafluoroethylene tubing with Norland optical adhesive and affixed above a 20× objective lens. The scattered emission was measured from a direction perpendicular to the capillary axis.

The cavity geometric modes were excited using a Photon Technologies Inc. GL-302 dye laser operated at a wavelength of 500 nm, which was pumped by a GL-3300 N_2 laser. This setup produced pulses of approximately 1 ns with energies of ~200 µJ. A repetition rate of 3 Hz was used. The emission was collected with a 20× objective lens, sent through a 550 nm longpass filter, and it was then analyzed using an imaging spectrometer (30 seconds per exposure) (see Fig. 5.1) with the entrance slit perpendicular to the capillary axis. The fairly long collection times are required by the low repetition rate and resulting low average power (~0.6 mW) of our laser.

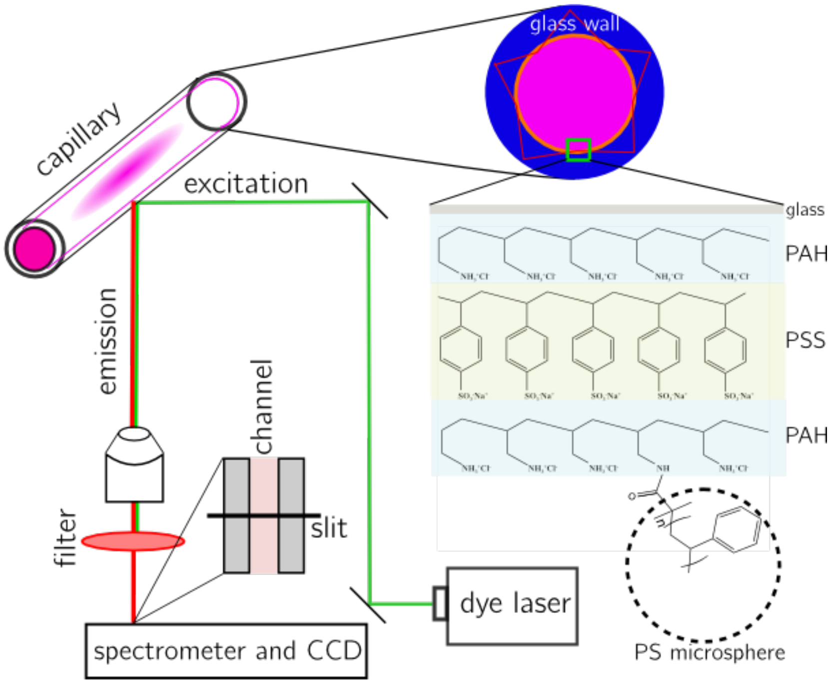

Figure 5.1 Diagram of the experimental setup. A representative star mode is illustrated in the capillary glass wall. The call-out on the right side illustrates the PE trilayer and a PS microsphere bound to the final PAH layer.

The capillary channel was then functionalized by using a polyelectrolyte layering method followed by the binding of carboxy-functionalized polystyrene (PS) microspheres:

1. The first step was to clean the surface by pumping 10 M NaOH solution through the channel of the capillary at a speed of 0.1 mL/min for 2 minutes, followed by a water rinse. This process leaves a slight negative charge on the channel wall [173, 174].

2. A solution of 1 mM rhodamine B (rhB) in water was then pumped into the capillary to establish the lasing baseline measurement (see Sec. 5.5). Note that lasing experiments are performed while the gain medium (the rhB-water solution) is being pumped through the chan-

nel. This was followed by a water rinse before moving to Step 3.

3. Next, a solution of 2 mg/mL polyallylamine hydrochloride (PAH) dissolved in a 2.5 M NaCl aqueous solution was pumped at a rate of 0.02 mL/min for 5 minutes followed by a water rinse. PAH has positively charged functional groups [175] that, therefore, should bind electrostatically to the clean capillary surface.
4. A solution of 2 mg/mL polystyrene sulfonate (PSS) in 2.5 M NaCl solution was pumped into the capillary at 0.02 mL/min for 5 minutes. The PSS has a negative surface charge and binds electrostatically to the PAH [40].
5. Repeat Step 3.
6. A solution of 1 mM rhB in water was pumped into the capillary and the lasing mode wavelength was then measured in order to observe the mode shifts after the trilayer formation. This was followed by a water rinse before moving to Step 7.
7. A solution of 50-nm-diameter PS microspheres (Polysciences; concentrations ranging from 0.05 mg/mL to 2 mg/mL), n-hydroxy-succinimide (NHS; 250 mM), and 1-ethyl-3-(3-dimethylamino-propyl)-carbodiimide (EDC; 250 mM) was then injected into the capillary for 30 minutes, followed by a water rinse.
8. Finally, Step 6 was repeated (rhB solution) in order to determine the lasing mode shifts after PS microsphere binding.

The presence of the PS microspheres was confirmed by helium ion microscopy. This method is similar to SEM, but it has an exceptionally large depth of focus [176], making it possible to obtain focused images "looking down" the axis of a capillary. The He ion beam was set to 30 kV and the imaging used a secondary electron detector. Charging was minimized by using a neutralizing electron gun in the sample chamber.

5.4 Basic theory and simulation

The star and triangle modes arise from reflections and refractions that occur at the inner and outer boundaries of the capillary (Fig. 5.2 **a**). A geometric description of these resonances was recently developed [2]; here, we further these ideas toward a multilayered structure (specifically, a capillary with a single effective channel coating). This coating approximates the PE trilayer described in the previous section, since each individual PE layer is extremely thin compared to the wavelength. The free spectral range (FSR) of the basic star and triangle modes can be written as [2]

$$\Delta f_{\text{star}} = \frac{c n_2 \sin\theta_3}{2N(n_1 n_2 r_1 \sin\psi \sin\theta_3 + r_1 n_2^2 \sin\alpha + r_3 n_3^2 \sin\phi)} \tag{5.1}$$

and

$$\Delta f_{\text{triangle}} = \frac{c n_2 \sin\theta_3}{2(v r_3 n_3^2 \sin\phi - u r_1 n_1 n_2 \sin\psi \sin\theta_3 - u r_1 n_2^2 \sin\alpha)}, \tag{5.2}$$

where the variable ψ is the half-angle subtended by the points of the incidence for the ray that refracts into the PS microsphere film and return to surface 1 (see Fig. 5.1 **a**), α is the half-angle subtended by the points of the incidence for the ray that refracts into the PE layer and returns to surface 2, and ϕ is the half-angle subtended by the path that refracts through the glass wall and return to the surface 3 (Fig. 5.2 **b**). θ_3 is the incident angle of the ray travelling from the PE layer to the glass wall, and u and v are integers describing the triangle modes [2], N is the number of points on the star, and the refractive indices for the inner region, the layer, and the capillary wall are n_1, n_2, and n_3, and r_1, r_2 and r_3 are the radii associated with the layered capillary (Fig. 5.2 **a**).

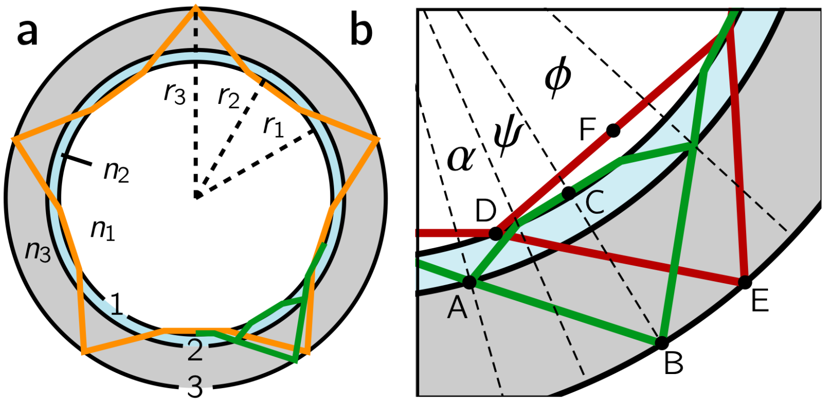

Figure 5.2 Diagram illustrating star mode and triangle modes in a layered capillary coating PE layer. **a** An example star mode (orange; $N = 5$) and a triangle mode superimposed in green. **b** Ray paths illustrating Type 1 (red) and Type 2 (green) triangle modes.

For typical capillary sizes (e.g., the 160 µm outer and 125 µm inner diameters used in the experiment to follow and a 60 nm thick the PE multilayer), the FSR of the star and triangle modes is 0.228 and 4.86 THz, respectively (or 0.27 and 5.8 nm at a wavelength of ~600 nm). The resonant wavelengths are given by:

$$\lambda_{\text{star}} = \frac{2N}{m}\left(n_1 r_1 \sin\psi + \frac{n_2 r_1 \sin\alpha}{\sin\theta_3} + \frac{r_3 n_3^2 \sin\phi}{n_2 \sin\theta_3}\right) \tag{5.3}$$

and

$$\lambda_{\text{triangle}} = \frac{2}{m}\left(v\frac{r_3 n_3^2 \sin\phi}{n_2 \sin\theta_3} - u r_1 n_1 \sin\psi - u\frac{r_1 n_2 \sin\alpha}{\sin\theta_3}\right), \tag{5.4}$$

where m is the mode number. To find the resonant wavelengths, using the laws of reflection and refraction these angles can be related by

$$\theta_3 = \arcsin\left(\frac{n_1 r_1}{n_2 r_2}\cos\psi\right), \tag{5.5}$$

$$\alpha = \arcsin\left(\frac{n_1}{n_2}\cos\psi\right) - \theta_3, \tag{5.6}$$

and

$$\phi = \arcsin\left(\frac{n_2}{n_3}\sin\theta_3\right) - \arcsin\left(\frac{r_2 n_2}{r_3 n_3}\sin\theta_3\right). \tag{5.7}$$

The incident angle ψ for the star and triangle modes can be obtained by the constraints that $N(\psi + \alpha + \phi) = \pi$ and $u(\psi + \alpha) = v\phi$, respectively.

Adding an effective layer (i.e., a single layer meant to approximate the channel coatings) to the channel wall increases the number of reflections and possible paths for the triangle modes. Since there is now one more boundary, there are at least two "sub-modes" that can form: Type 1, in which the path difference is given by $\Delta\mathrm{OPL}_1 = 2(DE\text{˘}DF)$ and Type 2 which has a path difference $\Delta\mathrm{OPL}_2 = 2(AB\text{˘}AC)$ (Fig. 5.2 **b**). These path differences shift in an opposite sense as the film thickness, t, increases. Thus, a careful selection of the specific lasing modes permits an observation of either a redshift or a blueshift upon the binding of a surface layer.

Considering the ray paths contributing to the Type 2 triangle modes, the path difference can be written as

$$\Delta\mathrm{OPL}_{\mathrm{triangle-2}} = 2\left(\frac{r_3 n_3^2 \sin\phi}{n_2 \sin\theta_3} - r_1 n_1 \sin\psi - \frac{r_1 n_2 \sin\alpha}{\sin\theta_3}\right). \tag{5.8}$$

Setting $\Delta\mathrm{OPL}_{\mathrm{triangle-2}} = m\lambda$, letting $m = 100$, establishing the condition for a triangle mode that $\psi + \alpha = 0$, and applying the laws of reflection and refraction, the resonant wavelength is 617.06 nm for a film of optical thickness 88.8 nm (this was selected to be relevant to the experimental results described below). In contrast, in the absence of the film this same mode number corresponded to a wavelength of 617.49 nm, showing that the Type 2 triangle mode is blueshifted owing to the presence of a film.

For the star modes, the film increases the round-trip path length, leading to a redshift. The magnitude of the redshift is expected to be small, since the mode order corresponding to a similar wavelength would be much larger than for a triangle mode. The optical path increase $\Delta\mathrm{OPL}_{\mathrm{star}}$ in a layered capillary is

$$\Delta\mathrm{OPL}_{\mathrm{star}} = 2N\left(n_1 r_1 \sin\psi + \frac{n_2 r_1 \sin\alpha}{\sin\theta_3} + \frac{r_3 n_3^2 \sin\phi}{n_2 \sin\theta_3}\right). \tag{5.9}$$

Based on the condition for the star mode that $N(\psi + \alpha + \psi) = \pi$, setting $\Delta\mathrm{OPL}_{\mathrm{star}} = m\lambda$, and letting $m = 2165$, the resonant wavelength is 617.27 nm for the film of optical thickness 88.8 nm. By comparison, in the absence of the film this same mode number corresponded to a wavelength of 617.18 nm, showing that the star mode is indeed redshifted due to the presence of the film.

The ray picture derived above gives the basic character of the geometric modes of a layered cylindrical structure. In order to visualize the mode field, the device was modeled with 2D finite-difference-time-domain (FDTD) simulations using Lumerical FDTD Solutions. The cell length was 100 nm and perfectly-matched boundaries were used. In order to match the experiment, the structure had to be much larger than the simulation cell size, so each simulation required approximately 1 week on a 2.6 GHz computer with 8 cores and 72 GB of memory. The exciter was a dipole placed 2 microns from the inner wall and the simulation time was 105 fs. The layer is too thin to be accurately simulated in a reasonable timeframe, but the layer is not crucial for simply visualizing the resonant mode fields.

The resulting spectrum shows the star and triangle modes (Fig. 5.3 **a**). A CW simulation was performed on a single, narrow mode at 610.97 nm (one of the “black dotted” modes in Fig. 5.3 **a**). The resulting spatial intensity distribution was clearly consistent with a star mode (Fig. 5.3 **b**) that circles three times before returning to its starting point. While the simple geometric calculation assumes a one-cycle closed path, a large number of related modes can clearly also exist and their strength depends on the position and orientation of the excitation dipole. By changing the refractive index of the inner medium, the sensitivity of both mode types were determined. The sensitivity was 67 nm/RIU (refractive index unit) for the star mode and 863 nm/RIU for the triangle mode in Fig. 5.3. These values are consistent with those calculated from the geometric equations for the two mode classes.

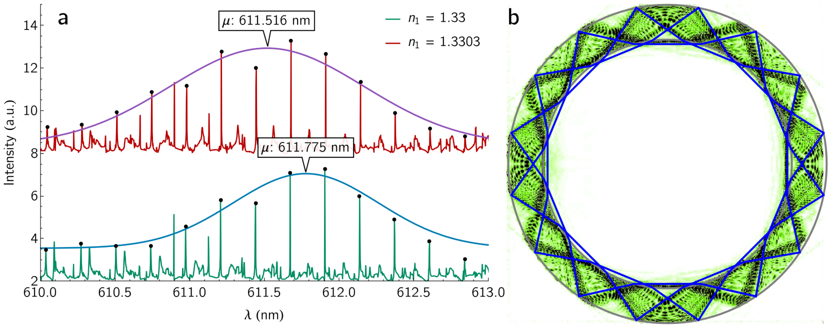

Figure 5.3 **a** Simulated FDTD spectra for a capillary of radii r = 125 and R = 160 μm for two different refractive indices in the channel (1.3300 vs. 1.3303). The star modes are marked by the black dots, and the triangle mode envelopes are represented by the Gaussian fits as shown by the blue and purple lines and described by the mean value, μ. **b** A star mode resonance at a wavelength of 610.97 nm. The blue lines represent the ray diagrams shown in Fig. 5.2, while the corresponding field intensities are shown on a scale from light green to black.

5.5 Results and discussion

The FDTD results described above clearly identified the star and triangle modes, producing results that were consistent with the theoretical sensitivity of the various mode types. The geometric analysis was extended to account for the presence of a surface layer on the channel wall. The star modes are expected to redshift while the triangle modes will subdivide into two types whose resonant wavelengths shift in opposite directions.

The lasing mode spectrum for a bare capillary with an rhB solution (Experimental Step 2; Fig. 5.4) consists of a set of narrowly-spaced modes separated by ~0.28 nm underneath a more widely-spaced envelope that, together, formed groups of resonances similar to those reported previously [2]. The lasing threshold was ~6.5 µJ/mm^2. The FSR of the narrowly-spaced modes agreed well with the star modes of Eq. 5.1 (0.28 nm), but for the triangle modes the experimental FSR was ~2.5 nm, which is about half the expected value for a single mode family with $u = v = 1$ in Eq. 5.2. This suggests that we observe multiple "orders" of triangle modes with different numbers of reflections inside the capillary wall (i.e., different u and v parameters), as well as the presence of Type 1 and Type 2 triangle modes.

The mode spectrum shifted after deposition of the polyelectrolyte trilayer and again after the PS microsphere binding (Fig. 5.4; Experimental Steps 6 and 8). Since the spectrum consists of a complicated set of overlapping mode families that are expected to shift in different directions, visually tracking the shifts is difficult. The shift of the envelope function (i.e., one the triangle modes) can, however, be visualized by taking the peaks of the underlying star modes and fitting them to a Gaussian function (Fig. 5.5), in which a shift of the envelope after each step becomes more apparent. The mode shown is therefore most likely a blueshifting triangle mode of Type 2.

In order to create a sensorgram of the lasing mode response, Fourier shift theorem [70] was used to track the wavelength shifts. This method measures the phase shift of selected Fourier components, weighted proportionally to their power. For a theoretical mode spacing of 0.27 and 5.8 nm for the star and triangle modes, the corresponding Fourier components in the spectrum are expected to be near 160 and 15, respectively. We therefore took these Fourier components and tracked their phase shifts over a multilayer deposition sequence (Fig. 5.6). Here, we first examine the PE

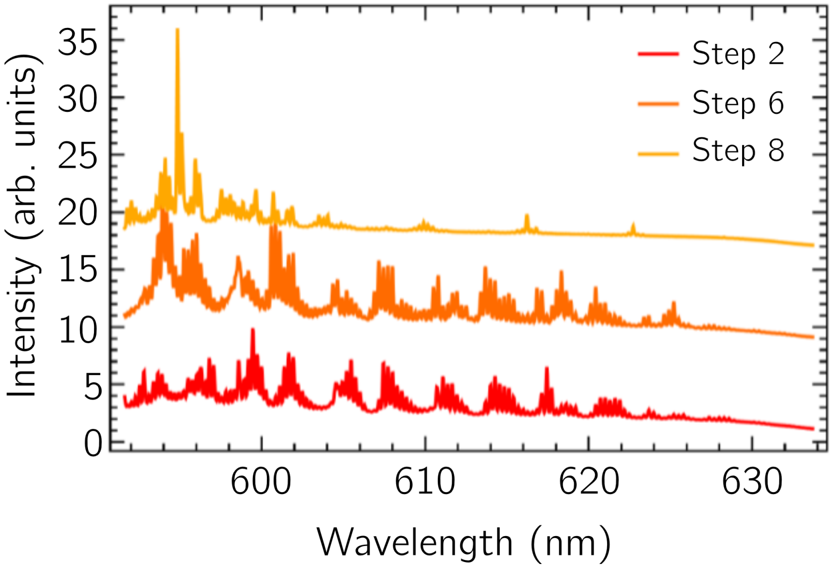

Figure 5.4 The lasing spectra of the initial blank capillary (Experimental Step 2), after PE trilayer deposition (Step 6) and after PS microsphere binding on the PE trilayer (Step 8).

layer deposition by building three PAH-PSS bilayers – that is, Steps 1-2, (3-4-6), (3-4-6), (3-4-6), with the sensorgram measurements done at Step 2 and Steps 6. A well-defined sensorgram results, in which the star modes slightly redshift as predicted by the theory in the previous section, and the triangle modes showed a large blueshift consistent with the presence of Type 2 modes. Type 1 triangle modes were also present in the spectrum and could be identified by selecting slightly different Fourier components which yielded the expected redshifts.

The layer thickness can be extrapolated by comparing the magnitude of the mode shift to the geometric theory in the previous section. The refractive indices of the PE bilayers are not well known but have been estimated to be around 1.5 [177, 178]. Using this refractive index, a single bilayer needs to be ~20 nm thick to generate the observed shift. This is a reasonable value given the high saline concentration used to form the PE layers [179].

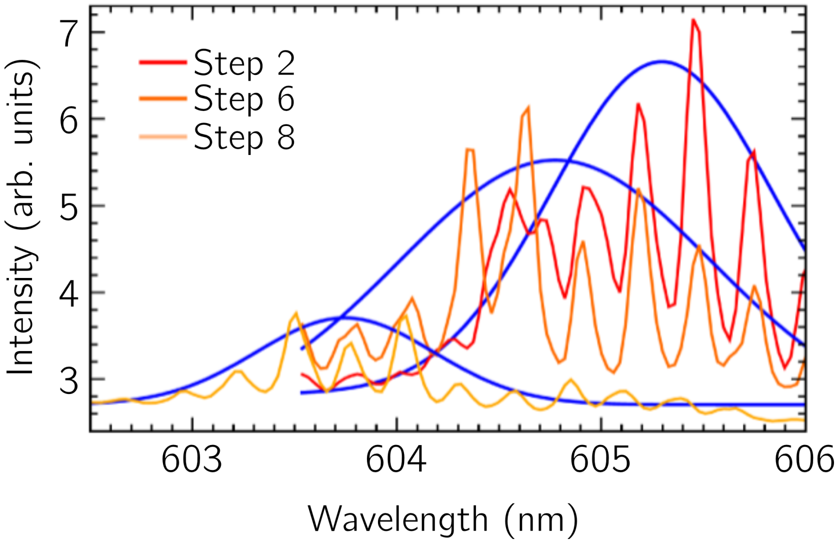

Figure 5.5 Zoom-in of part of the emission spectrum after the synthesis steps shown in the legend. The triangle modes (blue lines) are found by Gaussian fits of the star mode maxima.

We next ran a full sensing experiment following all the steps in the experimental section, monitoring the star modes and Type 2 triangle modes in the sensorgram (Fig. 5.7 **a**). The measurements were performed in Steps 2, 6, and 8. Once again, there is a stable sensorgram with clear shifts in the expected directions. For a PE trilayer deposition, the star modes shifted by 34 pm, and a further 81 pm subsequent to the microsphere solution being pumped into the channel (note that all measurements – Steps 2, 6, and 8 – are done with only the rhB solution). For the triangle modes, we observed a blueshift of −0.47 and a further −0.68 nm in Steps 6 and 8, respectively.

Binding of the microspheres produced well-defined mode shifts in the sensorgram (Fig. 5.7 **a**). While the randomly-distributed microspheres might be expected to have a complicated effect by causing scattering losses and changing the ray paths in arbitrary directions, the sensorgram nevertheless showed clear, stable mode shifts after microsphere binding. Qualitatively, the overall effect of the microspheres would be to increase the

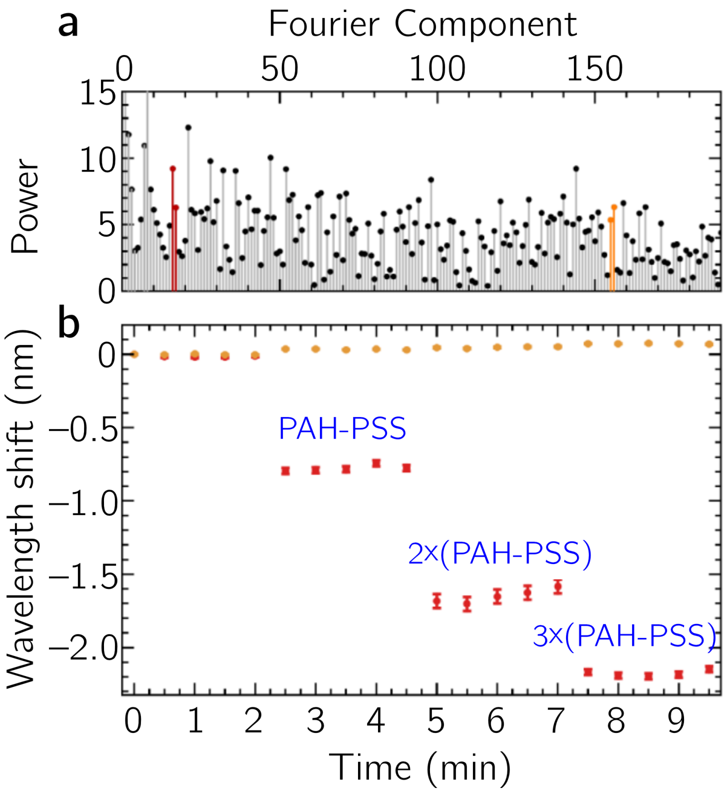

Figure 5.6 **a** Discrete Fourier transform of the spectrum of a capillary with 125-μm inner radius and 160-μm outer radius with PAH-PSS bilayers. The red and orange Fourier components indicate the phases used to calculate the wavelength shift of the triangle modes and star modes, respectively. **b** Corresponding sensorgram for 1-bilayer, 2-bilayers and 3-bilayers of PE functionalization.

path length of the star modes, since the rays are more likely to travel through high-index ($n = 1.59$) polystyrene than otherwise. A similar qualitative argument implies a further blueshift for the Type 2 triangle modes, as observed experimentally.

A blank run was also conducted to see if the microspheres had bound specifically to the functionalized capillary surface. The same steps were repeated as before, except the PE functionalization was left out (Steps 3-5). A small shift was still observed (approx. 5 pm for star modes and −80 pm for the Type 2 triangle modes), suggesting that there is ~8% nonspecific binding, as estimated from the magnitude of the mode shifts. The HIM micrographs showed that an ~22% microsphere surface coverage on the functionalized capillaries, whereas only a few microspheres could be found on the blank (see Fig. 5.7 (insets)).

In order to determine the detection limits for these capillary microlaser sensors, the experiments were repeated with microsphere concentrations ranging from 0.05 to 2 mg/mL (corresponding to a molar concentration range of 1.2 to 48.3 nM). In every case, the capillaries were first PE functionalized (Step 5) the lasing modes were measured (Step 6), the microspheres were pumped through the capillary for 30 minutes (Step 7), and then the mode positions were measured again (Step 8). The functionalization steps were the same in every case and resulted in similar lasing mode shifts for both the star and triangle modes (Fig. 5.8 **a**).

The shifts after microsphere binding varied monotonically with the concentration. The sensitivity was estimated by a linear fit of the wavelength shift as a function of the microsphere concentration (Fig. 5.5 **b**), yielding a sensitivity of $S = 15$ pm/nM for 50-nm-diameter PS microspheres. To obtain the detection limit (DL), the wavelength resolution (R_e = 15 pm) was defined as 3 times the largest standard deviation of shifts observed under steady-state conditions in Fig. 5.8 **a**. This yielded a detection limit of DL = R_e/S = 9.75 nM or 0.41 µg/mL for these lasing capillary sensors with 50-nm PS microspheres. While these values are technically only comparable for the same analytes, the DL is similar to those for capillary-based WGMs in the literature [40] while providing a more robust sensor with much easier synthesis. This number could likely be increased, for example, by combining data from mode shifts of opposite sense, obtaining a better signal-to-noise ratio by using a higher average power of the pump laser (which was ~0.6 mW in this work), and by minimization of mechanical vibration via better device packaging, as has been recently shown for delicate WGM-type sensors [165].

Additionally, lasing intensity or threshold measurements can be even more sensitive than the lasing model shift measurements reported here [180]. However, intensity-based measurements are sensitive to photobleaching or other instabilities in the lasing gain medium as well as fluctuations in the excitation, and can require a laborious or time-consuming data collection routines.

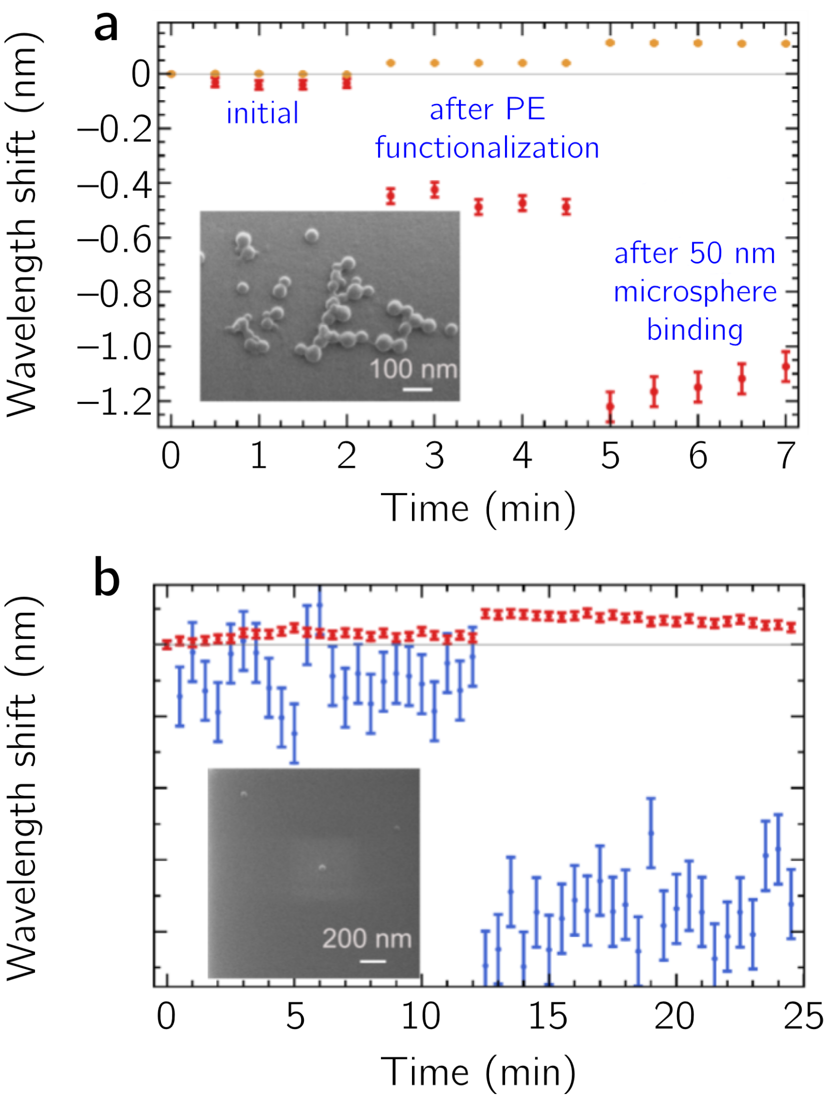

Figure 5.7 **a** Sensorgram showing the Type-2 triangle (red points) and star (orange points) mode shifts after the PE bilayer and subsequent microsphere binding. The inset shows a representative HIM image of a group of microspheres bound to the surface. The overall surface coverage was 22%. **b** Sensorgram for a "blank" run in which the PE trilayer was not deposited (red points indicate star and blue points indicate triangle modes). A small shift was observed, suggesting that some microspheres can bind non-specifically to the capillary wall. The inset shows a representative HIM image, in which a few microspheres can indeed be found in the capillary channel. The error bars represent the standard deviation of the data in each section.

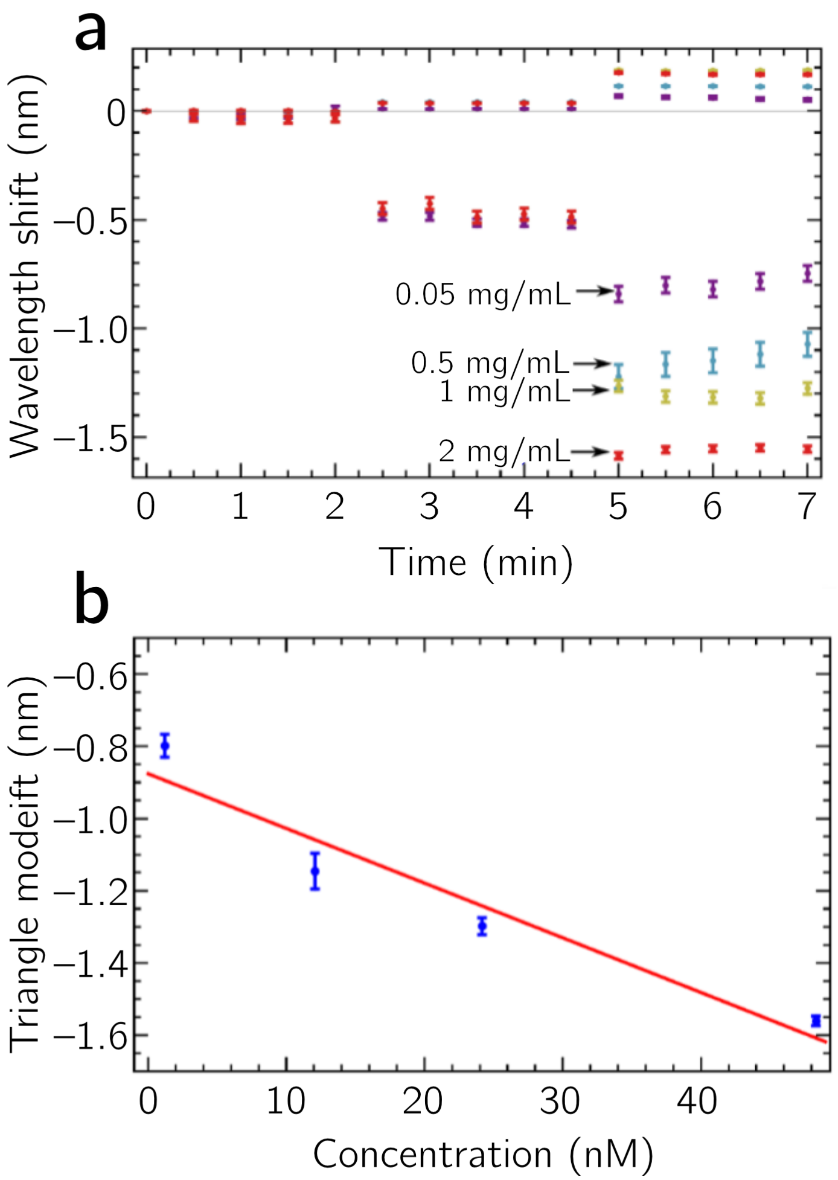

Figure 5.8 **a** Sensorgrams showing the mode shifts after exposure to the PE tri-layer and a subsequent PS microsphere binding step, using 0.05 mg/mL (purple), 0.5 mg/mL (blue), 1 mg/mL (yellow) and 2 mg/mL (red) microsphere solutions. **b** Plot of the magnitude of the total Type-2 triangle mode shifts after PS binding, as a function of the concentrations of 50 nm PS microsphere solution. The slope yields a sensitivity of 15 pm/nM. The error bars in **a** and **b** represent the standard deviation of the data for the four different concentrations.

5.6 Conclusions

This work developed the concept of the geometric capillary resonances for specific surface sensing. We first developed the theory for the geometric modes in a layered capillary, and showed that the mode structure becomes significantly more complicated due to the formation of new ray paths in the capillary walls. We then built and tested a lasing device in which polyelectrolyte multilayers were deposited on the capillary channel, followed by the amide bonding of carboxy-functionalized PS microspheres as a proof-of-concept system. Good sensorgrams could be obtained by a Fourier analysis of the lasing mode shifts. The magnitude and direction of the shifts were consistent with the theoretical analysis. These resonances offer an intriguing alternative to fluorescent WGM-based sensing schemes with several specific advantages. Since the resonances are defined by lasing modes, the emission intensity is much stronger than for WGMs, and since the lasing medium is continually refreshed, the emission is stable indefinitely (i.e., no bleaching was observed). The bulk sensitivities are higher than for conventional WGMs and they show good response to surface binding, with the shifts of the triangle modes on the order of 0.7 nm after 22% sphere surface coverage.

5.7 Acknowledgements

Natural Sciences and Engineering Research Council of Canada (463990-2015); National Natural Science Foundation of China (11404052, 11474048, 11874102); Sichuan Province Science and Technology Support Program (2019YJ0187); Graduate School, Technische Universität München; Future Energy Systems.

5.8 References

[2] W. Morrish et al. "Geometric Resonances for High-Sensitivity Microfluidic Lasing Sensors," *Physical Review Applied* **10** (5), 051001 (Nov. 2018). DOI: `10.1103/PhysRevApplied.10.051001` (pp. iv, 58, 77, 80, 85).

[3] Z. Zhang et al. "Functional lasing microcapillaries for surface-specific sensing," *Optics Express* **27** (19), 26967 (2019). DOI: `10.1364/oe.27.026967` (pp. v, 74).

[17] M. D. Baaske, M. R. Foreman, and F. Vollmer. "Single-molecule nucleic acid interactions monitored on a label-free microcavity biosensor platform," *Nature Nanotechnology* **9**. 933 (2014). DOI: `10.1038/nnano.2014.180` (pp. 2, 59, 75).

[25] H. T. Beier, G. L. Cote, and K. E. Meissner. "Whispering Gallery Mode Biosensors Consisting of Quantum Dot-Embedded Microspheres," *Annals of Biomedical Engineering* **37** (10), 1974–1983 (2009). DOI: `10.1007/s10439-009-9713-2` (pp. 2, 75).

[26] Y. Zhi, T. Thiessen, and A. Meldrum. "Silicon quantum dot coated microspheres for microfluidic refractive index sensing," *Journal of the Optical Society of America B-Optical Physics* **30** (1), 51–56 (2013). DOI: `10.1364/josab.30.000051` (pp. 2, 34, 75).

[27] H. Fan et al. "Confined whispering-gallery mode in silica double-toroid microcavities for optical sensing and trapping," *Optics Communications* **434**. 97–103 (2019). DOI: `10.1016/j.optcom.2018.10.055` (pp. 2, 75).

[28] J. Su, A. F. G. Goldberg, and B. M. Stoltz. "Label-free detection of single nanoparticles and biological molecules using microtoroid optical resonators," *Light-Science & Applications* **5**. (2016). DOI: `10.1038/lsa.2016.1` (pp. 2, 75).

[29] E. Ozgur et al. "Label-Free Biosensing with High Selectivity in Complex Media using Microtoroidal Optical Resonators," *Scientific Reports* **5**. (2015). DOI: `10.1038/srep13173` (pp. 2, 75).

[31] V. Zamora et al. "Refractometric sensor based on whispering-gallery modes of thin capillaries," *Optics Express* **15** (19), 12011–12016 (2007). DOI: `10.1364/oe.15.012011` (pp. 2, 75).

[32] I. M. White, H. Oveys, and X. Fan. "Liquid-core optical ring-resonator sensors," *Optics Letters* **31** (9), 1319–1321 (2006). DOI: `10.1364/OL.31.001319` (pp. 2, 9, 75).

[33] C. P. K. Manchee et al. "Refractometric sensing with fluorescent-core microcapillaries," *Optics Express* **19** (22), 21540–21551 (2011). DOI: `10.1364/OE.19.021540` (pp. 2, 34, 59, 75).

[40] S. Lane et al. "Protein biosensing with fluorescent microcapillaries," *Optics Express* **23** (3), 2577–2590 (Feb. 2015). DOI: `10.1364/OE.23.002577` (pp. 3, 9, 10, 59, 76, 79, 89).

[44] H.-J. Moon and D.-Y. Kang. "Strongly enhanced mode selection in a thin dielectric-coated layered microcavity laser," *Optics Letters* **32** (11), 1554–1556 (2007). DOI: `10.1364/OL.32.001554` (pp. 7, 63, 66, 77).

[45] T. Reynolds et al. "Fluorescent and lasing whispering gallery mode microresonators for sensing applications," *Laser & Photonics Reviews* **11** (2), (2017). DOI: `10.1002/lpor.201600265` (pp. 7, 76).

[56] S. M. Grist et al. "Silicon photonic micro-disk resonators for label-free biosensing," *Optics Express* **21** (7), 7994–8006 (2013). DOI: `10.1364/oe.21.007994` (pp. 9, 75).

[61] A. Francois et al. "Polymer based whispering gallery mode laser for biosensing applications," *Applied Physics Letters* **106** (3), (2015). DOI: `10.1063/1.4905931` (pp. 9, 34, 76).

[70] J. W. Silverstone et al. "Ultimate resolution for refractometric sensing with whispering gallery mode microcavities," *Optics Express* **20** (8), 8284–8295 (Apr. 2012). DOI: `10.1364/OE.20.008284` (pp. 10, 29, 41, 42, 47, 65, 85).

[151] I. H. Malitson. "Interspecimen Comparison of the Refractive Index of Fused Silica*,†," *Journal of the Optical Society of America* **55** (10), 1205–1209 (1965). DOI: `10.1364/JOSA.55.001205` (pp. 65, 77).

[153] Y.-C. Chen, Q. Chen, and X. Fan. "Lasing in blood," *Optica* **3** (8), 809 (2016). DOI: `10.1364/optica.3.000809` (pp. 69, 76).

[154] G. Mi et al. "Silicon microring refractometric sensor for atmospheric CO2 gas monitoring," *Optics Express* **24** (2), 1773–1780 (2016). DOI: `10.1364/oe.24.001773` (p. 75).

[155] A. L. Washburn et al. "Label-free, multiplexed biomolecular analysis using arrays of silicon photonic microring resonators," *Eurosensors Xxv*. Ed. by G. Kaltsas and C. Tsamis. Vol. 25. Procedia Engineering. 2011. DOI: `10.1016/j.proeng.2011.12.016` (p. 75).

[156] D. X. Xu et al. "Folded cavity SOI microring sensors for high sensitivity and real time measurement of biomolecular binding," *Optics Express* **16** (19), 15137–15148 (2008). DOI: `10.1364/oe.16.015137` (p. 75).

[157] H. Zhu et al. "Analysis of biomolecule detection with optofluidic ring resonator sensors," *Optics Express* **15** (15), 9139–9146 (2007). DOI: `10.1364/oe.15.009139` (p. 75).

[158] A. Weller et al. "Whispering gallery mode biosensors in the low-Q limit," *Applied Physics B-Lasers and Optics* **90** (3-4), 561–567 (2008). DOI: `10.1007/s00340-007-2893-2` (p. 75).

[159] T. Reynolds et al. "Dynamic Self-Referencing Approach to Whispering Gallery Mode Biosensing and Its Application to Measurement within Undiluted Serum," *Analytical Chemistry* **88** (7), 4036–4040 (2016). DOI: `10.1021/acs.analchem.6b00365` (p. 75).

[160] Y. Wang et al. "Tapered optical fiber waveguide coupling to whispering gallery modes of liquid crystal microdroplet for thermal sensing application," *Optics Express* **25** (2), 918–926 (2017). DOI: `10.1364/oe.25.000918` (p. 75).

[161] T. Le et al. "Polymer optical waveguide vertically coupled to high-Q whispering gallery resonators," *Ieee Photonics Technology Letters* **18** (5-8), 859–861 (2006). DOI: `10.1109/lpt.2006.871815` (p. 75).

[162] A. Rasoloniaina et al. "Controling the coupling properties of active ultrahigh-Q WGM microcavities from undercoupling to selective amplification," *Scientific Reports* **4**. (2014). DOI: `10.1038/srep04023` (p. 75).

[163] L. Shao et al. "Detection of Single Nanoparticles and Lentiviruses Using Microcavity Resonance Broadening," *Advanced Materials* **25** (39), 5616–5620 (Oct. 2013). DOI: `10.1002/adma201302572` (p. 75).

[164] L. He et al. "Ultrasensitive detection of mode splitting in active optical microcavities," *Physical Review A* **82** (5), (2010). DOI: `10.1103/PhysRevA.82.053810` (p. 75).

[165] X. Xu et al. "Phone-sized whispering-gallery microresonator sensing system," *Optics Express* **24** (23), 25905–25910 (2016). DOI: `10.1364/oe.24.025905` (pp. 76, 90).

[166] G. Decher. "Fuzzy nanoassemblies: Toward layered polymeric multicomposites," *Science* **277** (5330), 1232–1237 (1997). DOI: `10.1126/science.277.5330.1232` (p. 76).

[167] K. J. Rowland et al. "Fluorescent polymer coated capillaries as optofluidic refractometric sensors," *Optics Express* **21** (9), 11492–11505 (2013). DOI: 10.1364/oe.21.011492 (p. 76).

[168] A. Meldrum, P. Bianucci, and F. Marsiglio. "Modification of ensemble emission rates and luminescence spectra for inhomogeneously broadened distributions of quantum dots coupled to optical microcavities," *Optics Express* **18** (10), 10230–10246 (2010). DOI: 10.1364/oe.18.010230 (p. 76).

[169] Y. Zhi, J. Valenta, and A. Meldrum. "Structure of whispering gallery mode spectrum of microspheres coated with fluorescent silicon quantum dots," *Journal of the Optical Society of America B-Optical Physics* **30** (11), 3079–3085 (2013). DOI: 10.1364/josab.30.003079 (p. 76).

[170] S. F. Wondimu et al. "Robust label-free biosensing using microdisk laser arrays with on-chip references," *Optics Express* **26** (3), 3161–3173 (2018). DOI: 10.1364/oe.26.003161 (p. 76).

[171] A. Francois and M. Himmelhaus. "Whispering gallery mode biosensor operated in the stimulated emission regime," *Applied Physics Letters* **94** (3), (2009). DOI: 10.1063/1.3059573 (p. 76).

[172] V. Zamora et al. "Cylindrical optical microcavities: Basic properties and sensor applications," *Photonics and Nanostructures-Fundamentals and Applications* **9** (2), 149–158 (2011). DOI: 10.1016/j.photonics.2010.09.007 (p. 77).

[173] S. A. Greenberg. "The depolymerization of silica in sodium hydroxide solutions," *Journal of Physical Chemistry* **61** (7), 960–965 (1957). DOI: 10.1021/j150553a027 (p. 78).

[174] S. H. Behrens and D. G. Grier. "The charge of glass and silica surfaces," *Journal of Chemical Physics* **115** (14), 6716–6721 (2001). DOI: 10.1063/1.1404988 (p. 78).

[175] G. Decher and J. Schmitt. "Fine-Tuning of the film thickness of ultrathin multilayer films composed of consecutively alternating layers of anionic and cationic polyelectrolytes," *Trends in Colloid and Interface Science VI*. Ed. by C. Helm, M. Lösche, and H. Möhwald. Darmstadt: Steinkopff, 1992, 160–164 (p. 79).

[176] "Helium Ion Microscopy," *Helium Ion Microscopy*. Ed. by G. Hlawacek and A. Golzhauser. Nanoscience and Technology. 2016, 1–526. DOI: `10.1007/978-3-319-41990-9` (p. 79).

[177] G. Ladam et al. "Protein interactions with polyelectrolyte multilayers: Interactions between human serum albumin and polystyrene sulfonate/polyallylamine multilayers," *Biomacromolecules* **1** (4), 674–687 (2000). DOI: `10.1021/bm005572q` (p. 86).

[178] C. L. Schauer et al. "Color changes in chitosan and poly(allyl amine) films upon metal binding," *Thin Solid Films* **434** (1-2), 250–257 (2003). DOI: `10.1016/s0040-6090(03)00055-5` (p. 86).

[179] Z. Feldötö, I. Varga, and E. Blomberg. "Influence of salt and rinsing protocol on the structure of PAH/PSS polyelectrolyte multilayers," *Langmuir* **26** (22), 17048–17057 (2010). DOI: `10.1021/la102351f` (p. 86).

[180] A. François, H. Schwefel, and T. M. Monro. "Using the lasing threshold in whispering gallery mode resonators for refractive index sensing," *Laser Resonators, Microresonators, and Beam Control XX*. Ed. by A. V. Kudryashov, A. H. Paxton, and V. S. Ilchenko. Vol. 10518. International Society for Optics and Photonics. SPIE, 2018, 89–93. DOI: `10.1117/12.2288871` (p. 90).

Chapter 6

Integrating sphere laser absorption spectroscopy

6.1 Introduction

Greenhouse gases such as methane and carbon dioxide are believed to be major contributors to climate change [181–183]. Thus, detecting the presence and concentration of these gases—in the atmosphere and at their sources such as pipelines and power generation facilities—has become a growing area of research interest. As with many other applications, such as those already discussed in this thesis, optical methods are well-suited for detecting and quantifying these gases. Optics provides opportunities for remote sensing [89], offers a high-sensitivity [90, 184], and many optical sensing devices have compact footprints [185–187].

As detailed in Section 1.3, laser absorption spectroscopy (LAS) involves tuning a laser to one of the absorption features of a gas. Methane and carbon dioxide both have absorption features in the near-infrared (NIR) region, taken here to mean wavelengths from 0.7 µm to 3 µm, created by rovibrational transitions in the molecules, as discussed from a theoretical perspective in Chapter 1. The basic premise of LAS is that greater numbers of molecules absorb more of the laser light, resulting in reduced intensity at the detector. However, there are some important variations on this basic scheme.

Tunable-diode laser absorption spectroscopy (TDLAS) involves scanning the wavelength of a diode laser over an absorption peak [90, 184–187]. This is done by modulating the input current to the laser with a ramp waveform. This has the effect of changing both the wavelength and intensity of the laser emission. At the edges of the scan, outside the absorption peak, there will be no absorption from the gas and all of the laser intensity will be transmitted to the photodetector. These absorption-free portions of the scan allow for the overall spectrum to be corrected for the ramping intensity of the laser and the resultant absorption can be extracted.

A further modification to this scheme is wavelength modulation spectroscopy (WMS) [188–192]. The ramp waveform is supplemented by a sinusoidal waveform at a much higher frequency, causing the laser wavelength and intensity to rapidly oscillate on top of the slower ramp signal. Lock-in detection methods can then be applied to extract the second harmonic of the signal, greatly reducing noise as well as offsets caused by the ramp signal. This extracted signal can then either be integrated and correlated to the gas concentration, or a fitting routine can be used to match the concentration. Such a fitting routine involves modelling the absorption spectrum as a function of concentration, simulating the intensity of the modulated laser after it passes through the gas, and simulating the lock-in detection process. The initial concentration is then adjusted until the resultant simulation matches the experimental spectrum. This method can even be used to extract the temperature and pressure of the gas by adding them as modelling parameters.

Both TDLAS and WMS are often performed in multipass cells (Section

1.3.2). While substantial path lengths can be achieved in these cells, they require precise alignment between the laser, the mirrors, and the detector. They also tend to be quite expensive (on the order of $5000USD from ThorLabs). In contrast to multipass cells, integrating spheres have highly reflective internal coatings designed to reflect all the emitted light from a source inside the sphere. When laser light is injected into the sphere, reflections from the diffusely reflecting walls can substantially increase the average path length of the laser compared to a direct path between the laser and detector. Such a device requires no special alignment and the sphere itself provides a chamber to contain sampled gas for analysis. In this chapter, I describe my work to develop an integrating sphere LAS device using TDLAS and WMS for sensing methane and carbon dioxide.

6.2 Theory

The path length of the laser through the gas is a critical factor affecting the sensitivity of an LAS device; longer path lengths mean greater absorption of the laser light by the gas. In order to model the flux of light passing through a multipass cell in the presence of an absorbing gas, we can use the Beer-Lambert law, $\Phi = \Phi_0 \exp(-\alpha c l)$, where Φ is the transmitted flux, Φ_0 is the input laser flux, α is the absorption coefficient of the targeted absorption feature, c is the mole fraction, and l is the path length.

In an integrating sphere many, paths are possible as rays trace a random path through the sphere from emitter to detector. The average path length through the sphere L_{eff} is given as

$$L_{\text{eff}} = \frac{2}{3} M D, \tag{6.1}$$

where D is the diameter of the sphere, and M is called the sphere multiplier. The factor of $2D/3$ represents the average distance across the sphere

[99]. The sphere multiplier represents the average number of reflections a ray will experience and is given by

$$M = \frac{\rho}{1 - \rho(1 - a(\nu))(1 - f)} \,, \tag{6.2}$$

where ρ is the reflectance of the sphere's surface, f is the fraction of the sphere's surface covered by ports or other non-reflecting elements, and $a(\nu)$ is the attenuation for a typical pass through the sphere [193]. For measurements of methane and carbon dioxide in the atmosphere, this attenuation is negligible.

The most common atmospheric constituents include N_2, O_2, water vapour, Ar, Ne, He and H_2 [194]. Of these, the atoms and diatomic molecules do not have vibrational absorption lines and I confirmed that there were no interfering absorption features between methane, carbon dioxide, and water vapour by modelling the absorption with absorption data from the HITRAN 2016 database [75] using the HITRAN Application Programming Interface (HAPI) [195]. Similarly, I modelled O_3, N_2O, CO, NO, SO_2, NO_2, and H_2S as possible contaminants and found that they had no strong absorption features at wavelengths which would interfere with CH_4 and CO_2. Additionally, their concentration in the atmosphere is orders of magnitude less than either methane or carbon dioxide [196], thus the IR attenuation at the wavelengths characteristic of CO_2 and CH_4 under atmospheric conditions is negligible.

In order to model the path of rays through an integrating sphere and verify the model of Eq. 6.1, I developed a Monte Carlo simulation in Mathematica; the code is listed in Appendix A. This simulation launched rays straight down from the top of the integrating sphere. When they reached the bottom of the integrating sphere, a series of conditions were checked to determine if the ray was absorbed, and if not then it was reflected at a random angle. This process was repeated until the ray is either absorbed or reaches the detector.

There are a number of conditions for absorption. First, the Beer-Lambert law is applied to determine the probability that the ray was absorbed during the path it travelled across the sphere. If the ray strikes any of the ports, or a thin ring around where the two halves of the sphere seal together, it is assumed that the ray is lost. There is also a chance that the ray is absorbed even if it doesn't strike one of the ports. The reflectivity of gold, calculated for normal incidence from the Fresnel equations, is 99.4% at 1654 and 2004 nm, and 99.5% at 3260 nm. Finally, if the ray strikes the detector at an angle outside of its angle of acceptance of 35° (for the detector used in the experiments to follow) then it is also lost. The path length for each ray which passes these checks and reaches the detector is then calculated.

The distribution of the rays seems to closely follow that of an exponential distribution, $\lambda e^{-\lambda x}$, where x is the path length and the mean path length of rays that reach the detector is $1/\lambda$. The mean path length seems to closely match that given by Eq. 6.1, agreeing to within 0.5% for 1 million rays cast. The average path length through the integrating sphere with a radius of 38.1 mm and reflectivity of 99.5% integrating sphere is 2.428 m from Eq. 6.1, and 2.442 ± 0.006 m from the simulation. The histogram in Fig. 6.1 shows the distribution of path lengths from one such simulation.

To estimate the limit of detection (LoD) of the sphere, we assumed that the minimum detectable change in light incident on the detector ($\Delta\phi_{\mathrm{min}}$) would be equal to the noise equivalent power (NEP) of the detector multiplied by the bandwidth; accordingly, $\Delta\Phi_{\mathrm{min}} = \mathrm{NEP}\cdot\sqrt{B}$, where $B = 0.35/\tau_{\mathrm{r}}$ and τ_{r} is the manufacturer-specified rise time of the photodiode [197]. The radiant flux at the detector is

$$\Phi_d = \frac{\Phi_{\mathrm{i}} A_{\mathrm{d}} \Omega}{\pi A_{\mathrm{s}}} M, \tag{6.3}$$

where Φ_{i} is the laser power injected into the sphere, A_{d} is the exposed

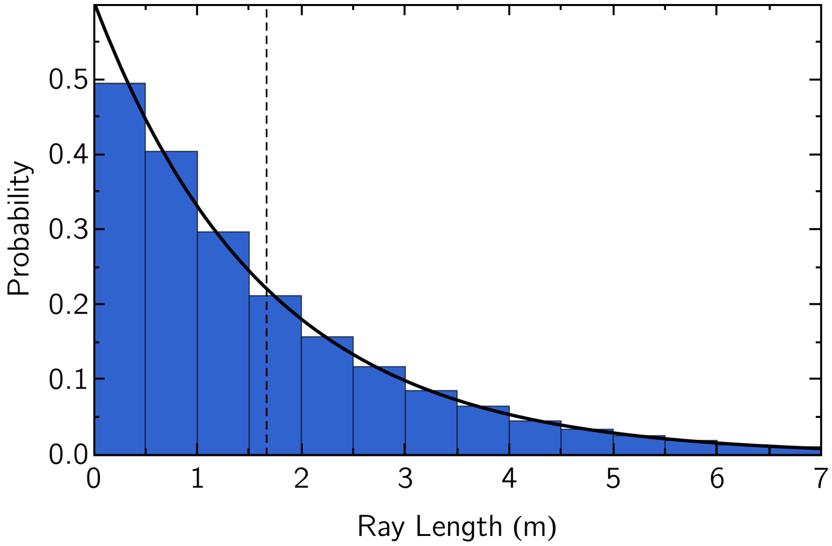

Figure 6.1 Histogram of the distribution of path lengths through an integrating sphere generated by the Monte Carlo simulation. One million rays were simulated with approximately 10% of those reaching the detector. The solid line represents the exponential distribution with λ equal to the inverse of the mean path length, and the dashed line indicates the mean path length.

area of the detector, A_s is the surface area of the sphere, and Ω is the solid angle describing the field of view of the detector [198]. Thus, the minimum detectable change in the light flux is

$$\Delta\Phi_\mathrm{min} = \Phi_\mathrm{d}(1 - e^{-\alpha c_\mathrm{min} L_\mathrm{eff}}), \tag{6.4}$$

where α is the absorption coefficient, c_min is the minimum detectable mole fraction of the gas, and L_eff is the path length calculated above. Rearranging, we find that

$$c_\mathrm{min} = -\frac{1}{\alpha L_\mathrm{eff}} \ln\left(1 - \frac{\Delta\Phi_\mathrm{min}}{\Phi_\mathrm{d}}\right). \tag{6.5}$$

A summary of the expected LoDs for a sphere with a radius of 38.1 mm and 99.5% reflectivity are given in Table 6.1. The main factors that affect

Table 6.1 Specifications and theoretical detection limits for the FGA21 (1654 nm), FD10D (2004 nm), and VL5T0 (3260 nm) photodiodes used in this work. A Φ_i of 10 mW was used for the first two detectors, and 1 mW for the third.

Wavelength (nm)	α (cm^{-1})	NEP (W·Hz$^{-1/2}$)	τ_r (ns)	c_{min} (ppm)
1653.73	0.37	6.0×10^{-14}	25	0.09
2003.50	0.14	1.0×10^{-12}	25	16.25
3260.23	50.40	8.0×10^{-11}	120	1.24

the detection limit are the strength of the absorption feature and the noise equivalent power of the photodetector. Comparing the methane detection limits at 1654 nm ($2\nu_3 R_3$) and 3260 nm ($\nu_3 R_4$), the absorption coefficient is more than two orders of magnitude greater at 3260 nm, but the NEP of the FGA21 detector used for 1654 nm light is more than 3 orders of magnitude smaller than the MIR detector used in the experiments to follow.

6.3 Designing and building integrating spheres

We next designed and built a custom-made integrating sphere that is compact, easy to take apart, has an inlet and outlet for gas, ports for a laser and detector which were positioned without a direct view of each other, and a fibre port for sampling the light inside the sphere if necessary. Ultimately, we designed a sphere with a 38.1 mm inner radius which we manufactured using three different systems: 3D-printed from acrylonitrile butadiene styrene (ABS) on two different kinds of printers, and CNC-machined from aluminum.

The first model was 3D-printed on a Prusa MK3S from white ABS plastic filament; this sphere will be referred to as model V1. A second one was printed on a Stratasys J750 printer (V2), also from ABS plastic, and a final one was machined from aluminum in the Department of Physics machine shop (V3). The V1 sphere was sanded to remove imperfections from the printing process, and the aluminum sphere was sand-blasted to roughen the surface and produce more diffuse reflections. The Stratasys sphere had no noticeable imperfections, but seemed to be rough enough to prevent specular reflection. The printed and machined spheres are shown in Fig. 6.2. All three models were printed or machined to the same dimensions, and their expected detection limits are shown in Table 6.1 assuming 98.5% reflectivity of the sphere surface.

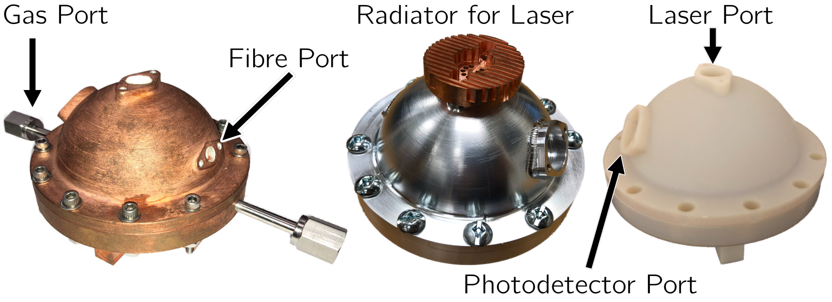

Figure 6.2 Images of the integrating spheres. **Left** A sphere 3D-printed from ABS on a Prusa MK3 and then electroplated in copper (V1). **Centre** A sphere machined from aluminum and shown with the laser cooling radiator attached (V3). **Right** A sphere 3D-printed from ABS on a Stratasys J750 printer (V2). All spheres have the same design.

In order to increase the reflectivity of the surface, films were either electroplated or thermally evaporated onto the surface of the spheres. The V1 sphere was coated with a layer of conductive silver paint. The sphere was then placed into a bath of Caswell copper plating solution (primarily Cu_2SO_4), and the cathode was attached to the sphere, contacting the silver paint. A copper anode was placed into the bath without touching the sphere, and the anode and cathode were connected to a DC power supply. The power supply was set to 0.85 A and 16.8 V in current-limited mode. The plating was allowed to run for 4 hours to produce a copper layer approximately 0.1 mm thick, and excess solution was then rinsed off with water. Finally, the copper coating was lightly sandblasted to roughen the surface.

Sphere V1 then had gold coated on top of the copper layer using Caswell's 24 ct gold tank plating solution, a gold anode, and the same electrical conditions as for the copper. This time the plating was only run for about 2 hours, until a thin layer of gold formed completely over the surface of the copper. The sphere was rinsed with water and then dried with air to avoid contamination of the gold surface. Figure 6.3 **a** and **b** show the V1 sphere before and after gold plating. The initial copper film was primarily to test the reflective properties of copper, however the gold film was a better long-term solution due to its greater stability against oxidation. Sphere V2 received only a copper coating using the same electrical parameters as V1.

The aluminum sphere, V3, was first roughened by sandblasting, and then a layer of gold was thermally evaporated onto the surface by physical vapour deposition. Figure 6.4 shows SEM images of the sandblasted surface of sample aluminum swatches. I tried layering silicon and/or silicon dioxide over the gold layer to try and increase the reflectivity of the swatches. However, due to the hemispherical shape of each half of the integrating sphere, it wasn't possible to accurately measure the film thickness so I just deposited gold. The mass of gold calculated to coat a hemisphere with a 38.1 mm radius in a uniform 100-nm-thick layer was placed into a tungsten/molybdenum boat and the evaporation continued until all of the gold had been deposited. The gold appeared to adhere well to the aluminum, forming a film that followed the contours of the sandblasted aluminum (Fig. 6.3 **c**, **d**).

6.4 Experimental Setup

Tanks of methane at concentrations of 496.2±9.9 ppm (nominally 500 ppm) or 3.755 ± 0.020%) or carbon dioxide with a concentration of 97.2 ± 4.9 ppm (nominally 100 ppm) and 99.999% nitrogen were procured from Praxair. In

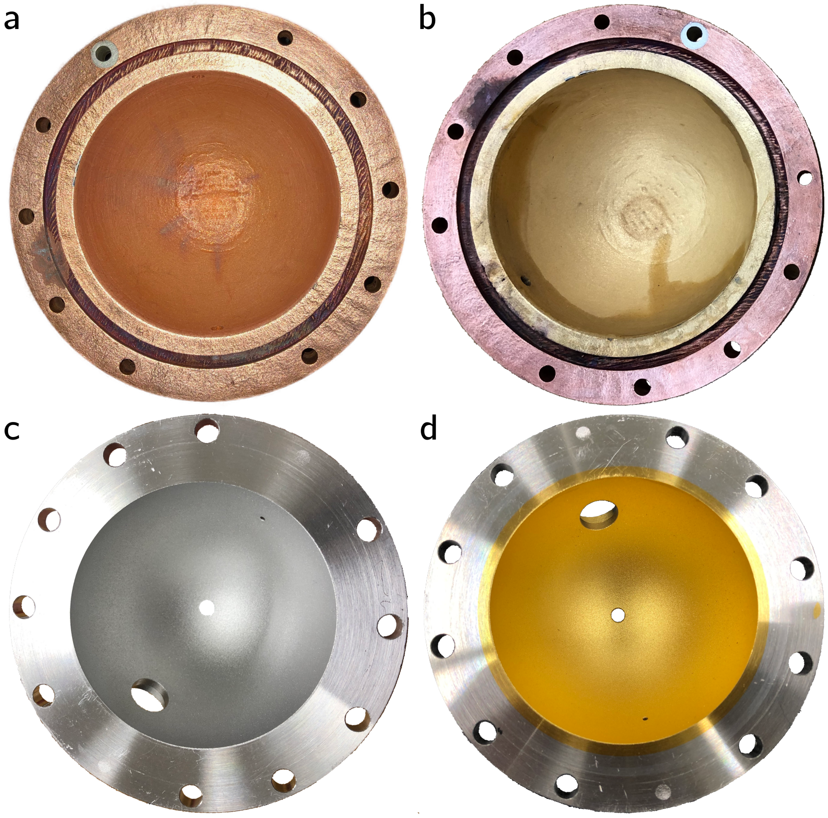

Figure 6.3 Images of the interiors of integrating spheres V1 and V3. **a** V1 sphere 3D-printed from ABS on a Prusa MK3S and then electroplated in copper. **b** Same as **a** but with an electroplated gold layer on top of the copper. **c** The V3 machined aluminum sphere after sandblasting but before physical vapour deposition of the gold film. **d** Same as **c** but with the gold film deposited.

the case of the methane and carbon dioxide cylinders, the remainder of the gas was nitrogen. These cylinders were regulated to 100 ± 5 kPa and connected to either a high-rate (Dwyer VFA-6) or low-rate (Swagelok VAF-G1-01M) gas flow controller. The flow controllers joined at a T-junction which was then connected to the inlet port of an integrating sphere. An additional port on the sphere served as the gas outlet port. Sapphire windows were installed on all 3 optical ports which served to make the integrating sphere airtight. One optical port was meant for fibre coupling in case we

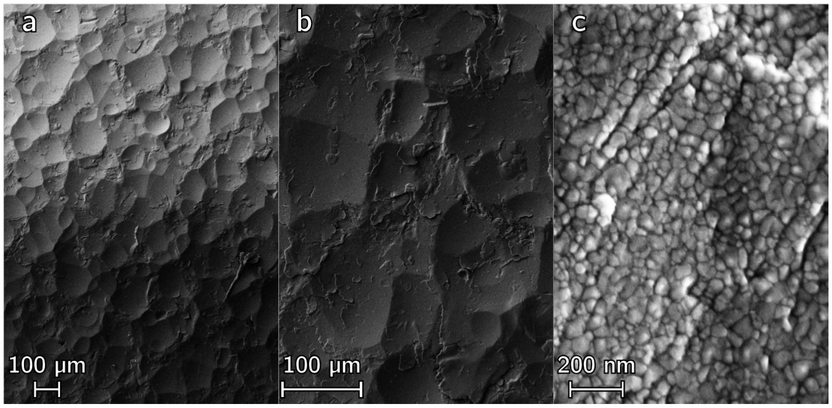

Figure 6.4 SEM images of sandblasted aluminum swatches with an 8 nm base chromium layer, followed by an 80 nm gold layer, and then a 454 nm silicon layer. Films were deposited via electron beam physical vapour deposition after sandblasting. Due to the difficulty of measuring layer thickness in a sphere, I ended up only using a gold layer on the V3 sphere. **a** Secondary electron (SE) image at 50X magnification. **b** SE image at 150X magnification. **c** In-lens image at 50,000X magnification.

needed to connect a spectrometer or other optical device. Of the remaining two ports, the top port was used to mount the laser, and the final port was where the sensor was mounted. A diagram of the experimental setup is shown in Fig. 6.5.

Three distributed feedback (DFB) lasers in TO packages were purchased from Norcada: 1654 nm and 3260 nm for methane, and 2004 nm for carbon dioxide. A Thorlabs TED200C thermoelectric temperature controller (TEC) was connected to the laser for temperature stabilization, and a Thorlabs LDC205C laser diode controller (LDC) provided power to the laser. The pin connections between the laser and controllers are shown in Table 6.2 for the TEC, and 6.3 for the LDC; diagrams of these connections are also shown in Fig. 6.6. The output of the laser was scanned over a small wavelength range (2-3 nm, typically) in order to sample an absorption peak. This was achieved by applying a combination of two voltage signals from a Liquid Instruments Moku:Lab waveform generator to the LDC. The LDC current output was modulated based on

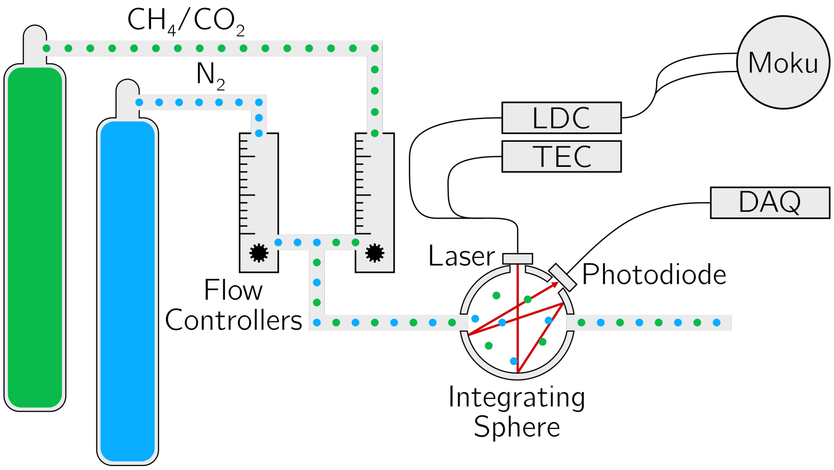

Figure 6.5 Diagram of the setup for laser absorption spectroscopy experiments. Tanks of high purity nitrogen and one of the two greenhouse gases are combined by flow controllers and flow into the integrating sphere. The Moku device provides up to two waveforms (ramp and sine) which are combined and sent to the laser diode controller. Both the LDC and thermoelectric controller (TEC) are connected to the laser diode. The emitted radiation bounces off the walls of the spheres until it enters the photodiode which is connected to a data acquisition module (DAQ).

the input signal according to the formula

$$I = I_{\mathrm{SET}} + I_{\mathrm{MAX}} \cdot \frac{U_{\mathrm{MOD}}}{10\,\mathrm{V}}, \tag{6.6}$$

where I is the output current, I_{SET} is the base current with no modulation, I_{MAX} is the maximum current of 500 mA, and U_{MOD} is the time-varying modulation voltage from the waveform generator.

Detection of the laser light at the output port of the integrating sphere was performed by either an FGA21 InGaAs photodiode for 1654 nm light, an FD10D InGaAs photodiode at 2004 nm, or a VL5T0 HgCdTe photovoltaic detector at 3260 nm, all purchased from Thorlabs. These detectors were connected to a Resolved Instruments DPD80 USB data acquisition (DAQ) device which streams 14-bit information at 20 MSamples/s to a computer.

Table 6.2 Pin arrangement for connecting thermoelectric controller to the laser.

TEC Pin	Laser Pin	Purpose
2	2	Thermistor +
3	8	Thermistor -
4	1	TEC +
5	9	TEC -

Table 6.3 Pin arrangement for connecting laser diode controller to the laser. The laser cathode pin was connected to ground to run in cathode-grounded mode.

LDC Pin	Laser Pin	Purpose
3	3	Ground
3	5	Laser Cathode to Ground
8	7	Laser Anode

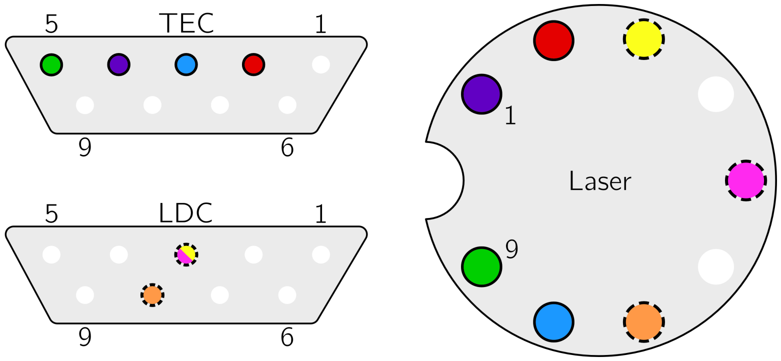

Figure 6.6 Pin diagrams for the thermoelectric controller (TEC), laser diode controller (LDC), and the laser. The ground of the LDC (pin 3) was connected to both the cathode (pin 3) and the ground (pin 5) of the laser.

6.5 Procedure

The integrating spheres were initially tested with only a copper coating on the V1 sphere, and bare ABS and aluminum for the V2 and V3 spheres. These tests were performed with both the 1654 nm and 3260 nm lasers and methane gas. Summaries of the settings for these runs are shown in Table 6.4. The reflectance of the V2 sphere with no copper coating was too low to get any usable results. The V1 and V3 spheres were then coated with gold films and the experiments were run again to analyze any improvement in the detection limit.

The thermoelectric temperature controller (TEC) was set to a resistance of $10\,\mathrm{k}\Omega$ to keep the 1654 nm laser at a temperature of $25\,^{\circ}\mathrm{C}$, $12.49\,\mathrm{k}\Omega$ to keep the 2004 nm laser at $20\,^{\circ}\mathrm{C}$, or $26.87\,\mathrm{k}\Omega$ ($4\,^{\circ}\mathrm{C}$) for the 3260 nm laser based on the manufacturer's data sheet for each laser. The laser diode controller (LDC) was then powered on and slowly ramped to the base current listed in Table 6.4. A ramp waveform with a frequency of 25 Hz and the associated peak-to-peak voltage was generated by our Moku waveform generator and delivered to the LDC, resulting in an output current given by Eq. 6.6.

Table 6.4 Summary of the settings used for methane and carbon dioxide LAS experiments. Spheres V1 and V2 had a copper coating, V1 later had a gold coating applied over the copper, and V3 was either bare aluminum or had a gold film. LDC current is the base current supplied to the laser from the laser diode controller and was modulated by a ramp waveform with the listed peak-to-peak voltage.

Sphere	Wavelength (nm)	Current (mA)	Ramp (Vpp)	Gain
V1 w/ Cu	1654 nm	55	1.3	2
V1 w/ Au		55	1.3	2
V2 w/ Cu		55	1.3	2
V3		55	1.3	2
V3 w/ Au		55	0.8	2
V1 w/ Au	2004 nm	110	0.25	3
V3 w/ Au		110	1.0	2
V1 w/ Cu	3260 nm	150	1.3	4
V1 w/ Au		165	0.95	4
V2 w/ Cu		165	0.95	4
V3		160	1.0	4
V3 w/ Au		160	1.3	4

Measurements for methane at 1654 nm were taken over the widest concentration range due to the weaker absorbance of methane at that wavelength. Measurements covered the range from 0 ppm to 37,550 ppm by mixing the flow from either a 500 or 37,550 ppm source cylinder with high purity nitrogen. The gain of the FGA21 photodiode was set to 2 as in Table 6.5 through the DAQ device's interface, and 2 seconds of signal was collected at each concentration corresponding to 40 million data points. The gain settings 1–4 on the Resolved Instruments DAQ correspond to a transimpedance amplification of 3.3 kV/A, 33 kV/A, 330 kV/A, and 3.3 MV/A. These settings result in amplification of the optical power by 0 dB, 10 dB, 20 dB, and 30 dB compared to gain level 1.

The much higher absorbance of methane at 3260 nm meant that much less light reached the VL5T0 detector, so the detector gain was set to 4, its maximum. The concentrations ranged from 0 to 37550 ppm initially, but response of the sensor tapered off at high concentrations as nearly all the light was absorbed. Later experiments ranged from 0 to 500 ppm. Collection times were identical to the 1654 nm case.

Carbon dioxide measurements at 2004 nm were made over concentrations ranging from 0 to 10,000 ppm by mixing 1% CO_2 with high-purity N_2. Based on the level of light reaching the photodetector, the gain was set to 3 which corresponds to an amplification of 330 kV/A as discussed above.

6.6 Results and Analysis

The raw data collected for each concentration consists of 40 million 14-bit numbers collected from the Resolved Instruments DAQ and takes 2 seconds to collect. A representative sample is shown for a 3260 nm experiment in Fig. 6.7 **a**. The data was imported and filtered with a zero-phase, second order Butterworth filter with a cutoff frequency of 3 kHz.

The zero-phase filtering was achieved by applying the filter to both the forward and reversed datasets and averaging them. The data for each concentration was partitioned into sets of 800,000 points, representing a single ramp of period 0.04 s, and then the middle 48 partitions were averaged; the first and last partition were discarded to avoid edge effects from the filtering. A linear fit was performed to the background of the data for each concentration to remove the effect of the ramp signal. Then, a cubic polynomial was fit to the zero concentration dataset and subtracted from all of the datasets. This was done to account for the nonlinearity of the laser response to the input current. The result of this process is shown in Fig. 6.7 **b**.

The area under each curve, such as in Fig. 6.7 **b**, was integrated, and the detection limit calculated as follows. In the case of the 1654 nm methane data (Fig. 6.8 **a**) and 2004 nm carbon dioxide data (Fig. 6.8 **b**), a linear fit was performed to the integrated area as a function of concentration. The linear fit for methane was performed on the data with concentrations less than or equal to 500 ppm. In order to measure above 500 ppm, it was necessary to switch to a more concentrated gas cylinder and this sometimes caused jumps in the data between 500 ppm and the next higher concentration. The detection limit was calculated as 3 times the uncertainty in the y-intercept divided by the slope of the fit.

In the case of 3260 nm data (Fig. 6.8 **a**), a different model was needed because the much larger absorption coefficient at 3260 nm means that at high concentrations, no light reaches the detector at all. This results in the integrated area eventually saturating such that an increase in concentration produces no increase in the magnitude of the apparent absorbance. Since the integrated area represents the absorbed light, the model was developed by subtracting the predicted optical power at the detector (Eq. 6.3) from the power when the concentration is zero. The model I used to fit the absorbance-concentration data was a slight modification of the formula in

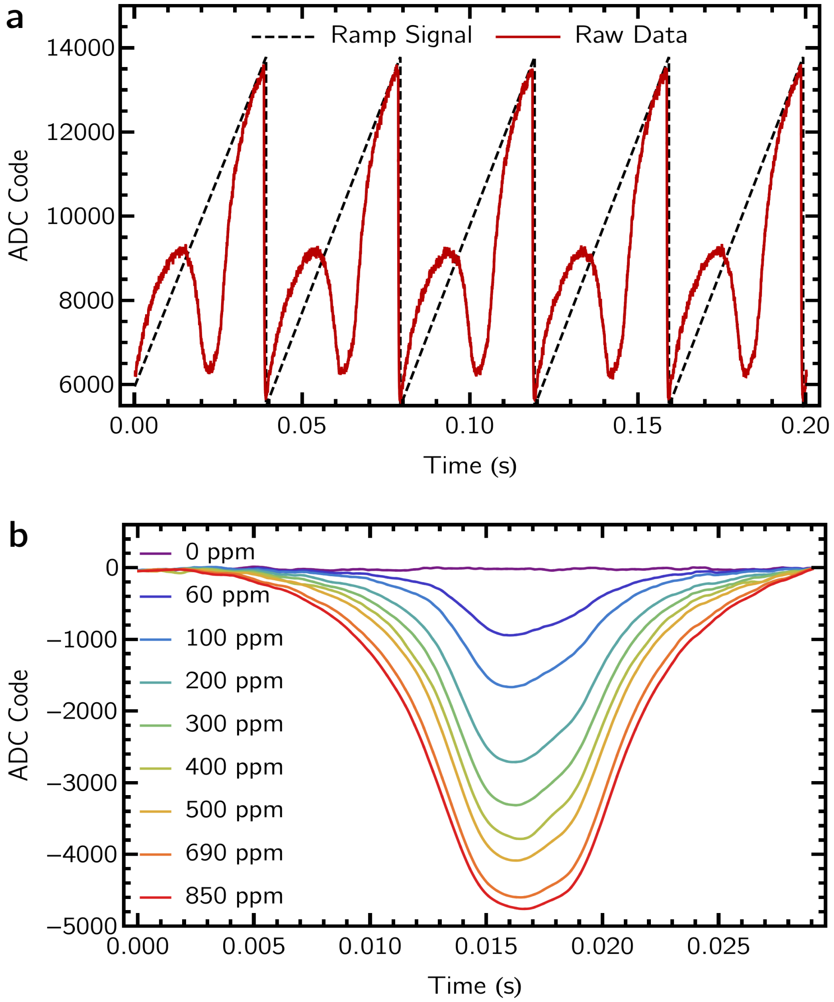

Figure 6.7 **a** An example of the raw data collected with the 3260 nm laser for a methane concentration of 850 ppm. The dashed black line is a representation of the ramp signal meant to guide the eye. **b** Plot of the data from a 3260 nm methane experiment from 0 to 850 ppm after corrections. The data was collected with the V3 sphere with a gold film applied.

Tranchart et al. [100]. The fractional absorption is given by

$$\frac{I_0 - I}{I_0} = a\frac{\alpha c L_{\mathrm{eff}}}{1 - \rho(1 - \alpha c L_{\mathrm{eff}})(1 - f)} + d, \tag{6.7}$$

where I is the intensity of the signal, I_0 is the intensity of the signal at zero concentration, a is a scaling constant, d is an offset, and α, c, L_{eff}, f are the absorption coefficient, molar concentration, effective path length, and port fraction, as previously defined. The port fraction for the spheres was calculated to be 0.0016. In this case, the detection limit was taken to be 3 times the uncertainty in the y-intercept divided by the slope at 0 ppm.

The results are summarized in Table 6.5. In every case, the detection limit for methane was better at 3260 nm than 1654 nm. This was what I had hoped to see when starting this project, as the absorption strength at 3260 nm is over 100 times greater. However, this does not appear to agree with the increase in the theoretical detection limit as we move from 1654 nm to 3260 nm (Table 6.1). There is no obvious *a priori* reason why this should be the case, so a few possible reasons for the disagreement between the theoretical LoD and the much worse ones obtained experimentally are given below.

First, the bandwidth of the photodetector is given by

$$B = \frac{1}{2\pi R_{\mathrm{f}} C}, \tag{6.8}$$

where R_{f} is the transimpedance amplification and C is the capacitance of the diode [199]. Thorlabs does not provide the capacitance for both the FGA21 and VL5T0 photodiodes, but the transimpedance amplification of the photodiode system is two orders of magnitude greater for the VL5T0 (3.3 MV/A) which runs in gain mode 4 than for the FGA21 (33 kV/A) which runs in gain mode 2. As bandwidth decreases with increasing transimpedance amplification, the greater amplification when running in gain mode 4 may explain why the detection limits are better at 3260 nm when the model, which calculates bandwidth from the manufacturer's specified rise time, indicates detection limits should be better at 1654 nm.

The reflectance from the gold coatings might be lower than predicted

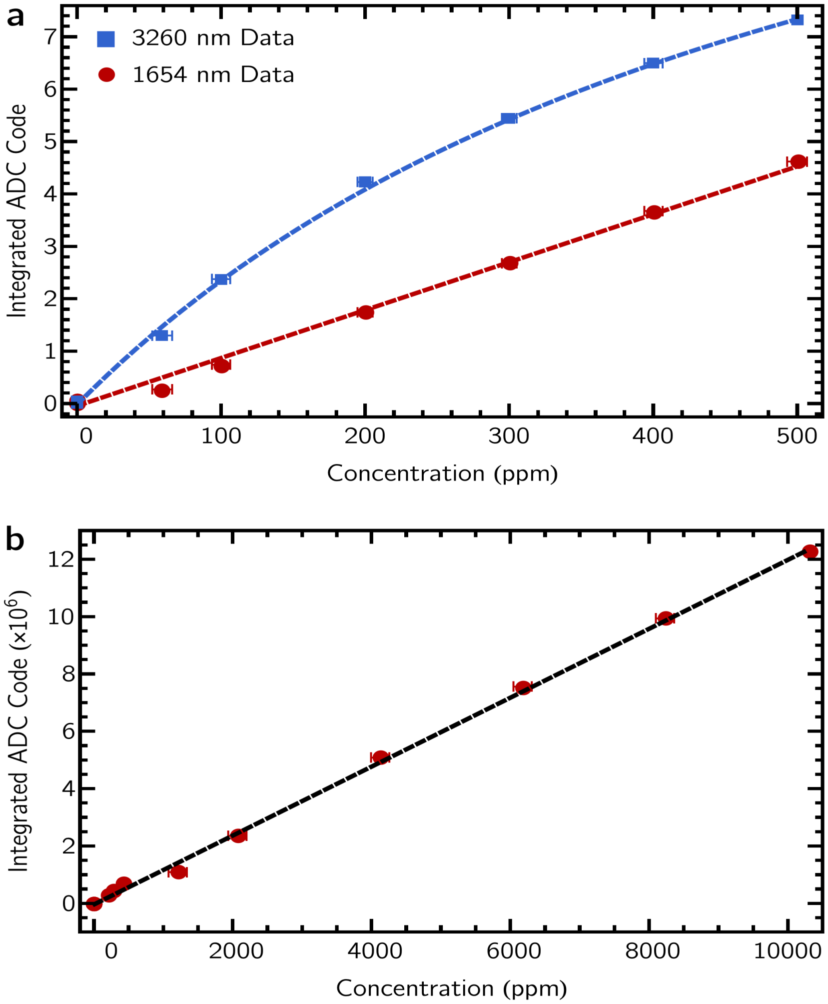

Figure 6.8 **a** Fits to the data for 1654 nm and 3260 nm methane experiments in the V3 sphere with gold coating. The 3260 nm data has been scaled down by a factor 10^8 and the 1654 nm data has been scaled down by 10^6. **b** Best-fit line to the data for a 2004 nm carbon dioxide experiment in the V3 sphere with gold coating. Vertical error bars are smaller than the markers in the above plots.

on the basis of the published optical constants. Fitting Eq. 6.7 to 3260 nm data from the gold-coated V3 sphere gives an experimental reflectance of $(91.2 \pm 0.7)\,\%$, which is substantially lower than the theoretical 99.5% reflectivity for gold. Reducing the reflectivity used in the theoretical LoD calculation from 99.5% to 91.2% results in a 30-fold increase of the LoD, which would be in good agreement with the experiment. As the films deposited through electron beam physical vapour deposition looked to be of high quality from a visual inspection, it seems unlikely that the reflectance would be that much lower than the theoretical value due to film defects alone. Labsphere [200] and NewPort [201], which manufacture integrating spheres commercially, claim a reflectance of around 95% for their gold-coated spheres at the wavelengths explored in this thesis; this coating would provide approximately a 3-fold improvement of the LoD.

There are a number of other factors that enter into Eq. 6.5 which could affect the LoD. The LoD scales inversely with the laser power; if the lasers were not outputting their full power, it would result in worse LoDs. For small changes in the port fraction f, the detection limit scales linearly. However, it seems unlikely that the port fraction is off by even a factor of 2, which would only result in doubling the detection limit. The LoD is proportional to the inverse square root of the detector area. While a larger detector could provide some improvement, the value is supplied by the manufacturer and should not contribute to the lower-than-predicted LoDs. If the photodiode was set back more than expected from the sphere or the detector port was smaller than expected, the solid angle over which the photodiode can collect light would be decreased. The detector port is designed to hold multiple photodiodes with different physical dimensions, so it's possible that the detector is not held at exactly the right distance. In determining the theoretical LoD I assumed a half-angle of 35°, but this could be as low as 24° in the worst case (a difference in position of 5 mm) which would roughly double the LoD.

The photodiode and DAQ also play a role in determining the LoD. Smaller values of noise equivalent power (NEP) mean lower detection limits. The NEP used in calculating the theoretical detection limits was just the manufacturer's quoted value for the bare photodiode. It's possible that the setup contributed noise above that level, resulting in worse LoDs. The NEP and the LoD scale with the square root of the bandwidth. Since the bandwidth can take on a wide range of values from Hz up to MHz, it can have a substantial effect on the LoD. Since the exact bandwidth of the DAQ/photodiode system is not known, future work might involve characterizing the bandwidth and reducing it as much as possible to get the best LoD.

As expected, based on the higher theoretical infrared reflectance of copper, the spheres coated with copper coatings outperformed the bare aluminum one. The experimental reflectances of the spheres were estimated by fitting to Eq. 6.7 and the uncertainty was given by the standard error of the reflectance parameter; the results showed that copper was more reflective than aluminum at 3260 nm. The copper-coated V1 sphere had a reflectance of (87 ± 1) % and copper-coated V2 was (87.0 ± 0.6) % reflective, compared to (84 ± 5) % for bare aluminum. Interestingly, the detection limits appear to be worse for the V1 sphere after the gold coating was added. They go from 28.4 ± 1.0 ppm to 37 ± 2 ppm at 1654 nm, and from 7.6±0.8 ppm to 11±2 ppm at 3260 nm, though the large uncertainty at 3260 nm precludes any firm conclusion. I suspect that this was due to the dark areas visible on the gold coating in Fig. 6.3 **b**. However, for the aluminum spheres, the gold coating always results in an improved detection limit.

While only two experiments were performed with carbon dioxide (spheres V1 and V3 with gold coatings) I was able to achieve a detection limit well below the atmospheric level of around 405 ppm [202]. These measurements also show that gold deposited onto a sandblasted aluminum surface through physical vapour deposition produced a better coating and lower detection limits than the electroplating method did.

Table 6.5 Summary of the detection limits (DL) for methane and carbon dioxide LAS experiments. Spheres V1 and V2 had a copper coating, V1 later had a gold coating applied over the copper, and V3 was either bare aluminum or had a gold film.

Sphere	Wavelength (nm)	Theoretical DL (ppm)	Experimental DL (ppm)
V1 w/ Cu	1654 nm	0.09	28.4(10)
V1 w/ Au			37(2)
V2 w/ Cu			31(1)
V3			85(9)
V3 w/ Au			13.2(3)
V1 w/ Au	2004 nm	16.25	396(11)
V3 w/ Au			99.3(8)
V1 w/ Cu	3260 nm	1.24	7.6(8)
V1 w/ Au			11(2)
V2 w/ Cu			12.0(5)
V3			22(7)
V3 w/ Au			3.4(3)

6.7 Conclusions

Integrating sphere laser absorption spectroscopy offers a path to more economical sensors which are capable of detecting small quantities of greenhouse gases. I have demonstrated that a small aluminum sphere with a thin gold film is capable of detecting 99.3 ± 0.8 ppm carbon dioxide—well below the atmospheric level of 405 ppm [202]. This same sphere can also be used to detect methane by switching the laser source and detector to either 1654 nm or 3260 nm, and demonstrates detection limits of 13.2 ± 0.3 and 3.4 ± 0.6 ppm, respectively. Additionally, I found that a 3D-printed sphere with only a copper coating was capable of achieving detection limits of 28.4 ± 1.0 and 8 ± 2 ppm at 1654 nm and 3260 nm, respectively.

Demonstrating detection of sub-atmospheric levels of greenhouse gases is a substantial first step to creating a commercially viable sensor, but there are likely still some improvements that can be made. During initial tests with depositing gold films onto quartz wafers (with a chromium adhesion layer) we measured a reflectance of over 99% at 1654 nm using a reflectance setup with an NIR spectrometer. Experimentally, the reflectance of the integrating sphere appears to be around 91% at its highest as measured by fitting the experimental data to Eq. 6.7. Improving the reflectance of the coating to the theoretical value of 99.5% would decrease the LoD by a factor of 30, while improving the reflectivity to 98% would still offer a 10-fold improvement.

Ultimately, investigating the reflectance of the film and the bandwidth of the photodetector seem like the most important next steps. The reflectances measured from fitting data to Eq. 6.7 seem quite low. Designing a setup specifically for direct measurements of the reflectance might provide better data. If the reflectance really is lower than expected, then experimentation to improve the reflectance would be a logical step. Labsphere [200] claims a reflectance of over 99% at 1650 nm using a Spectralon coating. While Spectralon's reflectance drops off at MIR wavelengths, using Spectralon could provide a substantial improvement for NIR measurements.

Improvements to the photodetector and signal acquisition would also improve the LoD. Either increasing the area of the detector or increasing its collection angle with a larger port would allow for more light to reach the detector. Adding our own thermoelectric cooling system to the photodiode or purchasing a cooled photodiode such as the Thorlabs PDA10DT would result in lower NEP. The PDA10DT also offers greater control over the gain and bandwidth compared to the current setup employing the FD10D photodiode for 2004 nm measurements. Additionally, the power response of the photodetector should be determined so that the noise level can be measured. If the NEP of the system is much higher than the NEP of the bare photodiode, steps could be taken to reduce the noise such as packaging the photodiode directly in the DAQ to reduce interference, filtering the signal on the DAQ, or selecting a different DAQ for the photodiode to connect to. Implementing the WMS protocol to filter the signal received from the photodetector should also further reduce noise and improve the detection limits.

The most expensive component of this LAS system is the DFB laser. DFB lasers in the mid-infrared are relatively recent, and I expect that their power will increase and cost will decrease over time; at any rate, the cost of the laser would be the same for other types of gas sensors like cavity-enhanced absorption spectroscopy and LAS with a multi-pass cell, but the cost of an integrating sphere, particularly a 3D-printed one, is substantially less.

In addition to improving detection limits through the aforementioned methods, there exist a few other lines of inquiry that might be interesting. The effect of the surface roughness on the integrating sphere was not explored in the current work; I simply used sandblasting to create a rough surface. However, it's possible that a surface with smaller features might be more (or less) diffusely reflective. Hanssen [203] showed that bead-blasted, gold-coated integrating spheres diverged substantially from being ideal Lambertian reflectors. Instead, they used a plasma spray technique to apply nickel followed by an electroplated layer of gold. Exploring such methods for generating a diffusely reflecting coating could improve detection limits.

Detection of molecules dissolved in water would also be interesting because the integrating sphere provides a natural fluidic cavity. Current methods for gases like methane involve headspace measurements where the dissolved methane is allowed to diffuse into the air above the water in an enclosed space for some time. The methane concentration in the headspace is then measured and the concentration in the water is determined indirectly [204, 205]. Directly detecting methane in water would allow for more rapid, real-time determination of the dissolved concentration.

6.8 Acknowledgements

Thanks to David Fortin for making the CAD models of the integrating spheres and Callum Doolin for productive discussions on the Resolved Instruments data acquisition system.

Chapter 7

Conclusion

7.1 Main results

In Chapter 3 I described the development of a refractometric sensor exploiting the Fabry-Perot modes of a silica microcapillary. By shining broadband light from the transmission light source of a microscope onto a microcapillary, FP modes are created in the channel. These modes are sensitive to the optical path length across the channel, and an increase in the refractive index of the fluid in the channel results in an increase in the optical path length causing a redshift of the modes. After travelling through the capillary, the light was collected by a spectrometer and the positions of the modes in the spectrum were analyzed with a Fourier technique, and we demonstrated sensitivity to the pressure of the gas in the capillary, the composition of the gas, and the presence of a sucrose solute in water. This simple device had a refractometric sensitivity of $(5.6 \pm 0.2) \times 10^2$ nm/RIU, and could detect pressure changes as small as

3.3 ± 0.1 kPa.

I demonstrated, to the best of my knowledge, the first example of employing “star” and “triangle” resonances for refractometric sensing in Chapter 4. Star modes are formed when a ray travels around the circumference of the capillary, reflecting off the outer glass-air interface in a manner similar to a whispering gallery mode, but it reflects at such an angle that it travels through the capillary channel before again reflecting at the outer interface. These show up as a series of closely spaced peaks in the spectrum of the device, and are modulated by an envelope created by triangle modes—interferences generated between light light travelling through the channel meeting up with light which reflected from the outer glass-air interface. Shifts of these modes were again analyzed with a Fourier technique and we found that star modes redshift with increasing refractive index, but triangle modes actually blueshift. Combining these opposite shifts yielded refractometric sensitivities in excess of 1000 nm/RIU.

In conjunction with Professor Zhihong Zhang, we then put these modes to the test in detecting the specific binding of polystyrene microspheres to the capillary wall in Chapter 5. Using the same style of glass microcapillary, we deposited polyelectrolyte layers of PAH and PSS on the capillary channel. We then excited a rhodamine B solution using a high-power nitrogen laser, resulting in lasing star and triangle modes. We measured the spectrum before and after pumping carboxy-functionalized polystyrene microspheres into the capillary and binding them to the electrolyte layer through reaction with EDC and NHS. The shift in the mode positions showed that the system was sensitive to different amounts of microspheres bonded to the walls and showed that a refractometric sensor using these modes could be made specific to a particular analyte.

Finally, I worked to develop an integrating sphere laser absorption spectroscopy platform for the measurement of greenhouse gases, as outlined in Chapter 6. I discussed the design of the integrating sphere and explore different materials, such as 3D-printing from ABS or machining from aluminum. These spheres can be produced much more economically than multi-pass cells, and require no alignment as laser light injected into the sphere reflects randomly until it reaches the photodetector or is absorbed by the gas. The wavelength of the laser was scanned across absorption features of either methane or carbon dioxide, and I demonstrated that the integrating spheres were capable of detecting as little as 3 ppm methane and 100 ppm carbon dioxide.

7.2 Future work and outlook

The techniques described in this thesis have shown the utility of refractometric sensing and laser absorption spectroscopy, but there remain further challenges and opportunities. Simulations show that the FP microcapillaries would have greater sensitivity at telecommunications wavelengths of 1550 nm. Efforts to functionalize the capillaries as we did for the geometric modes of Chapter 5 could also help to remedy the lack of specificity in these sensors, though the relatively small interaction length at the surface of the capillary in FP modes compared to geometric or whispering gallery modes might render this method inefficient. Finally, adapting this platform to a lab-on-a-chip configuration could allow for both smaller analyte volumes and a more compact device.

The integrating sphere LAS system could benefit from higher reflectivity films which should result in lower detection limits. It would be interesting to explore the effects of different kinds of surface coatings and the roughness of those coatings on the detection limits. Limiting the bandwidth of the photodetector would also improve the LoD. A logical next step for the project would be to test wavelength modulation spectroscopy (WMS) in the integrating spheres and compare the detection limits to the direct detection results outlined in this thesis. A further benefit of WMS would be that the pressure and temperature of the gas could be extracted from the fitting results.

As the sphere is a closed system, it would be interesting to expand its capabilities to liquids. A possibility would be to explore the detection of gases such as methane and carbon dioxide in water. Integrating spheres have previously been applied to the task of measuring microalgae and other dissolved organic materials [206], so measuring gases seems like a logical step. However, water has non-negligible absorption at infrared wavelengths, and the absorption is very high in the mid-infrared. Greater absorption by the water means a shorter mean path length and worse detection limits. There are some methane absorption features near 887 nm, where water is still relatively transmissive, but they are far weaker than the ones explored in this thesis.

In this thesis, I have attempted to demonstrate the power and versatility of optical sensing technologies. They provide a competitive or even state-of-the-art solution to a wide variety of challenging problems, including the detection of single viruses or nanoparticles, humidity, refractive index, and greenhouse gases. With the fields of photonics and nanofabrication mixing to produce nanoscale photonic chips and optomechanical devices, and lasers and photodetectors improving all the time, I must conclude that we will continue to see evermore impressive optical sensors at ever-decreasing sizes. While this thesis only shines a light on one small corner of the field, I hope it has been illuminating nevertheless.

Bibliography

[1] W. Morrish et al. "Refractometric micro-sensor using a mirrored capillary resonator," *Optics Express* **24** (22), 24959–24970 (2016). DOI: `10.1364/OE.24.024959` (pp. iv, 32, 60).

[2] W. Morrish et al. "Geometric Resonances for High-Sensitivity Microfluidic Lasing Sensors," *Physical Review Applied* **10** (5), 051001 (Nov. 2018). DOI: `10.1103/PhysRevApplied.10.051001` (pp. iv, 58, 77, 80, 85).

[3] Z. Zhang et al. "Functional lasing microcapillaries for surface-specific sensing," *Optics Express* **27** (19), 26967 (2019). DOI: `10.1364/oe.27.026967` (pp. v, 74).

[4] A. M. Fox and D. Fox. "Optical Properties of Solids," Oxford master series in condensed matter physics. Oxford University Press, 2001 (p. 1).

[5] F. L. Pedrotti, L. M. Pedrotti, and L. S. Pedrotti. "Introduction to Optics," Cambridge University Press, Dec. 2017. DOI: `10.1017/9781108552493` (p. 1).

[6] A. J. Das et al. "Ultra-portable, wireless smartphone spectrometer for rapid, non-destructive testing of fruit ripeness," *Scientific reports* **6**. 32504 (2016). DOI: 10.1038/srep32504 (p. 2).

[7] M. Zude and B. Herold. "Optimum harvest date determination for apples using spectral analysis," *Gartenbauwissenschaft* **67** (5), 199–204 (2002) (p. 2).

[8] C. Lang and T. Hübert. "A colour ripeness indicator for apples," *Food and Bioprocess Technology* **5** (8), 3244–3249 (2012). DOI: 10.1007/s11947-011-0694-4 (p. 2).

[9] T. H. M. Akkermans. "Digital control in optical disc drives," *ICCE. International Conference on Consumer Electronics (IEEE Cat. No.01CH37182)*. June 2001, 246–247. DOI: 10.1109/ICCE.2001.935294 (p. 2).

[10] K. Nagatomi et al. "A smart model HD DVD/DVD/CD compatible pickup head," *IEEE Transactions on Consumer Electronics* **52** (1), 150–154 (2006). DOI: 10.1109/TCE.2006.1605040 (p. 2).

[11] Q. Fu et al. "A portable smart phone-based plasmonic nanosensor readout platform that measures transmitted light intensities of nanosubstrates using an ambient light sensor," *Lab on a Chip* **16** (10), 1927–1933 (2016). DOI: 10.1039/c6lc00083e (p. 2).

[12] J. A. Sans et al. "Oscillations studied with the smartphone ambient light sensor," *European Journal of Physics* **34** (6), 1349–1354 (2013). DOI: 10.1088/0143-0807/34/6/1349 (p. 2).

[13] P. Günther et al. "Laser Doppler distance sensor using phase evaluation," *Opt. Express* **17** (4), 2611–2622 (Feb. 2009). DOI: 10.1364/OE.17.002611 (p. 2).

[14] K. Konolige et al. "A low-cost laser distance sensor," *2008 IEEE International Conference on Robotics and Automation*. May 2008, 3002–3008. DOI: 10.1109/ROBOT.2008.4543666 (p. 2).

[15] J. Aasi et al. "Advanced LIGO," *Classical and Quantum Gravity* **32** (7), 074001 (Apr. 2015). DOI: `10.1088/0264-9381/32/7/074001` (p. 2).

[16] H. Zhu et al. "Phage-based label-free biomolecule detection in an opto-fluidic ring resonator," *Biosensors and Bioelectronics* **24** (3), 461–466 (2008). DOI: `https://doi.org/10.1016/j.bios.2008.04.028` (p. 2).

[17] M. D. Baaske, M. R. Foreman, and F. Vollmer. "Single-molecule nucleic acid interactions monitored on a label-free microcavity biosensor platform," *Nature Nanotechnology* **9**. 933 (2014). DOI: `10.1038/nnano.2014.180` (pp. 2, 59, 75).

[18] T. Yoshie, L. Tang, and S.-Y. Su. "Optical Microcavity: Sensing down to Single Molecules and Atoms," *Sensors* **11** (2), 1972–1991 (Feb. 2011). DOI: `10.3390/s110201972` (p. 2).

[19] M. Sumetsky et al. "Optical liquid ring resonator sensor," *Optics Express* **15** (22), 14376–14381 (2007). DOI: `10.1364/OE.15.014376` (pp. 2, 59).

[20] X. Zhang et al. "Coupled optofluidic ring laser for ultrahigh- sensitive sensing," *Optics Express* **19** (22), 22242–22247 (2011). DOI: `10.1364/OE.19.022242` (pp. 2, 60).

[21] H. Lee et al. "Chemically etched ultrahigh-Q wedge-resonator on a silicon chip," *Nature Photonics* **6** (6), 369–373 (June 2012). DOI: `10.1038/nphoton.2012.109`. arXiv: `1112.2196` (p. 2).

[22] N. M. Hanumegowda, I. M. White, and X. Fan. "Aqueous mercuric ion detection with microsphere optical ring resonator sensors," *Sensors and Actuators B: Chemical* **120** (1), 207–212 (Dec. 2006). DOI: `10.1016/J.SNB.2006.02.011` (p. 2).

[23] M. Y. Ye, M. X. Shen, and X. M. Lin. "Ringing phenomenon based whispering-gallery-mode sensing," *Scientific Reports* **6**. (2016). DOI: `10.1038/srep19597` (p. 2).

[24] M. V. Artemyev, U. Woggon, and R. Wannemacher. "Photons confined in hollow microspheres," *Applied Physics Letters* **78** (8), 1032–1034 (2001). DOI: `10.1063/1.1350423` (p. 2).

[25] H. T. Beier, G. L. Cote, and K. E. Meissner. "Whispering Gallery Mode Biosensors Consisting of Quantum Dot-Embedded Microspheres," *Annals of Biomedical Engineering* **37** (10), 1974–1983 (2009). DOI: `10.1007/s10439-009-9713-2` (pp. 2, 75).

[26] Y. Zhi, T. Thiessen, and A. Meldrum. "Silicon quantum dot coated microspheres for microfluidic refractive index sensing," *Journal of the Optical Society of America B-Optical Physics* **30** (1), 51–56 (2013). DOI: `10.1364/josab.30.000051` (pp. 2, 34, 75).

[27] H. Fan et al. "Confined whispering-gallery mode in silica doubletoroid microcavities for optical sensing and trapping," *Optics Communications* **434**. 97–103 (2019). DOI: `10.1016/j.optcom.2018.10.055` (pp. 2, 75).

[28] J. Su, A. F. G. Goldberg, and B. M. Stoltz. "Label-free detection of single nanoparticles and biological molecules using microtoroid optical resonators," *Light-Science & Applications* **5**. (2016). DOI: `10.1038/lsa.2016.1` (pp. 2, 75).

[29] E. Ozgur et al. "Label-Free Biosensing with High Selectivity in Complex Media using Microtoroidal Optical Resonators," *Scientific Reports* **5**. (2015). DOI: `10.1038/srep13173` (pp. 2, 75).

[30] A. Meldrum et al. "Luminescent Capillary-Based Whispering Gallery Mode Sensors: Crossing the Lasing Threshold," *Physica Status Solidi (a)* **1700619** (7), 1700619 (2017). DOI: `10.1002/pssa.201700619` (pp. 2, 7, 60).

[31] V. Zamora et al. "Refractometric sensor based on whispering-gallery modes of thin capillaries," *Optics Express* **15** (19), 12011–12016 (2007). DOI: 10.1364/oe.15.012011 (pp. 2, 75).

[32] I. M. White, H. Oveys, and X. Fan. "Liquid-core optical ring-resonator sensors," *Optics Letters* **31** (9), 1319–1321 (2006). DOI: 10.1364/OL.31.001319 (pp. 2, 9, 75).

[33] C. P. K. Manchee et al. "Refractometric sensing with fluorescent-core microcapillaries," *Optics Express* **19** (22), 21540–21551 (2011). DOI: 10.1364/OE.19.021540 (pp. 2, 34, 59, 75).

[34] H. Li et al. "Analysis of single nanoparticle detection by using 3-dimensionally confined optofluidic ring resonators," *Optics Express* **18** (24), 25081–25088 (2010). DOI: 10.1364/OE.18.025081 (pp. 2, 59).

[35] A. K. Mallik et al. "Agarose coated spherical micro resonator for humidity measurements," *Optics Express* **24** (19), 21216–21227 (2016). DOI: 10.1364/OE.24.021216 (pp. 2, 59).

[36] I. Hernández-Romano et al. "Optical fiber temperature sensor based on a microcavity with polymer overlay," *Optics Express* **24** (5), 5654–5661 (2016). DOI: 10.1364/OE.24.005654 (pp. 2, 59).

[37] N. M. Hanumegowda et al. "Refractometric sensors based on microsphere resonators," *Applied Physics Letters* **87** (20), 201107 (2005). DOI: 10.1063/1.2132076 (pp. 2, 9).

[38] T. Ioppolo et al. "Micro-optical force sensor concept based on whispering gallery mode resonators," *Applied Optics* **47** (16), 3009–3014 (2008). DOI: 10.1364/AO.47.003009 (pp. 2, 59).

[39] A. Mahmood et al. "Magnetic field sensing using whispering-gallery modes in a cylindrical microresonator infiltrated with ferronematic liquid crystal," *Optics Express* **25** (11), (2017). DOI: 10.1364/oe.25.012195 (p. 2).

[40] S. Lane et al. "Protein biosensing with fluorescent microcapillaries," *Optics Express* **23** (3), 2577–2590 (Feb. 2015). DOI: `10.1364/OE.23.002577` (pp. 3, 9, 10, 59, 76, 79, 89).

[41] B. E. A. Saleh and M. C. Teich. "Fundamentals of photonics; 2nd ed." Wiley series in pure and applied optics. New York, NY: Wiley, 2007 (pp. 4, 6).

[42] S. O. Kasap. "Optoelectronics and photonics : principles and practices," 2nd. Pearson, 2013. DOI: `10.1007/s13398-014-0173-7.2`. arXiv: `9809069v1 [arXiv:gr-qc]` (pp. 4, 5).

[43] O. Svelto and D. C. Hanna. "Principles of lasers," 5th. Vol. 1. Springer, 2010. DOI: `10.1007/978-1-4419-1302-9` (p. 5).

[44] H.-J. Moon and D.-Y. Kang. "Strongly enhanced mode selection in a thin dielectric-coated layered microcavity laser," *Optics Letters* **32** (11), 1554–1556 (2007). DOI: `10.1364/OL.32.001554` (pp. 7, 63, 66, 77).

[45] T. Reynolds et al. "Fluorescent and lasing whispering gallery mode microresonators for sensing applications," *Laser & Photonics Reviews* **11** (2), (2017). DOI: `10.1002/lpor.201600265` (pp. 7, 76).

[46] G. Z. Xiao et al. "Monitoring changes in the refractive index of gases by means of a fiber optic Fabry-Perot interferometer sensor," *Sensors and Actuators, A: Physical* **118** (2), 177–182 (2005). DOI: `10.1016/j.sna.2004.08.029` (p. 8).

[47] I. Transactions and O. N. Microwave. "Fiber-Optic Fabry-Perot Interferometer Sensor Applications," 1612–1621 (1982) (p. 8).

[48] H. Y. Choi et al. "Miniature fiber-optic high temperature sensor based on a hybrid structured Fabry-Perot interferometer," *Optics Letters* **33** (21), 2455–2457 (2008). DOI: `10.1364/ol.33.002455` (pp. 8, 34).

[49] W. C. L. Hopman et al. “Quasi-one-dimensional photonic crystal as a compact building-block for refractometric optical sensors,” *IEEE Journal of Selected Topics in Quantum Electronics* **11** (1), 11–16 (Jan. 2005). DOI: `10.1109/JSTQE.2004.841693` (p. 9).

[50] A. F. Obaton et al. “Tilted Fibre Bragg Gratings and Phase Sensitive-Optical Low Coherence Interferometry for refractometry and liquid level sensing,” *Sensors and Actuators A: Physical* **189**. 451–458 (2013). DOI: `https://doi.org/10.1016/j.sna.2012.10.020` (p. 9).

[51] K. Schroeder et al. “A fibre Bragg grating refractometer,” *Measurement Science and Technology* **12** (7), 757–764 (June 2001). DOI: `10.1088/0957-0233/12/7/301` (p. 9).

[52] A. A. S. S. H. A. B. S. R. S. G. EDWALL. “Fiber Optical Bragg Grating Refractometer,” *Fiber and Integrated Optics* **17** (1), 51–62 (1998). DOI: `10.1080/014680398245055` (p. 9).

[53] S.-H. Kwon et al. “Optimization of photonic crystal cavity for chemical sensing,” *Opt. Express* **16** (16), 11709–11717 (Aug. 2008). DOI: `10.1364/OE.16.011709` (p. 9).

[54] A. Di Falco, L. O’Faolain, and T. F. Krauss. “Chemical sensing in slotted photonic crystal heterostructure cavities,” *Applied Physics Letters* **94** (6), 63503 (2009). DOI: `10.1063/1.3079671` (p. 9).

[55] Y.-n. Zhang, Y. Zhao, and R.-q. Lv. “A review for optical sensors based on photonic crystal cavities,” *Sensors and Actuators A: Physical* **233**. 374–389 (2015). DOI: `https://doi.org/10.1016/j.sna.2015.07.025` (p. 9).

[56] S. M. Grist et al. “Silicon photonic micro-disk resonators for label-free biosensing,” *Optics Express* **21** (7), 7994–8006 (2013). DOI: `10.1364/oe.21.007994` (pp. 9, 75).

[57] R. Caroselli et al. "Experimental study of the sensitivity of a porous silicon ring resonator sensor using continuous in-flow measurements," *Opt. Express* **25** (25), 31651–31659 (Dec. 2017). DOI: `10.1364/OE.25.031651` (p. 9).

[58] J. Wu et al. "Rapid 3D µ-printing of polymer optical whispering-gallery mode resonators," *Optics Express* **23** (23), 29708 (2015). DOI: `10.1364/oe.23.029708` (p. 9).

[59] H. Wei and S. Krishnaswamy. "Direct Laser Writing Polymer Micro-Resonators for Refractive Index Sensors," *IEEE Photonics Technology Letters* **28** (24), 2819–2822 (Dec. 2016). DOI: `10.1109/LPT.2016.2623814` (p. 9).

[60] F. Xia et al. "Ultra-compact high order ring resonator filters using submicron silicon photonic wires for on-chip optical interconnects," *Optics Express* **15** (19), 11934 (2007). DOI: `10.1364/oe.15.011934` (p. 9).

[61] A. Francois et al. "Polymer based whispering gallery mode laser for biosensing applications," *Applied Physics Letters* **106** (3), (2015). DOI: `10.1063/1.4905931` (pp. 9, 34, 76).

[62] A. Bianchetti et al. "Refractometry-based air pressure sensing using glass microspheres as high-Q whispering-gallery mode microresonators," *Optics Communications* **394**. 152–156 (2017). DOI: `https://doi.org/10.1016/j.optcom.2017.03.009` (p. 9).

[63] Y. Zhi et al. "Refractometric Sensing with Silicon Quantum Dots Coupled to a Microsphere," *Plasmonics* **8** (1), 71–78 (2013). DOI: `10.1007/s11468-012-9423-8` (p. 9).

[64] M. L. Gorodetsky, A. A. Savchenkov, and V. S. Ilchenko. "Ultimate Q of optical microsphere resonators," *Opt. Lett.* **21** (7), 453–455 (Apr. 1996). DOI: `10.1364/OL.21.000453` (p. 9).

[65] F. Vollmer, S. Arnold, and D. Keng. "Single virus detection from the reactive shift of a whispering-gallery mode," *Proceedings of the National Academy of Sciences of the United States of America* **105** (52), 20701–20704 (2008). DOI: `10.1073/pnas.0808988106` (p. 9).

[66] S. I. Shopova et al. "Optofluidic ring resonator based dye laser," *Applied Physics Letters* **90** (22), 2005–2008 (2007). DOI: `10.1063/1.2743884` (p. 9).

[67] S. Lane et al. "Refractometric sensitivity and thermal stabilization of fluorescent core microcapillary sensors: theory and experiment," *Applied Optics* **54** (6), 1331–1340 (2015). DOI: `10.1364/AO.54.001331` (p. 10).

[68] S. Lane et al. "Whispering gallery mode structure and refractometric sensitivity of fluorescent capillary-type sensors," *Sensors and Actuators B: Chemical* **190**. 752–759 (Jan. 2014). DOI: `10.1016/J.SNB.2013.09.029` (p. 10).

[69] S. A. Mcfarlane. "Fluorescent-Core Microcapillaries : Detection Limits for Biosensing Applications Master of Science," (2013) (pp. 10, 30).

[70] J. W. Silverstone et al. "Ultimate resolution for refractometric sensing with whispering gallery mode microcavities," *Optics Express* **20** (8), 8284–8295 (Apr. 2012). DOI: `10.1364/OE.20.008284` (pp. 10, 29, 41, 42, 47, 65, 85).

[71] C. N. Banwell and E. M. McCash. "Fundamentals of Molecular Spectroscopy," European Chemistry Series. McGraw-Hill, 1994 (pp. 12, 14, 16).

[72] G. Herzberg. "Molecular spectra and molecular structure. Vol.2: Infrared and Raman spectra of polyatomic molecules," 1945 (p. 12).

[73] J. L. McHale. "Molecular Spectroscopy, Second Edition," 2nd Editio. Boca Raton, FL: CRC Press, July 2017, 475. DOI: 10.1201/9781315115214 (p. 12).

[74] D. L. Andrews. "Molecular Photophysics and Spectroscopy," 2053-2571. Morgan & Claypool Publishers, 2014. DOI: 10.1088/978-1-627-05288-7 (pp. 14, 15).

[75] I. E. Gordon et al. "The HITRAN2016 molecular spectroscopic database," *Journal of Quantitative Spectroscopy and Radiative Transfer* **203**. 3–69 (2017). DOI: https://doi.org/10.1016/j.jqsrt.2017.06.038 (pp. 18, 103).

[76] A. O'Keefe, J. J. Scherer, and J. B. Paul. "cw Integrated cavity output spectroscopy," *Chemical Physics Letters* **307** (5), 343–349 (1999). DOI: https://doi.org/10.1016/S0009-2614(99)00547-3 (p. 18).

[77] D. S. Baer et al. "Sensitive absorption measurements in the near-infrared region using off-axis integrated-cavity-output spectroscopy," *Applied Physics B: Lasers and Optics* **75** (2-3), 261–265 (2002). DOI: 10.1007/s00340-002-0971-z (p. 18).

[78] Y. A. Bakhirkin et al. "Mid-infrared quantum cascade laser based off-axis integrated cavity output spectroscopy for biogenic nitric oxide detection," *Applied Optics* **43** (11), 2257–2266 (2004). DOI: 10.1364/AO.43.002257 (p. 18).

[79] D. D. Arslanov et al. "Real-time, subsecond, multicomponent breath analysis by Optical Parametric Oscillator based Off-Axis Integrated Cavity Output Spectroscopy," *Optics Express* **19** (24), 24078 (2011). DOI: 10.1364/oe.19.024078 (p. 19).

[80] B. J. Orr and Y. He. "6 - Cavity-based absorption spectroscopy techniques," ed. by M. B. T. L. S. f. S. Baudelet. Woodhead Publishing,

2014, 167–207. DOI: `https://doi.org/10.1533/9780857098733.2.167` (p. 19).

[81] G. Berden, R. Peeters, and G. Meijer. "Cavity ring-down spectroscopy: Experimental schemes and applications," *International Reviews in Physical Chemistry* **19** (4), 565–607 (2000). DOI: `10.1080/014423500750040627` (p. 19).

[82] D. Romanini et al. "CW cavity ring down spectroscopy," *Chemical Physics Letters* **264** (3), 316–322 (1997). DOI: `https://doi.org/10.1016/S0009-2614(96)01351-6` (p. 19).

[83] J. Morville et al. "Two schemes for trace detection using cavity ring-down spectroscopy," *Applied Physics B* **78** (3-4), 465–476 (Feb. 2004). DOI: `10.1007/s00340-003-1363-8` (p. 19).

[84] B. A. Paldus et al. "Cavity ringdown spectroscopy using mid-infrared quantum-cascade lasers," *Opt. Lett.* **25** (9), 666–668 (May 2000). DOI: `10.1364/OL.25.000666` (p. 19).

[85] A. Kosterev. "Photo-acoustic spectroscopy," *Laser Spectroscopy for Sensing*. Ed. by M. B. T. L. S. f. S. Baudelet. Elsevier, 2014, 208–234. DOI: `10.1533/9780857098733.2.208` (p. 19).

[86] P. Patimisco et al. "Tuning forks with optimized geometries for quartz-enhanced photoacoustic spectroscopy," *Optics Express* **27** (2), 1401 (2019). DOI: `10.1364/oe.27.001401` (p. 19).

[87] K. Liu et al. "Multi-resonator photoacoustic spectroscopy," *Sensors and Actuators, B: Chemical* **251**. 632–636 (2017). DOI: `10.1016/j.snb.2017.05.114` (p. 19).

[88] T. Tomberg et al. "Sub-parts-per-trillion level sensitivity in trace gas detection by cantilever-enhanced photo-acoustic spectroscopy," *Scientific Reports* **8** (1), 1–7 (2018). DOI: `10.1038/s41598-018-20087-9` (p. 19).

[89] S. Coburn et al. “Regional trace-gas source attribution using a field-deployed dual frequency comb spectrometer,” *Optica* **5** (4), 320 (2018). DOI: `10.1364/optica.5.000320` (pp. 19, 100).

[90] P. Werle, R. Mücke, and F. Slemr. “The limits of signal averaging in atmospheric trace-gas monitoring by tunable diode-laser absorption spectroscopy (TDLAS),” *Applied Physics B Photophysics and Laser Chemistry* **57** (2), 131–139 (1993). DOI: `10.1007/BF00425997` (pp. 20, 100, 101).

[91] T. A. Hu et al. “Improved multipass optics for diode laser spectroscopy,” *Review of Scientific Instruments* **64** (12), 3380–3383 (1993). DOI: `10.1063/1.1144308` (p. 20).

[92] E. Lanzinger, K. Jousten, and M. Kühne. “Partial pressure measurement by means of infrared laser absorption spectroscopy,” *Vacuum* **51** (1), 47–51 (1998). DOI: `https://doi.org/10.1016/S0042-207X(98)00132-8` (p. 20).

[93] M. Uddi, A. K. Das, and C. J. Sung. “Temperature measurements in a rapid compression machine using mid-infrared H2O absorption spectroscopy near 7.6 μm,” *Applied Optics* **51** (22), 5464–5476 (2012). DOI: `10.1364/AO.51.005464` (p. 20).

[94] J. B. McManus, M. S. Zahniser, and D. D. Nelson. “Dual quantum cascade laser trace gas instrument with astigmatic Herriott cell at high pass number,” *Applied Optics* **50** (4), (2011). DOI: `10.1364/AO.50.000A74` (p. 20).

[95] M. Graf, L. Emmenegger, and B. Tuzson. “Compact, circular, and optically stable multipass cell for mobile laser absorption spectroscopy,” *Optics Letters* **43** (11), 2434 (2018). DOI: `10.1364/ol.43.002434` (p. 20).

[96] A. Manninen et al. "Versatile multipass cell for laser spectroscopic trace gas analysis," *Applied Physics B: Lasers and Optics* **109** (3), 461–466 (2012). DOI: 10.1007/s00340-012-4964-2 (p. 20).

[97] Z. Yang et al. "Generalized optical design of the double-row circular multi-pass cell," *Sensors (Switzerland)* **18** (8), 1–15 (2018). DOI: 10.3390/s18082680 (p. 20).

[98] M. Graf et al. "Beam folding analysis and optimization of mask-enhanced toroidal multipass cells," *Optics Letters* **42** (16), 3137 (2017). DOI: 10.1364/ol.42.003137 (p. 20).

[99] E. Hawe et al. "Hazardous gas detection using an integrating sphere as a multipass gas absorption cell," *Sensors and Actuators, A: Physical* **141** (2), 414–421 (2008). DOI: 10.1016/j.sna.2007.10.070 (pp. 21, 103).

[100] S. bastien Tranchart, I. H. Bachir, and J.-L. Destombes. "Sensitive trace gas detection with near-infrared laser diodes and an integrating sphere," *Applied Optics* **35** (36), 7070 (Dec. 1996). DOI: 10.1364/AO.35.007070 (pp. 21, 117).

[101] C. G. Venkatesh, R. S. Eng, and A. W. Mantz. "Tunable diode laser–integrating sphere systems: a study of their output intensity characteristics," *Appl. Opt.* **19** (10), 1704–1710 (May 1980). DOI: 10.1364/AO.19.001704 (p. 21).

[102] J. Hodgkinson, D. Masiyano, and R. P. Tatam. "Using integrating spheres as absorption cells: Path-length distribution and application of beer's law," *Applied Optics* **48** (30), 5748–5758 (Oct. 2009). DOI: 10.1364/AO.48.005748 (p. 21).

[103] X. Wei and D. K. Roper. "Tin Sensitization for Electroless Plating Review," *Journal of the Electrochemical Society* **161** (5), D235–D242 (2014). DOI: 10.1149/2.047405jes (pp. 24, 38).

[104] X. Fan and I. M. White. "Optofluidic microsystems for chemical and biological analysis," *Nature Photonics*. (2011). DOI: `10.1038/nphoton.2011.206` (p. 33).

[105] J. Jágerská et al. "Refractive index sensing with an air-slot photonic crystal nanocavity," *Optics Letters* **35** (15), 2523–2525 (2010). DOI: `10.1364/ol.35.002523` (pp. 33, 34).

[106] H. Clevenson et al. "High sensitivity gas sensor based on high-Q suspended polymer photonic crystal nanocavity," *Applied Physics Letters*. (2014). DOI: `10.1063/1.4879735` (p. 33).

[107] M. R. Foreman, J. D. Swaim, and F. Vollmer. "Whispering gallery mode sensors," *Advances in Optics and Photonics* **7** (2), 168 (June 2015). DOI: `10.1364/aop.7.000168` (p. 33).

[108] Y.-J. Rao et al. "Micro Fabry-Perot interferometers in silica fibers machined by femtosecond laser," *Optics Express*. (2007). DOI: `10.1364/oe.15.014123` (pp. 33, 34).

[109] A. Francois et al. "Whispering Gallery Mode Devices for Sensing and Biosensing," *Photonic Materials for Sensing, Biosensing and Display Devices*. Ed. by M. J. Serpe, Y. Kang, and Q. M. Zhang. Vol. 229. Springer Series in Materials Science. Cham: Springer International Publishing, 2016, 237–288. DOI: `10.1007/978-3-319-24990-2_9` (p. 33).

[110] T. Reynolds et al. "Optimization of whispering gallery resonator design for biosensing applications," *Optics Express*. (2015). DOI: `10.1364/oe.23.017067` (pp. 33, 59).

[111] Y. Zhang et al. "Functional Investigation of Effects on Transplantable Bone Marrow Stem Cells Label with Iron Oxide Nanoparticles," *Journal of Biomaterials and Tissue Engineering* **5** (6), 486–492 (June 2015). DOI: `10.1166/jbt.2015.1298` (p. 33).

[112] R. St-Gelais, J. Masson, and Y. A. Peter. “All-silicon integrated Fabry-Peacuterot cavity for volume refractive index measurement in microfluidic systems,” *Applied Physics Letters* **94** (24), (2009). DOI: `10.1063/1.3152286` (p. 33).

[113] T. Wei et al. “Temperature-insensitive miniaturized fiber inline Fabry-Perot interferometer for highly sensitive refractive index measurement,” *Optics Express* **16** (8), 5764–5769 (2008). DOI: `10.1364/oe.16.005764` (pp. 33, 34, 49).

[114] S. Pang, R. E. Beckham, and K. E. Meissner. “Quantum dot-embedded microspheres for remote refractive index sensing,” *Applied Physics Letters* **92** (22), (2008). DOI: `10.1063/1.2937209` (p. 34).

[115] P. Zijlstra, K. L. van der Molen, and A. P. Mosk. “Spatial refractive index sensor using whispering gallery modes in an optically trapped microsphere,” *Applied Physics Letters* **90** (16), (2007). DOI: `10.1063/1.2722695` (p. 34).

[116] I. M. White and X. Fan. “On the performance quantification of resonant refractive index sensors,” *Optics Express* **16** (2), 1020–1028 (2008). DOI: `10.1364/OE.16.001020` (pp. 34, 42, 60).

[117] D.-W. Duan et al. “Microbubble based fiber-optic Fabry-Perot interferometer formed by fusion splicing single-mode fibers for strain measurement,” *Applied Optics* **51** (8), 1033–1036 (2012). DOI: `10.1364/ao.51.001033` (p. 34).

[118] C. R. Liao, T. Y. Hu, and D. N. Wang. “Optical fiber Fabry-Perot interferometer cavity fabricated by femtosecond laser micromachining and fusion splicing for refractive index sensing,” *Optics Express* **20** (20), 22813–22818 (2012). DOI: `10.1364/oe.20.022813` (p. 34).

[119] Y. Guo et al. "Optofluidic Fabry-Perot cavity biosensor with integrated flow-through micro-/nanochannels," *Applied Physics Letters* **98** (4), (2011). DOI: `10.1063/1.3548673` (p. 34).

[120] W. Z. Song et al. "Refractive index measurement of single living cells using on-chip Fabry-Perot cavity," *Applied Physics Letters* **89** (20), (2006). DOI: `10.1063/1.2387965` (p. 34).

[121] S. Calixto et al. "Capillary refractometer integrated in a microfluidic configuration," *Applied Optics* **47** (6), 843–848 (2008). DOI: `10.1364/ao.47.000843` (p. 34).

[122] H. El Ghandoor et al. "Measuring the refractive index of crude oil using a capillary tube interferometer," *Optics and Laser Technology* **35** (5), 361–367 (2003). DOI: `10.1016/s0030-3992(03)00029-x` (p. 34).

[123] B. Krattiger et al. "Laser-based refractive-index detection for capillary electrophoresis: ray-tracing interference theory," *Applied Optics* **32** (6), 956 (1993). DOI: `10.1364/ao.32.000956` (p. 34).

[124] S. W. Qi et al. "Analysis of capillary interferometry for measuring refractive indices of minute samples," *Applied Optics* **43** (3), 530–536 (2004). DOI: `10.1364/ao.43.000530` (p. 34).

[125] H. J. Tarigan et al. "Capillary-scale refractive index detection by interferometric backscatter," *Analytical Chemistry* **68** (10), 1762–1770 (1996). DOI: `10.1021/ac9511455` (p. 34).

[126] A. Yang et al. "Measuring the refractive indices of liquids with a capillary tube interferometer," *Applied Optics* **45** (31), 7993–7998 (2006). DOI: `10.1364/ao.45.007993` (p. 34).

[127] S. Surdo et al. "Optofluidic microsystems with integrated vertical one-dimensional photonic crystals for chemical analysis," *Lab on a Chip* **12** (21), 4403–4415 (2012). DOI: `10.1039/c2lc40613f` (p. 34).

[128] S. Surdo et al. “Capillarity-driven (self-powered) one-dimensional photonic crystals for refractometry and (bio) sensing applications,” *Rsc Advances* **4** (94), 51935–51941 (2014). DOI: `10.1039/c4ra09056j` (p. 34).

[129] O. Svelto et al. “Lasers and Coherent Light Sources,” *Springer Handbook of Lasers and Optics*. Ed. by F. Träger. New York, NY: Springer New York, 2007, 583–936. DOI: `10.1007/978-0-387-30420-5_11` (p. 36).

[130] URL: `http://www.polysciences.com/default/pentabromophenyl-acrylate`.

[131] E. Klantsataya et al. “Effect of surface roughness on metal enhanced fluorescence in planar substrates and optical fibers,” *Optical Materials Express* **6** (6), 2128–2138 (2016). DOI: `10.1364/ome.6.002128` (pp. 38, 44).

[132] Y. Clergent, C. Durou, and M. Laurens. “Refractive index variations for argon, nitrogen, and carbon dioxide at lambda = 632.8 nm (He-Ne laser light) in the range 288.15K <= T <= 323.15K, 0 < p < 110 kPa,” *Journal of Chemical and Engineering Data* **44** (2), 197–199 (1999). DOI: `10.1021/je980133o` (pp. 42, 161).

[133] F. Carpignano et al. “Refractive Index Sensing in Rectangular Glass Micro-Capillaries by Spectral Reflectivity Measurements,” *Ieee Journal of Selected Topics in Quantum Electronics* **22** (3), (2016). DOI: `10.1109/jstqe.2015.2455339` (p. 42).

[134] M. Piliarik and J. J. Homola. “Surface plasmon resonance (SPR) sensors: approaching their limits?,” *Optics Express* **17** (19), 16505–16517 (2009). DOI: `10.1364/oe.17.016505` (pp. 42, 60).

[135] G. Liu and M. Han. “Fiber-optic gas pressure sensing with a laser-heated silicon-based Fabry-Perot interferometer,” *Optics Letters* **40** (11), 2461–2464 (2015). DOI: `10.1364/ol.40.002461` (p. 43).

[136] B. Xu et al. "Fiber-tip gas pressure sensor based on dual capillaries," *Optics Express* **23** (18), 23484–23492 (2015). DOI: `10.1364/oe.23.023484` (pp. 43, 49).

[137] E. Pinet. "Pressure measurement with fiber-optic sensors: Commercial technologies and applications," *21st International Conference on Optical Fiber Sensors*. Ed. by W. J. Bock, J. Albert, and X. Bao. Vol. 7753. Proceedings of SPIE. 2011. DOI: `10.1117/12.895536` (p. 49).

[138] Y. Z. Zhu et al. "High-temperature fiber-tip pressure sensor," *Journal of Lightwave Technology* **24** (2), 861–869 (2006). DOI: `10.1109/jlt.2005.862444` (p. 49).

[139] URL: `https://www.crystran.co.uk/optical-materials/silica-glass-sio2`.

[140] W. B. Emerson. "Compressibility of fused-quartz glass at atmospheric pressure," *Journal of Research of the National Bureau of Standards* **18** (6), 683–711 (1937). DOI: `10.6028/jres.018.044` (p. 49).

[141] S. B. Sane and W. G. Knauss. "The time-dependent bulk response of Poly (Methyl Methacrylate)," *Mechanics of Time-Dependent Materials* **5** (4), 293–324 (2001). DOI: `10.1023/a:1012517421899` (p. 49).

[142] J. J. Xie et al. "First-principles calculation of the thermal properties of silver," *Physical Review B* **59** (2), 965–969 (1999). DOI: `10.1103/PhysRevB.59.965` (p. 49).

[143] J. Mai et al. "Rapid detection of trace bacteria in biofluids using porous monoliths in microchannels," *Biosensors & Bioelectronics* **54**. 435–441 (2014). DOI: `10.1016/j.bios.2013.11.012` (p. 50).

[144] S. H. Huang et al. "Whispering gallery mode resonator sensor for in situ measurements of hydrogel gelation," *Optics Express* **26** (1), 51–62 (2018). DOI: `10.1364/OE.26.000051` (p. 59).

[145] A. François et al. "Lasing of whispering gallery modes in optofluidic microcapillaries," *Optics Express* **24** (12), 12466–12477 (2016). DOI: 10.1364/OE.24.012466 (pp. 60, 68).

[146] V. Zamora, Z. Zhang, and A. Meldrum. "Refractometric Sensing of Heavy Oils in Fluorescent Core Microcapillaries," *Oil Gas Sci. Technol. – Rev. IFP Energies nouvelles* **70** (3), 487–495 (2015). DOI: 10.2516/ogst/2013113 (p. 60).

[147] H. Li and X. Fan. "Characterization of sensing capability of optofluidic ring resonator biosensors," *Applied Physics Letters* **97** (1), (2010). DOI: 10.1063/1.3462296 (p. 60).

[148] T. Ling and L. J. Guo. "Sensitivity enhancement in optical microtube resonator sensors via mode coupling," *Applied Physics Letters*. (2013). DOI: 10.1063/1.4813007 (p. 60).

[149] G. Rigamonti et al. "Flow-through micro-capillary refractive index sensor based on T/R spectral shift monitoring," *Biomedical Optics Express* **8** (10), 4438–4453 (2017). DOI: 10.1364/BOE.8.004438 (p. 60).

[150] F. Sun et al. "High quality factor and high sensitivity photonic crystal rectangular holes slot nanobeam cavity with parabolic modulated lattice constant for refractive index sensing," *Optics Communications* **399**. 56–61 (Sept. 2017) (p. 60).

[151] I. H. Malitson. "Interspecimen Comparison of the Refractive Index of Fused Silica*,†," *Journal of the Optical Society of America* **55** (10), 1205–1209 (1965). DOI: 10.1364/JOSA.55.001205 (pp. 65, 77).

[152] J. R. Rumble. "CRC Handbook of Chemistry and Physics," 98th ed. Boca Raton, FL: CRC Press/Taylor & Francis (p. 65).

[153] Y.-C. Chen, Q. Chen, and X. Fan. "Lasing in blood," *Optica* **3** (8), 809 (2016). DOI: 10.1364/optica.3.000809 (pp. 69, 76).

[154] G. Mi et al. “Silicon microring refractometric sensor for atmospheric CO2 gas monitoring,” *Optics Express* **24** (2), 1773–1780 (2016). DOI: `10.1364/oe.24.001773` (p. 75).

[155] A. L. Washburn et al. “Label-free, multiplexed biomolecular analysis using arrays of silicon photonic microring resonators,” *Eurosensors Xxv*. Ed. by G. Kaltsas and C. Tsamis. Vol. 25. Procedia Engineering. 2011. DOI: `10.1016/j.proeng.2011.12.016` (p. 75).

[156] D. X. Xu et al. “Folded cavity SOI microring sensors for high sensitivity and real time measurement of biomolecular binding,” *Optics Express* **16** (19), 15137–15148 (2008). DOI: `10.1364/oe.16.015137` (p. 75).

[157] H. Zhu et al. “Analysis of biomolecule detection with optofluidic ring resonator sensors,” *Optics Express* **15** (15), 9139–9146 (2007). DOI: `10.1364/oe.15.009139` (p. 75).

[158] A. Weller et al. “Whispering gallery mode biosensors in the low-Q limit,” *Applied Physics B-Lasers and Optics* **90** (3-4), 561–567 (2008). DOI: `10.1007/s00340-007-2893-2` (p. 75).

[159] T. Reynolds et al. “Dynamic Self-Referencing Approach to Whispering Gallery Mode Biosensing and Its Application to Measurement within Undiluted Serum,” *Analytical Chemistry* **88** (7), 4036–4040 (2016). DOI: `10.1021/acs.analchem.6b00365` (p. 75).

[160] Y. Wang et al. “Tapered optical fiber waveguide coupling to whispering gallery modes of liquid crystal microdroplet for thermal sensing application,” *Optics Express* **25** (2), 918–926 (2017). DOI: `10.1364/oe.25.000918` (p. 75).

[161] T. Le et al. “Polymer optical waveguide vertically coupled to high-Q whispering gallery resonators,” *Ieee Photonics Technology Letters* **18** (5-8), 859–861 (2006). DOI: `10.1109/lpt.2006.871815` (p. 75).

[162] A. Rasoloniaina et al. “Controling the coupling properties of active ultrahigh-Q WGM microcavities from undercoupling to selective amplification,” *Scientific Reports* **4**. (2014). DOI: 10.1038/srep04023 (p. 75).

[163] L. Shao et al. “Detection of Single Nanoparticles and Lentiviruses Using Microcavity Resonance Broadening,” *Advanced Materials* **25** (39), 5616–5620 (Oct. 2013). DOI: 10.1002/adma201302572 (p. 75).

[164] L. He et al. “Ultrasensitive detection of mode splitting in active optical microcavities,” *Physical Review A* **82** (5), (2010). DOI: 10.1103/PhysRevA.82.053810 (p. 75).

[165] X. Xu et al. “Phone-sized whispering-gallery microresonator sensing system,” *Optics Express* **24** (23), 25905–25910 (2016). DOI: 10.1364/oe.24.025905 (pp. 76, 90).

[166] G. Decher. “Fuzzy nanoassemblies: Toward layered polymeric multicomposites,” *Science* **277** (5330), 1232–1237 (1997). DOI: 10.1126/science.277.5330.1232 (p. 76).

[167] K. J. Rowland et al. “Fluorescent polymer coated capillaries as optofluidic refractometric sensors,” *Optics Express* **21** (9), 11492–11505 (2013). DOI: 10.1364/oe.21.011492 (p. 76).

[168] A. Meldrum, P. Bianucci, and F. Marsiglio. “Modification of ensemble emission rates and luminescence spectra for inhomogeneously broadened distributions of quantum dots coupled to optical microcavities,” *Optics Express* **18** (10), 10230–10246 (2010). DOI: 10.1364/oe.18.010230 (p. 76).

[169] Y. Zhi, J. Valenta, and A. Meldrum. “Structure of whispering gallery mode spectrum of microspheres coated with fluorescent silicon quantum dots,” *Journal of the Optical Society of America*

B-Optical Physics **30** (11), 3079–3085 (2013). DOI: 10.1364/josab.30.003079 (p. 76).

[170] S. F. Wondimu et al. “Robust label-free biosensing using microdisk laser arrays with on-chip references,” *Optics Express* **26** (3), 3161–3173 (2018). DOI: 10.1364/oe.26.003161 (p. 76).

[171] A. Francois and M. Himmelhaus. “Whispering gallery mode biosensor operated in the stimulated emission regime,” *Applied Physics Letters* **94** (3), (2009). DOI: 10.1063/1.3059573 (p. 76).

[172] V. Zamora et al. “Cylindrical optical microcavities: Basic properties and sensor applications,” *Photonics and Nanostructures-Fundamentals and Applications* **9** (2), 149–158 (2011). DOI: 10.1016/j.photonics.2010.09.007 (p. 77).

[173] S. A. Greenberg. “The depolymerization of silica in sodium hydroxide solutions,” *Journal of Physical Chemistry* **61** (7), 960–965 (1957). DOI: 10.1021/j150553a027 (p. 78).

[174] S. H. Behrens and D. G. Grier. “The charge of glass and silica surfaces,” *Journal of Chemical Physics* **115** (14), 6716–6721 (2001). DOI: 10.1063/1.1404988 (p. 78).

[175] G. Decher and J. Schmitt. “Fine-Tuning of the film thickness of ultrathin multilayer films composed of consecutively alternating layers of anionic and cationic polyelectrolytes,” *Trends in Colloid and Interface Science VI*. Ed. by C. Helm, M. Lösche, and H. Möhwald. Darmstadt: Steinkopff, 1992, 160–164 (p. 79).

[176] “Helium Ion Microscopy,” *Helium Ion Microscopy*. Ed. by G. Hlawacek and A. Golzhauser. Nanoscience and Technology. 2016, 1–526. DOI: 10.1007/978-3-319-41990-9 (p. 79).

[177] G. Ladam et al. “Protein interactions with polyelectrolyte multilayers: Interactions between human serum albumin and polystyrene sulfonate/polyallylamine multilayers,” *Biomacromolecules* **1** (4), 674–687 (2000). DOI: `10.1021/bm005572q` (p. 86).

[178] C. L. Schauer et al. “Color changes in chitosan and poly(allyl amine) films upon metal binding,” *Thin Solid Films* **434** (1-2), 250–257 (2003). DOI: `10.1016/s0040-6090(03)00055-5` (p. 86).

[179] Z. Feldötö, I. Varga, and E. Blomberg. “Influence of salt and rinsing protocol on the structure of PAH/PSS polyelectrolyte multilayers,” *Langmuir* **26** (22), 17048–17057 (2010). DOI: `10.1021/la102351f` (p. 86).

[180] A. François, H. Schwefel, and T. M. Monro. “Using the lasing threshold in whispering gallery mode resonators for refractive index sensing,” *Laser Resonators, Microresonators, and Beam Control XX*. Ed. by A. V. Kudryashov, A. H. Paxton, and V. S. Ilchenko. Vol. 10518. International Society for Optics and Photonics. SPIE, 2018, 89–93. DOI: `10.1117/12.2288871` (p. 90).

[181] R. W. Howarth, R. Santoro, and A. Ingraffea. “Methane and the greenhouse-gas footprint of natural gas from shale formations,” *Climatic Change* **106** (4), 679–690 (2011). DOI: `10.1007/s10584-011-0061-5` (p. 100).

[182] E. D. Schulze et al. “Importance of methane and nitrous oxide for Europe’s terrestrial greenhouse-gas balance,” *Nature Geoscience* **2** (12), 842–850 (2009). DOI: `10.1038/ngeo686` (p. 100).

[183] F. Joos et al. “Carbon dioxide and climate impulse response functions for the computation of greenhouse gas metrics: A multi-model analysis,” *Atmospheric Chemistry and Physics* **13** (5), 2793–2825 (2013). DOI: `10.5194/acp-13-2793-2013` (p. 100).

[184] R. Kan et al. "A high sensitivity spectrometer with tunable diode laser for ambient methane monitoring," *Chin. Opt. Lett.* **5** (1), 54–57 (Jan. 2007) (pp. 100, 101).

[185] A. Hartmann et al. "Ultra-compact TDLAS humidity measurement cell with advanced signal processing," *Applied Physics B: Lasers and Optics* **115** (2), 263–268 (2014). DOI: 10.1007/s00340-013-5599-7 (pp. 100, 101).

[186] C. Li et al. "Compact TDLAS based optical sensor for ppb-level ethane detection by use of a 3.34 μm room-temperature CW interband cascade laser," *Sensors and Actuators, B: Chemical* **232**. 188–194 (2016). DOI: 10.1016/j.snb.2016.03.141 (pp. 100, 101).

[187] L. Dong et al. "Compact TDLAS based sensor design using interband cascade lasers for mid-IR trace gas sensing," *Optics Express* **24** (6), A528 (2016). DOI: 10.1364/oe.24.00a528 (pp. 100, 101).

[188] K. Sun et al. "Analysis of calibration-free wavelength-scanned wavelength modulation spectroscopy for practical gas sensing using tunable diode lasers," *Measurement Science and Technology* **24** (12), 125203 (Dec. 2013). DOI: 10.1088/0957-0233/24/12/125203 (p. 101).

[189] G. B. Rieker, J. B. Jeffries, and R. K. Hanson. "Calibration-free wavelength-modulation spectroscopy for measurements of gas temperature and concentration in harsh environments," *Applied Optics* **48** (29), 5546 (Oct. 2009). DOI: 10.1364/AO.48.005546 (p. 101).

[190] Z. Du et al. "Mid-infrared tunable laser-based broadband fingerprint absorption spectroscopy for trace gas sensing: A review," *Applied Sciences (Switzerland)* **9** (2), 1–33 (2019). DOI: 10.3390/app9020338 (p. 101).

[191] H. Li et al. "Extension of wavelength-modulation spectroscopy to large modulation depth for diode laser absorption measurements in high-pressure gases," *Applied Optics* **45** (5), 1052–1061 (2006). DOI: 10.1364/AO.45.001052 (p. 101).

[192] C. S. Goldenstein et al. "Fitting of calibration-free scanned-wavelength-modulation spectroscopy spectra for determination of gas properties and absorption lineshapes," *Applied Optics* **53** (3), 356 (2014). DOI: 10.1364/ao.53.000356 (p. 101).

[193] E. Hawe et al. "CO2 monitoring and detection using an integrating sphere as a multipass absorption cell," *Measurement Science and Technology* **18** (10), 3187–3194 (2007). DOI: 10.1088/0957-0233/18/10/S21 (p. 103).

[194] H. B. Singh. "Composition, chemistry, and climate of the atmosphere," Van Nostrand Reinhold New York, 1995 (p. 103).

[195] R. V. Kochanov et al. "HITRAN Application Programming Interface (HAPI): A comprehensive approach to working with spectroscopic data," *Journal of Quantitative Spectroscopy and Radiative Transfer* **177**. 15–30 (2016). DOI: https://doi.org/10.1016/j.jqsrt.2016.03.005 (p. 103).

[196] H. Schlager, V. Grewe, and A. Roiger. "Chemical Composition of the Atmosphere." *Atmospheric Physics: Background – Methods – Trends*. Ed. by U. Schumann. Berlin, Heidelberg: Springer Berlin Heidelberg, 2012, 17–35. DOI: 10.1007/978-3-642-30183-4_2 (p. 103).

[197] URL: https://www.thorlabs.com/images/TabImages/Rise%7B%5C_%7DTime%7B%5C_%7D3dB%7B%5C_%7DBandwidth%7B%5C_%7DRelationship%7B%5C_%7DLab%7B%5C_%7DFact.pdf (visited on 12/17/2020).

[198] S. Bergin. “Pathlength calibration of integrating sphere based gas cells.” PhD thesis. 2016 (p. 105).

[199] P. Horowitz and W. Hill. “The Art of Electronics,” 3rd. New York, NY: Cambridge University Press, 2015, 538 (p. 118).

[200] URL: `https://www.labsphere.com/site/assets/files/2553/a-guide-to-reflectance-materials-and-coatings.pdf`.

[201] URL: `https://www.newport.com/medias/sys%7B%5C_%7Dmaster/images/images/hc3/h13/8797116858398/Integrating-Spheres-Datasheet.pdf`.

[202] G. Hartfield, J. Blunden, and D. S. Arndt. “State of the climate in 2017,” *Bulletin of the American Meteorological Society* **99** (8), Si–S310 (2018). DOI: `10.1175/2018BAMSStateoftheClimate.1` (pp. 121, 123).

[203] L. M. Hanssen. “New instrumentation development at the National Institute of Standards and Technology for spectral diffuse reflectance and transmittance measurement,” *Spectrophotometry, Luminescence and Colour; Science & Compliance*. Ed. by C. Burgess and D. G. Jones. Vol. 6. Analytical Spectroscopy Library. Elsevier, 1995, 115–128. DOI: `https://doi.org/10.1016/S0926-4345(06)80010-6` (p. 125).

[204] C. L. Souza, C. A. Chernicharo, and S. F. Aquino. “Quantification of dissolved methane in UASB reactors treating domestic wastewater under different operating conditions,” *Water Science and Technology* **64** (11), 2259–2264 (2011). DOI: `10.2166/wst.2011.695` (p. 125).

[205] P. Servio and P. Englezos. “Measurement of dissolved methane in water in equilibrium with its hydrate,” *Journal of Chemical and Engineering Data* **47** (1), 87–90 (2002). DOI: `10.1021/je0102255` (p. 125).

[206] S. I. Pogosyan et al. "Absorption spectroscopy of microalgae, cyanobacteria, and dissolved organic matter: Measurements in an integrating sphere cavity," *Oceanology* **49** (6), 866–871 (2009). DOI: `10.1134/S0001437009060125` (p. 129).

[207] E. R. Peck and B. N. Khanna. "Dispersion of Nitrogen," *Journal of the Optical Society of America* **56** (8), 1059 (Aug. 1966). DOI: `10.1364/josa.56.001059` (p. 162).

[208] E. R. Peck and D. J. Fisher. "Dispersion of Argon," *Journal of the Optical Society of America* **54** (11), 1362 (Nov. 1964). DOI: `10.1364/josa.54.001362` (p. 162).

Appendix A

Code for Monte Carlo integrating sphere simulation

A.1 Simulation Code

This is the code that was discussed in Sec. 6.2 which was used to provide a distribution of path lengths for rays travelling through the integrating sphere. The resulting array `cases` contained the path lengths for rays which struck the detector, and this array was then used to examine the distribution and the mean path length.

```
(* Helper function to determine when a
ray intersects with the sphere. *)
intersectionCompile = Compile[
  {{o, _Real, 1}, {u, _Real, 1}, {r, _Real}, {c, _Real, 1}},
  o + ((-2*u . (o - c) +
  Sqrt[(2*u . (o - c))^2 - 4*u . u*((o - c) . (o - c) - r^2)])/
  (2*u . u))*u,
  CompilationTarget -> "C"
]
```

```

(* Helper function for multiplying quaternions. *)
qm = Compile[
  {{a, _Real, 1}, {b, _Real, 1}},
  Module[
    {vec = {0., 0., 0.}},
    vec = a[[1]]*b[[2 ;; 4]] + b[[1]]*a[[2 ;; 4]] +
      {a[[3]]*b[[4]] - a[[4]]*b[[3]],
      a[[4]]*b[[2]] - a[[2]]*b[[4]],
      a[[2]]*b[[3]] - a[[3]]*b[[2]]};
    {a[[1]]*b[[1]] - (a[[2]]*b[[2]] +
      a[[3]]*b[[3]] + a[[4]]*b[[4]]),
    vec[[1]],
    vec[[2]],
    vec[[3]]}
  ],
  CompilationTarget -> "C"
]

(* The main function which fires rays
and returns their lengths. *)
traceCompile = Compile[
  {{start, _Real, 1}, {direction, _Real, 1}},
  Module[
    {orig = start, lastOrig = start, dir = direction,
    len = 0., x, y, z, p, pquat, theta, phi, rand, axis,
    axisnorm, q1, q1inv, q2, q2inv},
    While[
      True,
      {x, y, z} = orig =
        intersectionCompile[orig, dir, 0.0381, {0, 0, 0}];
      (* Test for various cases. If the ray is absorbed,
      the length is set to zero. *)
      Which[
        (* Ray entered the photodetector. *)
        ArcCos[orig .
          {-0.026941, 0., 0.026941}/
```

```
          (Sqrt[orig . orig]*0.0381)] < 0.171442 &&
        ArcCos[orig . dir/(Sqrt[orig . orig]*Sqrt[dir . dir])]
            < 0.610865,
        len += Sqrt[Total[(orig - lastOrig)^2]]; Break[],
        (* Ray entered a gas port. *)
        y^2 + z^2 < 0.0016^2,
        len = 0.; Break[],
        (* Ray struck the laser. *)
        x^2 + y^2 < 0.0025^2 && z > 0,
        len = 0.; Break[],
        (* Ray struck the fibre port. *)
        ArcCos[orig .
          {0.026941, 0., 0.026941}/
          (Sqrt[orig . orig]*0.0381)] < 0.013124,
        len = 0.; Break[],
        (* Ray struck the detector at the wrong angle. *)
        ArcCos[orig .
          {-0.026941, 0., 0.026941}/
          (Sqrt[orig . orig]*0.0381)] < 0.171442,
        len = 0.; Break[],
        (* Ray struck the ring where the two hemispheres meet. *)
        -0.00025 < z < 0.00025,
        len = 0.; Break[],
        (* Ray was absorbed by the gold coating. *)
        RandomReal[] > 0.995,
        len = 0.; Break[]
      ];
      (* Add the length of the pass across the sphere to the
      ray's total length, and choose a new direction to propagate
      if none of the above conditions were met. *)
      len += Sqrt[Total[(orig - lastOrig)^2]];
      p = -orig/Sqrt[orig . orig];
      pquat = {0., p[[1]], p[[2]], p[[3]]};
      theta = RandomReal[{-0.99*(Pi/2), 0.99*(Pi/2)}];
      phi = RandomReal[{-Pi, Pi}];
      rand = RandomReal[{0, 1}, 3];
      axis = {rand[[2]]*p[[3]] - rand[[3]]*p[[2]],
```

```
        rand[[3]]*p[[1]] - rand[[1]]*p[[3]],
        rand[[1]]*p[[2]] - rand[[2]]*p[[1]]};
      axisnorm = axis/Sqrt[axis . axis];
      q1 = {Cos[theta/2],
        Sin[theta/2]*axisnorm[[1]], Sin[theta/2]*axisnorm[[2]],
        Sin[theta/2]*axisnorm[[3]]};
      q1inv = q1*{1, -1, -1, -1};
      q2 = {Cos[phi/2], Sin[phi/2]*p[[1]],
        Sin[phi/2]*p[[2]], Sin[phi/2]*p[[3]]};
      q2inv = q2*{1, -1, -1, -1};
      dir = qm[qm[q2, qm[qm[q1, pquat], q1inv]], q2inv][[2 ;; 4]];
      lastOrig = orig;
    ];
    (* Return the length the ray travelled if
    it hit the detector; return zero otherwise. *)
    len
  ],
  CompilationOptions -> {"InlineExternalDefinitions" -> True},
  CompilationTarget -> "C",
  RuntimeOptions -> "Speed"
]

(* Call the main function to find the lengths of some rays. *)
lens = Table[traceCompile[{0, 0, 0.0381}, {0, 0, -1}], 1000000];

(* Take only lengths greater than 0 m. *)
cases = Cases[lens, _?Positive];
```

Appendix B

Applicability of the Gladstone-Dale equation

B.1 Gladstone-Dale Equation

The Gladstone-Dale equation is given by $n = 1 + \mu(P/T)$ where n is the refractive index, μ is a gas-dependent constant, P is the pressure, and T is the temperature. In Ch. 3 I use this equation to determine the refractive index of argon and nitrogen at 170 kPA and 294.15 K (Fig. 3.4) and the refractive index of argon when its pressure is varied (Figs. 3.5 and 3.7 **a**) with a temperature of 294.15 K. The so-called gas-dependent constant, μ, is also dependent on the wavelength. I was unable to find a comprehensive calculation of the values for different wavelengths and thus used the values for argon and nitrogen of 762×10^{-9} and 808.8×10^{-9} K/Pa, respectively, found in Ref. [132] which are valid for 632.8 nm. However, since the refractive indices of argon and nitrogen vary in nearly the same way over the visible and NIR wavelengths, the Gladstone-Dale equation should be valid over this wavelength range which includes the relatively narrow wavelength range explored in Ch. 3 (~570 to 630 nm). I use only differences in refractive index to characterize the Fabry-Perot refractometric sensor; since the refractive indices, and therefore μ, display the same dispersion relationship, the difference in refractive indices between the different gases or the same gas at different pressures should be valid.

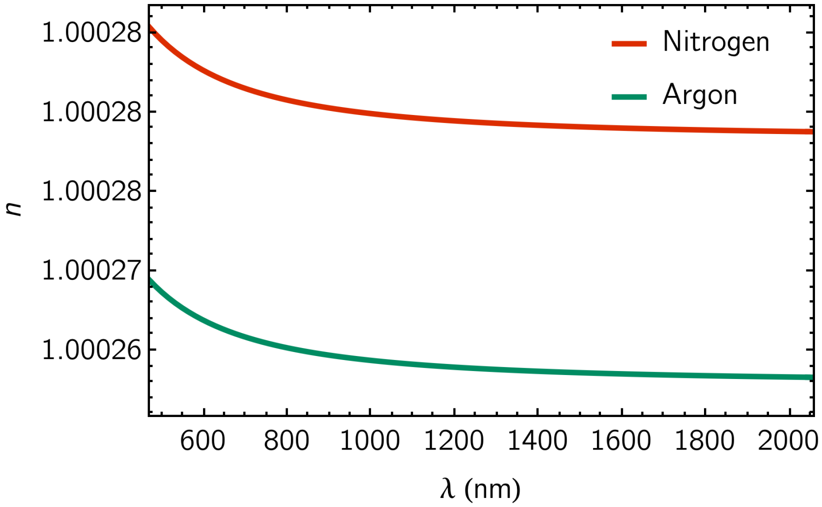

Figure B.1 Plot of the refractive indices of nitrogen and argon at 2988.15 K showing that both gases display the same dispersion relationship over visible and NIR wavelengths. The data for nitrogen comes from Ref. [207] and the argon data comes from Ref. [208]. Both sets of data were retrieved from `RefractiveIndex.info`.